ORGANIC GEOCHEMISTRY IN OCEANIC HYDROTHERMAL SYSTEMS: IMPLICATIONS FOR PREBIOTIC SYNTHESIS, EXTRATERRESTRIAL HABITABILITY, AND GREEN CHEMISTRY

by

ALEXANDRIA ROSE ASPIN

A dissertation submitted in partial fulfillment of the
requirements for the degree of

DOCTOR OF PHILOSOPHY IN BIOMEDICAL SCIENCES: HEALTH AND ENVIRONMENTAL CHEMISTRY

2025

Oakland University
Rochester, Michigan

Doctoral Advisory Committee:

Ziming Yang, Ph.D., Chair
Ngong Beyeh, Ph.D.
Ferman A. Chavez, Ph.D.

To my sweet Cedar, my dearest companion and greatest source of joy. You were my constant comfort and motivation through the hardest of times, and this work is dedicated to the love and happiness you brought into my life.

ACKNOWLEDGMENTS

I would like to express my deepest gratitude to my dissertation chair, Dr. Ziming Yang, for your invaluable guidance, patience, and support throughout this journey. The opportunities I have had under your mentorship were endless, and I am forever grateful for the role you played in shaping me as a researcher. I also extend my appreciation to my committee members, Dr. Ngong Beyeh and Prof. Ferman A. Chavez, for your insightful feedback and perspectives that helped strengthen this work. To my lab group members, past and present- thank you for your assistance and camaraderie. Your support and collaboration have made this experience not only enriching but also enjoyable.

To my friends and family, your unwavering belief in me has been a constant source of strength. Thank you for your patience, understanding, and encouragement, especially during the most demanding moments of this process. A special thank you to my mom, my greatest supporter from the beginning- your love, encouragement, and belief in me have been invaluable. To my best friends, Brittney Rajewski and Megan Jamison- thank you for keeping me sane, making me laugh, and reminding me that life exists outside of research. Finally, to my cats, Salem, Sage, Sargent, and Cedar- your steadfast companionship, perfectly timed interruptions, and endless comfort have brought me so much joy. You have been the best little research assistants I could have asked for.

Alexandria Rose Aspin

ABSTRACT

ORGANIC GEOCHEMISTRY IN OCEANIC HYDROTHERMAL SYSTEMS: IMPLICATIONS FOR PREBIOTIC SYNTHESIS, EXTRATERRESTRIAL HABITABILITY, AND GREEN CHEMISTRY

by

Alexandria Rose Aspin

Adviser: Ziming Yang, Ph.D.

Hydrothermal systems are unique environments that are relevant to many different applications. In particular, this dissertation details their relevance to the origin of life on Earth, the search for extraterrestrial habitable environments, and their use in sustainable practices. Chapters Two and Three seek to investigate the influences of parameters such as temperature, pH, and metal salts on the reaction pathways of important organics, including alkenes and amino acids, respectively. Acidic solutions promote the hydration and dimerization pathways of alkenes, while the presence of metal salts can enhance the dimerization and oxidation pathways. Similarly, these geochemical parameters influence amino acid reaction pathways and product distributions, where lower temperatures, basic pHs, and inorganic metals inhibit their degradation.

Chapter Three indicates the enhanced survivability of amino acids in environments that are expected on icy ocean moons, suggesting they may be prime targets for the search for life outside of Earth. Chapter 4 investigates whether the transition from liquid in the subsurface ocean to vacuum above the surface influences the relative abundances of biosignatures, as future missions will rely on the analysis of

materials above the icy surfaces to determine whether they could be inhabited. Simulation of the liquid-vacuum transition indicated the distributions were sufficiently conserved to allow distinction between biological and abiotic sources.

Finally, the green and sustainable recycling of plastic using Earth-abundant minerals has been investigated under hydrothermal conditions. The efficiency of plastic degradation was strongly influenced by its structure, where polymers with a C-C backbone degraded much slower under hydrothermal treatment compared to polymers containing a heteroatomic backbone. Furthermore, the presence of minerals selectively enhanced the degradation of heteroatomic plastics, highlighting the application of hydrothermal conversion as a green and sustainable alternative for pollutant recycling.

TABLE OF CONTENTS

TABLE OF CONTENTS—Continued

TABLE OF CONTENTS—Continued

TABLE OF CONTENTS—Continued

LIST OF TABLES

LIST OF FIGURES

LIST OF ABBREVIATIONS

γAB	γ-Aminobutyric Acid
AA	Amino Acid
AIB	Aminoisobutyric Acid
Ala	Alanine
Asp	Aspartic Acid
BPA	Bisphenol A
C_p	Heat Capacity
DCM	Dichloromethane
DFT	Density Functional Theory
DI	Deionized
FMQ	Fayalite-Magnetite-Quartz Mineral Assemblage
GC	Gas Chromatography
GC-FID	Gas Chromatography – Flame-Ionization Detector
GC-MS	Gas Chromatography-Mass Spectrometry
Glu	Glutamic Acid
Gly	Glycine
GSFC	Goddard Space Flight Center
His	Histidine
HKF	Helgeson-Kirkham Flowers
HPLC	High-Performance Liquid Chromatography
IFF	Iron-Ferrosilite-Fayalite Mineral Assemblage

IW	Iron-Wüstite Mineral Assemblage
K_{eq}	Equilibrium Constant
K_w	Ion Product of Water
Leu	Leucine
L_{freeze}	Enthalpy of Freezing
L_{vap}	Enthalpy of Vaporization
MH	Magnetite-Hematite Mineral Assemblage
NAC	N-acetylcysteine
OPA	o-Phthaldialdehyde
PBS	Phosphate Buffer Solution
PC	Polycarbonate
Phe	Phenylalanine
PPM	Pyrrhotite-Pyrite-Magnetite Mineral Assemblage
PS	Polystyrene
P_{sat}	Saturation Vapor Pressure
P_t	Triple Point Pressure
S_N1	Unimolecular Nucleophilic Substitution
S_N2	Bimolecular Nucleophilic Substitution
$t_{1/2}$	Half-Life
T_{freeze}	Time to Freeze
Thr	Threonine

Trp	Tryptophan
T_{triple}	Triple Point Temperature
T_{vent}	Surface Vent Temperature
Tyr	Tyrosine
UV-Vis	Ultraviolet-Visible
V_{fluid}	Vent Fluid Velocity
WORM	Water-Organic-Rock-Microbe

CHAPTER ONE

INTRODUCTION

1.1 Overview

Deep in the ocean at the seafloor, there are unique aqueous environments characterized by elevated temperatures and pressures. These systems are called hydrothermal vents and serve as a connection between the Earth's interior and ocean, from which Earth-abundant materials are exhumed from below the oceanic crust and to the seafloor. The fluids ejected from the oceanic crust are hot and rich in minerals and chemicals, which harbor rich ecosystems (Corliss et al., 1979; Spiess et al., 1980). Hydrothermal systems are also one of the environments that are reminiscent of early Earth (Martin et al., 2008; Russell & Hall, 1997), and it is recognized that vent systems are chemically reactive from disequilibria and provide suitable conditions for prebiotic synthesis (Baross & Hoffman, 1985). There have been extensive reports on reaction pathways and organic species observed in natural hydrothermal systems, however, their transformations have not fully been elucidated, and more importantly, how inorganic materials affect their pathways remains unknown. Hydrothermal environments are also expected to exist outside of Earth, such as in Saturn's moon Enceladus and Jupiter's moon Europa (Hsu et al., 2015; Lowell & DuBose, 2005; Waite et al., 2017), which has significance to the origin of and search for life beyond Earth. Because hydrothermal water possesses unique properties that can promote organic reactions, it has become useful in green and sustainable chemistry practices, where water is used as a benign

reaction medium and other Earth-abundant but non-toxic materials (i.e. minerals) as catalysts. This is a relatively new field of research, termed “geomimicry,” and has applications in a wide variety of fields, including waste recycling, pollutant remediation, and even synthetic organic chemistry (Yang & Aspin, 2023).

1.2 Deep-Ocean Hydrothermal Vents

Since their discovery more than 50 years ago (Corliss et al., 1979; Lonsdale, 1977), many hydrothermal systems and vents have been uncovered, such as the East Pacific Rise, Mid-Atlantic Ridge, Juan de Fuca Ridge, and the Izu-Bonin-Mariana arc volcanoes. Hydrothermal vent systems are commonly formed along plate tectonic boundaries. At convergent boundaries, such as in the case of the Izu-Bonin-Mariana arc volcanoes, two plate tectonics collide, forcing one to subduct beneath the other. As the plate subducts, it is heated by the Earth’s mantle, releasing fluids and magma to the

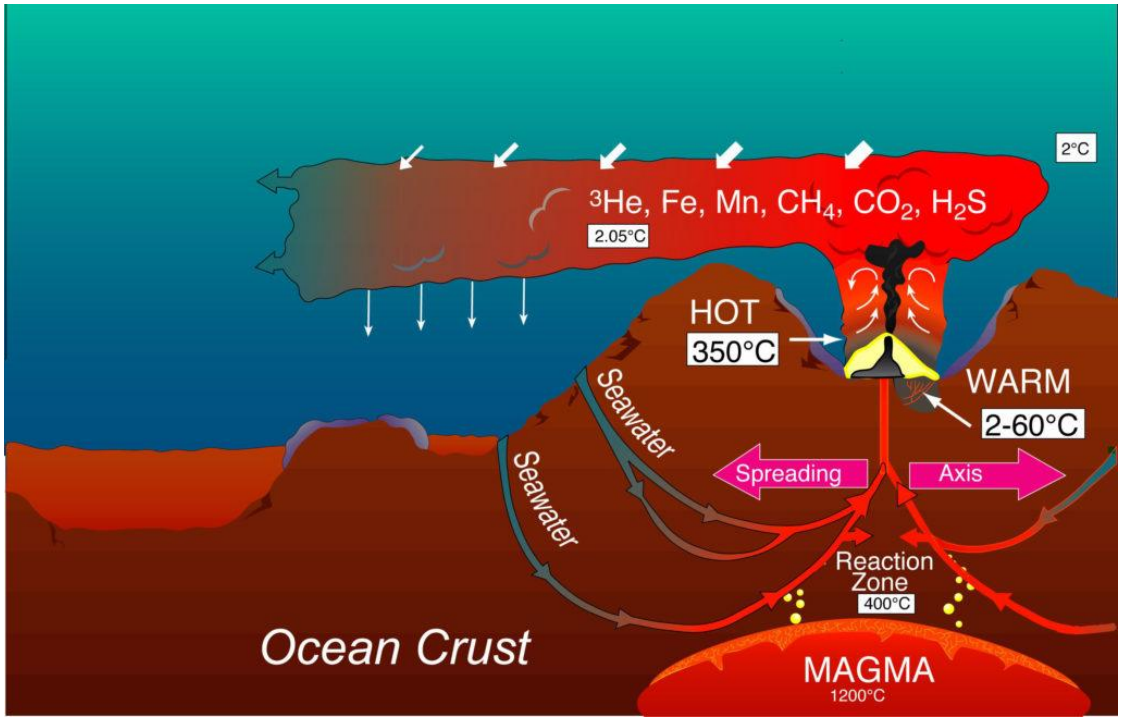

Figure 1. Schematic of a hydrothermal vent at a divergent plate boundary or spreading center (*Taken from the Schmidt Ocean Institute*)

oceanic crust, forming new seafloor. More commonly, however, are the vent systems at divergent plate boundaries, such as the East Pacific Rise, Mid-Atlantic Ridge, and the Juan de Fuca Ridge. Here, tectonic plates separate from one another, releasing molten rock from the Earth's crust, forming new oceanic floor (Figure 1).

As the plate tectonics at convergent and divergent boundaries move, the newly formed seafloor contains small cracks and fissures, which allows the relatively cold seawater to percolate through the crust. As the near-freezing seawater approaches the hot magma (1200^{o}C), chemical alteration of the fluids occurs, removing some chemicals such as magnesium and sulfate ions and incorporating them into the rocks. The fluids also dissolve chemical components from the rocks, including metals like copper, zinc, gold, and iron, as well as minerals such as metal sulfides. These superheated (<400 ^{o}C) and chemical-rich fluids are carried to the seafloor and ejected into the surrounding seawater (Figure 1). Because there is a strong temperature gradient between the ejected fluids and seawater, some of the dissolved metals and minerals rapidly precipitate out, falling to the seafloor and forming tall chimney-like structures. These chimneys can be classified by their characteristics (Lough et al., 2019). For example, "white smokers" are chimneys that are white from the deposits of barium, calcium, and silicon minerals, and are associated with lower temperatures (40-90^{o}C) and a more alkaline pH (9-11). "Black smokers" are the most widely discovered vent systems and are formed from deposits of iron and manganese sulfide minerals, which are darker in color and characterized by higher temperatures (up to 400^{o}C) and acidic pH (2-5).

Water at elevated temperatures and pressures has many unique properties compared to those at ambient conditions. For example, the density of water decreases quickly with increasing temperature (thermal expansion of water yields fewer molecules per unit area), nearly decreasing by 24% from 1000 kg/m^3 at 25^{o}C to roughly 765 kg/m^3 at 300^{o}C (Figure 2). This decrease in density affects the hydrogen bonding network within water, which is the source of many of water's unique properties (Akiya & Savage, 2002). In general, hydrogen bonding becomes weaker with increasing temperature and decreasing density. Unlike the infinite network of hydrogen bonding at ambient conditions, hydrothermal water has clusters of hydrogen-bonded water molecules, and with increasing temperatures and decreasing density, the average cluster size decreases (Akiya & Savage, 2002).

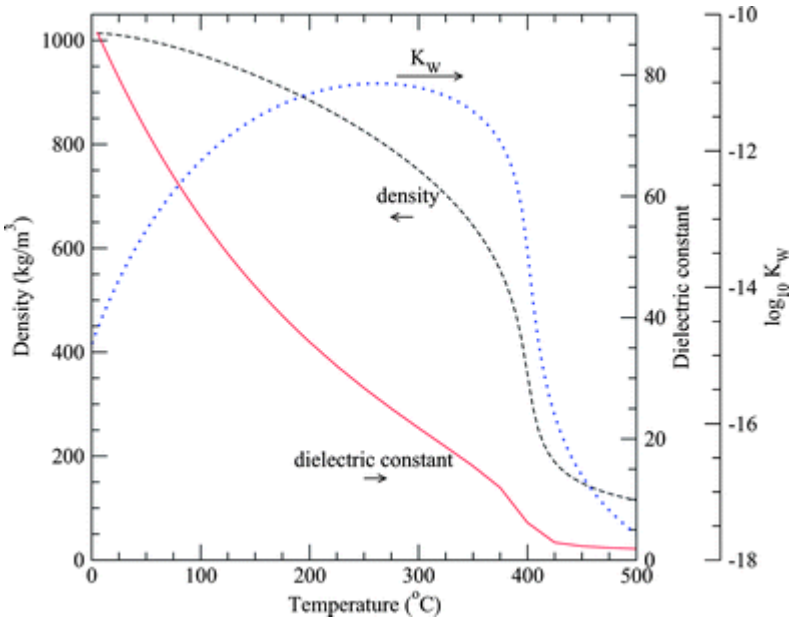

Figure 2. Water density, static dielectric constant, and ion dissociation constant of water at 30MPa as a function of temperature (Adapted from Peterson, et al., 2008)

The changes in the extent of hydrogen bonding and density are accompanied by a corresponding change in the static dielectric constant of water (Akerlof & Oshry, 1950; Heger et al., 1980; Mizan et al., 1994; Okada et al., 1997). With increasing temperature, the dielectric constant of water also decreases. For example, at 25^{o}C and 30MPa, the dielectric constant is roughly 90, while it decreases to 21 when the temperature increases to 300^{o}C (Figure 2). At this temperature, water behaves more like a polar organic solvent like ethanol, which has a dielectric constant of 24 at ambient conditions. This indicates that water can act as an organic solvent at elevated temperatures and pressures, dissolving small organic compounds that would otherwise not be soluble at room temperature. This also suggests that highly polar compounds like ionic salts will be less soluble in hydrothermal water compared to ambient liquid water (Tester et al., 1993).

Additionally, the ion product (or K_w) of water is another important property that is affected by the decrease in hydrogen bonding at high temperatures and pressures. As shown in Figure 2, increasing the temperature increases the ion product until the critical temperature (374^{o}C) is reached. The ion product is nearly three orders of magnitude higher right before the critical temperature than it is at ambient temperature. As a result, the H^+ and OH^- concentrations in hydrothermal water are naturally higher than in ambient liquid water. This is expected to enhance both acid- and base-catalyzed reactions within hydrothermal water (Chau et al., 2001; Holzapfel, 1969).

1.3 Hydrothermal Organic Geochemistry

Hydrothermal fluids venting from the oceanic crust are enriched in both organic compounds and inorganic materials. The Earth's interior and the subsurface biosphere are estimated to contain >99.5% of the carbon on the planet (Dasgupta & Hirschmann, 2010;

Hedges, 1992; Kelemen & Manning, 2015; Shock et al., 2019), yet relatively little is known about the deep carbon cycle. The study of deep carbon has emerged as a relatively new field, aiming to better understand the quantities, transport, and forms of carbon beneath Earth's surface.

The massive deep carbon reservoir is partly supplied by organic matter derived from living organisms (i.e. microbial communities, vegetation, etc), and is largely comprised of biomolecules such as lipids, lignin, and carbohydrates (Hedges, 1992). For example, biological activity in the deep biosphere is dominated by chemosynthetic organisms, which generate or utilize organic compounds near the vents to produce energy (McCollom & Shock, 1997). These microorganisms interact with the surrounding deep ocean environments, by providing a source of energy to organisms such as tubeworms, shrimp, mussels, crabs, and clams, which have all been observed in the deep biosphere. The organic carbon then sinks to the seafloor in the form of decaying biota, ultimately being sequestered and incorporated into rocks or turned into hydrocarbons.

The main known source of organic compounds on Earth is biologically derived, however, abiotic organic synthesis cannot be ignored, as it is essential to life emergence and sustenance. Recently, there has been the identification of small abiotically-formed compounds like methane and light hydrocarbons (short-chain alkanes or small organic acids) in a variety of geological environments on Earth including seafloor hydrothermal vents (Fryer et al., 1992; Ménez et al., 2018; Proskurowski et al., 2008). There are even further studies on the abiotic production of organic compounds and their transformations in hot hydrothermal fluids (Cho et al., 2025; Fu et al., 2020a; Liao et al., 2021; Loison et al., 2010; McCollom & Seewald, 2001; Robinson et al., 2021a; Robinson et al., 2019;

Shipp et al., 2013a; Shock et al., 2020; Shock, 1993). Studying their distribution and history is difficult, as their signatures are oftentimes too diluted to observe overtop the biological inputs, however, exploring the transformations of abiotic organic molecules is fundamental to astrobiology research and the origin of life.

Hydrothermal fluids are not only characterized by the presence of organic matter, but also by the wide distribution of inorganic materials such as mineral assemblages and dissolved metal ions. Commonly occurring mineral assemblages in natural hydrothermal environments include oxides (hematite Fe_2O_3, magnetite Fe_3O_4, corundum Al_2O_3) (Nadoll et al., 2014) and sulfides (pyrite FeS_2, pyrrhotite FeS, sphalerite ZnS, chalcopyrite $CuFeS_2$) (Large, 1977). Some of these minerals contain redox-active metals, which can control the redox state of hydrothermal fluids, as shown in Figure 3 (Shock et al., 2019). For example, in solutions buffered by the iron-wüstite (IW) and iron-ferrosilite-fayalite (IFF) assemblages, higher activities of aqueous hydrogen are expected, corresponding to more reducing conditions. This means that when carbon is present in solutions where these minerals are in equilibrium, the carbon will most likely be reduced such as in hydrocarbons (Shock et al., 2019). Conversely, when the pyrrhotite-pyrite-magnetite (PPM) and magnetite-hematite (MH) assemblages dominate the hydrothermal fluids, more oxidizing conditions and lower activities of hydrogen are expected. When MH is in equilibrium, organic carbon will almost exclusively be in a more oxidized form such as carboxylic acids or ketones (Shock et al., 2019). However, the PPM and FMQ (fayalite-magnetite-quartz) assemblages are crossed by the dashed line at elevated temperatures (Figure 3), which represents conditions where CO_2 and CH_4 are in equilibrium. This suggests that lower reaction temperatures and aqueous hydrogen

activities in the presence of FMQ or PPM favor a more reduced form of carbon, while higher reaction temperatures and hydrogen activities favor more oxidized carbon. Indeed, minerals have been shown experimentally to influence oxidation and reduction reaction pathways of organic carbon in elevated temperatures and pressures (Johnson-Finn et al., 2021; Venturi et al., 2017; Yang et al., 2018).

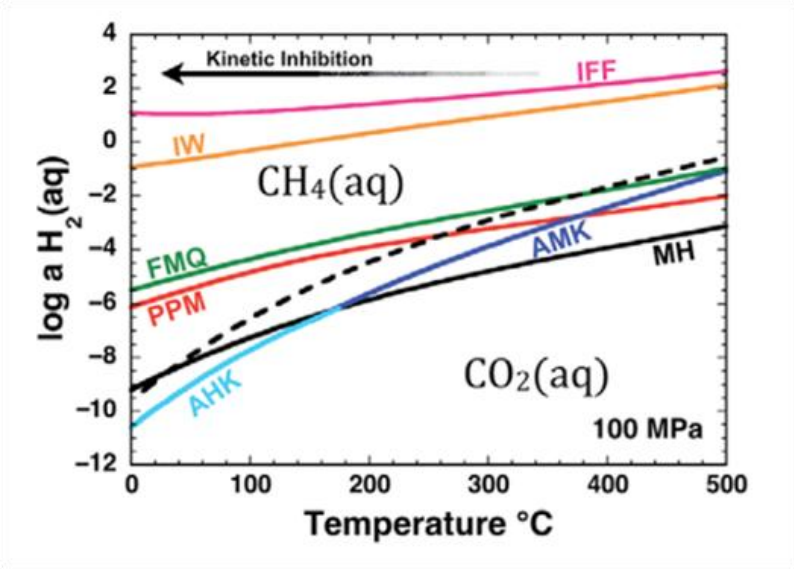

Figure 3. The activity of aqueous H_2 regulated by different mineral assemblages as a function of temperature at 100 MPa. The dashed curve indicates the activities of H_2 when methane and carbon dioxide are at equilibrium in only water (Taken from Shock et al., 2019)

The presence of metal ions in natural hydrothermal systems is also inevitable due to the dissolution of surrounding minerals. When superheated fluids rise from the Earth's crust to the seafloor, they are enriched in dissolved metals such as Fe, Cu, Zn, and Au (Brugger et al., 2016; Haase et al., 2009; Qiu et al., 2023; Sander & Koschinsky, 2011). Some of these metals are also redox-active and can potentially influence the oxidative and reductive pathways of organic molecules in hydrothermal systems (Bockisch et al., 2019; Fu et al., 2020a; Liao et al., 2021; Liao et al., 2022).

1.4 Biosignature Preservation and Detection

Hydrothermal systems are not only observed on the oceanic seafloor but are also expected to occur beyond Earth, such as in Saturn's icy moon, Enceladus. Data from the Cassini mission, which was sent to study Saturn and its moons and ring system in 1997, suggests Enceladus contains a global subsurface liquid ocean beneath the ice shell (Patthoff & Kattenhorn, 2011) that is in direct contact with the rocky interior, as shown in Figure 4 (Hsu et al., 2015). Additionally, jet-like features jutting from the icy surface were observed, generating a large cloud of water vapor and ice particles above the southern pole. The detection of nanometer-sized silica particles and high abundances of molecular hydrogen within these plumes suggested ongoing hydrothermal activity at temperatures >90^{o}C at the rock-water interface in Enceladus (Hsu et al., 2015; Waite et al., 2017).

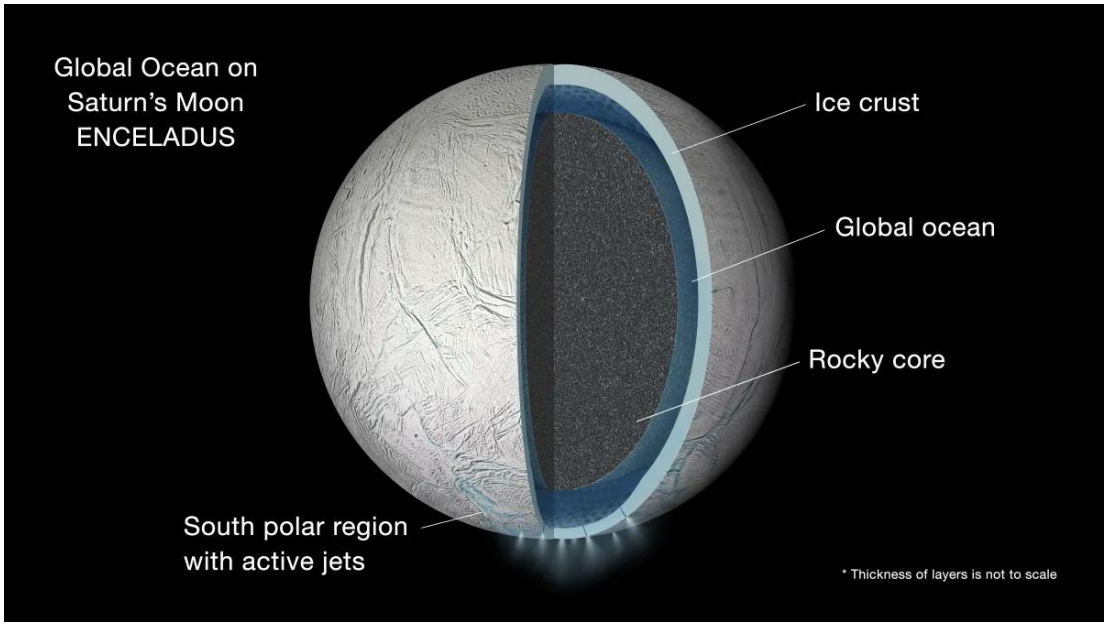

Figure 4. Illustration of the interior of Enceladus, showing a global liquid water ocean in contact with a rocky core and a thick icy crust. At the south polar region of the moon, the active jets eject from the subsurface ocean through the icy crust into space (Taken from NASA).

Hydrothermal activity at Enceladus's seafloor is significant for the potential formation of life in space. The hydrothermal vent origin-of-life theory suggests that on Earth, early life could have formed by harnessing the chemical and energy gradients found surrounding hydrothermal vents (Baross & Hoffman, 1985; Martin et al., 2008). Thus, it is of interest to many astrobiologists to study prebiotic synthesis in conditions relevant to Enceladus (Barge & White, 2017; Marlin et al., 2025) as a similar formation of life is possible. Recent publications report simple and complex organic molecules in the plumes emanating from Enceladus's surface (Khawaja et al., 2019; Postberg et al., 2018b), containing molecules that are necessary to generate and sustain life such as amino acids and nucleotide bases. Understanding their stability and reactivity in hydrothermal conditions relevant to Enceladus's ocean is important to determine their survivability and likelihood of forming more complex biomolecules.

Icy ocean moons like Enceladus are prime locations for the search for life outside of Earth, as liquid water is one of the essential criteria for habitability. For an astrobiology target to be considered habitable, it must meet two other criteria: a source of energy and bioessential elements (Capone et al., 2006; Hoehler et al., 2007; McKay et al., 2014; Shapiro & Schulze-Makuch, 2009). Evidence from the Cassini mission suggests that Enceladus meets the three criteria for habitability. It has a global subsurface liquid water ocean (McKinnon, 2015; Patthoff & Kattenhorn, 2011; Thomas et al., 2016) and a source of energy from the ongoing hydrothermal activity (Hsu et al., 2015; Waite et al., 2017). Additionally, the essential elements required for life (CHONP) have been detected within the materials ejected from the plumes (Khawaja et al., 2019; Postberg et al., 2023; Postberg et al., 2018b; Waite et al., 2017). Considering most biomolecules required for

life are composed of CHONP, the observed elements serve as precursors to such compounds. Furthermore, the detection of organic matter, chemical redox couples (i.e. CO_2 and H_2), and methane can also be a source of energy for microbial communities that utilize these for metabolism (Glein & Waite, 2020; Postberg et al., 2011).

It has been suggested that Enceladus represents the best astrobiology target in the Solar System to search for life beyond Earth. Indeed, there have been many proposed missions to study Enceladus and its plumes via multiple flybys or by landing directly on the icy surface (Cable et al., 2017; Eigenbrode et al., 2018; MacKenzie et al., 2021). Of the different mission concepts, the Enceladus Orbilander seeks to first orbit and then land to determine if Enceladus is inhabited and to what extent the subsurface ocean can sustain life. To answer whether Enceladus is inhabited, several objectives need to be addressed, including the characterization of the volatile and non-volatile materials, the characterization of the amino acid and lipid composition, and the search for evidence of cells and a genetic biopolymer. Regardless of which mission is chosen as the successor to Cassini, the detection and characterization of these materials are likely to determine if Enceladus supports or could have supported life.

1.4 Geomimicry

When exploring how Earth operates and transforms carbon in the deep carbon cycle, it is oftentimes compared to conventional organic chemistry practices. Although this may provide useful insights into organic reaction mechanisms, it commonly falls short in the reaction conditions and additives. For example, traditional organic synthesis uses harsh reagents such as concentrated sulfuric acid or extreme oxidants like chromate or permanganate, while hydrothermal systems conduct similar organic chemistry in only

water with nontoxic materials like minerals or metal salts. For this reason, hydrothermal chemistry has emerged in the field of "geomimicry," which conducts organic reactions under conditions that mimic natural geochemical processes for green chemistry and sustainable applications (Bockisch et al., 2019; Hunter & Savage, 2004; Liu et al., 2013; Yang et al., 2015; Yang & Aspin, 2023).

Geochemically relevant conditions are not extreme, often well below the critical point of water (~150-300^{o}C and vapor-saturation pressures). Even at these mild temperatures, hydrothermal water possesses many properties that are beneficial in green chemistry applications. As discussed in Chapter 1.2, the dielectric constant of water decreases at elevated temperatures. In the temperature range of 250-300^{o}C, the dielectric constant reaches ~20-25, comparable to those of acetone and methanol at ambient conditions of 25^{o}C and 1 atm (ε = 21 and 30, respectively). Because of this property, compounds that readily dissolve in methanol and acetone at room temperature should be soluble in hydrothermal water, making it a suitable organic solvent. Additionally, the elevated dissociation constant (K_w) results in higher concentrations of H^+ and OH^- ions in solution, allowing water to directly participate in organic reactions as an acid- or base-catalyst. Finally, water is the most benign and environmentally abundant liquid, suggesting it is an excellent reaction medium for green chemistry and sustainable reactions or processes.

Hydrothermal conditions have been widely used in a variety of applications. It has been used in the synthesis of nanocomposites such as carbon nanotubes in material science (Kumar & Kumar, 2021; Sonawane et al., 2018) and the organic synthesis of pharmaceuticals such as quinoxalines (Amaya-Garcia et al., 2021), bisimides

(Baumgartner et al., 2017), and benzimidazoles (Dudd et al., 2003). Treatment with hydrothermal methods has also been used during the disinfection of sewage sludge in wastewater treatment and pollutant remediation (Jian et al., 2018; Shi et al., 2013a; Shi et al., 2013b). Additionally, organic wastes such as biomass or plastics have been subject to hydrothermal degradation (Liu et al., 2015; Mohan et al., 2015; Seshasayee & Savage, 2020; Wang et al., 2022). Often, these processes are even further sustainable because they recycle the waste into value-added products such as fertilizers for soil amendment (Shan et al., 2023; Xiong et al., 2021) and fuels for energy (Alherbawi et al., 2021; Madsen & Glasius, 2019; Malhotra & Garg, 2020).

1.5 Research gaps

Herein, the transformations of select organic compounds under relevant hydrothermal conditions are investigated, including alkenes and amino acids. Alkenes represent an important intermediate linking the most reduced form of carbon (alkanes) to the most oxidized form as carboxylic acids. Although studies of individual alkene pathways have been reported (Bockisch et al., 2019; Seewald, 1994; Seewald, 2001; Shipp et al., 2013a; Venturi et al., 2017), how the pathways compete with one another is not fully understood, and in particular, the key geochemical parameters that control their reactions warrant further investigation. Additionally, few studies have explored the influence of inorganic materials such as dissolved metals or minerals on the reaction pathways (Bockisch et al., 2019; Venturi et al., 2017). Thus, this study aims to address this lack of research and to elucidate the individual effects of dissolved metal ions on alkene pathways.

The hydrothermal transformation of amino acids has received considerable attention in relation to hydrothermal research (Estrada et al., 2017; Lee et al., 2014a; Lee et al., 2014b; Lemke et al., 2009; McCollom, 2013; Pedreira-Segade et al., 2019; Sato et al., 2004; Shock, 1992; Shock, 1993), considering they are an important biomolecule necessary to form and sustain life. Hot hydrothermal fluids tend to degrade amino acids, making them unstable around these environments. However, how inorganic materials such as dissolved metal salts influence the reaction pathways or survivability in hydrothermal systems remains relatively unstudied. This study aims to address this research gap by investigating different solution chemistries and compositions on amino acid reactivity. The results suggest that the reactivity of amino acids increases with increasing temperatures and is dependent on solution pH, indicating the overall charge may control the stability of amino acids. Furthermore, inorganic salts enhance the stability of amino acids in hot hydrothermal solutions, suggesting a protective role of metals in their organic transformations. In alkaline conditions and solutions of high ionic strength, similar to the expected chemistry of Enceladus's ocean, the survivability of amino acids is enhanced. This suggests that amino acids may be more preserved in hydrothermal conditions than originally thought, which has implications for prebiotic synthesis and the origin of life considering amino acids must be stable in solution long enough to enable the formation of peptides and proteins. The enhanced stability of this type of biosignature is also relevant to the search for life, as amino acids are more preserved in extraterrestrial oceans, thus increasing the likelihood of detection.

However, biosignature detection in icy ocean worlds is difficult, owing to the thick layer of ice surrounding the underlying liquid ocean of interest. Enceladus displays

surface activity in the form of plumes ejecting from the icy surface, which can be targeted in future missions and used to infer the characteristics of the subsurface liquid ocean. This study seeks to investigate how the transition from liquid in the subsurface liquid ocean to vacuum above the surface affects the relative abundances of biosignatures such as amino acids and fatty acids, which are two of the five objectives that are sought to investigate on Enceladus by the Enceladus Orbilander (MacKenzie et al., 2021). Injection of amino and fatty acids indicates that relative abundances of the materials are sufficiently conserved to allow for distinction between biological and abiotic sources, suggesting biosignature analysis in future search-for-life missions may accurately identify the source of the organic compounds.

Finally, the green and sustainable degradation of plastic under hydrothermal conditions is investigated here. Recycling of plastic typically consists of mechanical breakdown of wastes and remelting it into a new product, however, this requires separation of the different types of plastics, making recycling difficult and time-consuming. Storage of plastic waste in landfills and incineration also poses a risk to ecosystems, considering toxic additives and chemicals can easily enter the surrounding environment, posing a danger to the health of many organisms (Shen et al., 2020). This shows an urgent need to find an alternative method to recycle plastic waste. Although there have been studies on the degradation of plastics in hot water (Gentilcore et al., 2024; Hongthong et al., 2020; Musivand et al., 2023; Seshasayee et al., 2021; Seshasayee & Savage, 2020; Seshasayee & Savage, 2021; Thunman et al., 2019; Zhao et al., 2018a), the conversion and product selectivity greatly depend on the plastic structure. Additionally, the influence of inorganic materials such as minerals or dissolved salts has

rarely been explored. This study seeks to further improve the sustainability of hydrothermal plastic degradation by utilizing Earth-abundant minerals to help facilitate the conversion.

CHAPTER TWO

EXPERIMENTAL AND THEORETICAL INVESTIGATION OF ALKENE TRANSFORMATIONS IN OCEANIC HYDROTHERMAL FLUIDS: A MECHANISTIC STUDY OF STYRENE

2.1 Introduction

Hydrothermal transformations of organic compounds are unique and important for many geological processes. Maturation of organic matter results in the production and accumulation of oil and natural gas deposits (Helgeson et al., 2009; Jones et al., 2008; Larter et al., 2003; Seewald, 2003), while methane and labile organic compounds in hydrothermal systems are sources of metabolic energy and nutrients for the microbial life in the subsurface biosphere (Amend et al., 2011; Dick, 2019; Horsfield et al., 2006; McCollom & Seewald, 2007). Hydrothermal systems are also thought to mimic conditions where organic precursors of life may have originated, and many studies have focused on the abiotic origin of important biomolecular precursors (Fu et al., 2020c; LaRowe & Regnier, 2008; Ménez et al., 2018; Robinson et al., 2021a; Shock & Canovas, 2010; Shock & Schulte, 1998). Studies of these organic hydrothermal reactions are not only relevant to prebiotic synthesis on early Earth, but could also be indicative for potential of life in other planets and icy moons (Barge et al., 2019; Postberg et al., 2018b). Identifying the pathways and mechanisms of organic compounds is critical to understand their generation, preservation, and degradation during the hydrothermal geochemical processes.

Organic functional group interconversions under hydrothermal conditions between alkanes, alkenes, alcohols, ketones/aldehydes, and carboxylic acids have been

proposed and experimentally validated (Figure A1). Alkenes (with C=C double bonds) are commonly observed in natural hydrothermal environments, such as in the structures of unsaturated petroleum or lipids. As a key intermediate linking alkanes and other functional groups, alkenes are known to hydrogenate to alkanes under hydrothermal conditions (Seewald, 1994; Yang et al., 2012), hydrate to form alcohols (Seewald, 2001; Shipp et al., 2013a), and to further be reduced by dissolved molecular hydrogen or minerals via water-mineral/metal interactions (Bockisch et al., 2019; Venturi et al., 2017). A recent study also suggests that alkenes can be potentially oxidized by metal salts to form aldehydes in hydrothermal solutions, possibly through an ozonolysis-like oxidative C=C bond cleavage pathway (Liao et al., 2021). However, how these alkene reaction pathways compete with each other in complex hydrothermal systems is unknown, and in particular, the key geochemical factors controlling alkene hydrothermal transformations is not well understood, which warrants further investigation.

In hydrothermal fluids, natural organic matter is usually surrounded by inorganic materials such as minerals and dissolved metal salts, which can significantly influence organic geochemical transformations (McCollom, 2013; Seewald, 2003). Previous studies have shown that organic-mineral/metal interactions could control the chemistry and transformation of organic functional groups under hydrothermal conditions. As examples, reduction of alkenes to alkanes can be catalyzed by iron and nickel (Bockisch et al., 2019); dehydrogenation of cycloalkanes to benzene can be facilitated in the presence of iron oxide minerals (Venturi et al., 2017); reduction of ketones to alcohols can be promoted by iron sulfide minerals (Yang et al., 2018); and oxidation of alcohols to aldehydes/ketones, as well as oxidation of aldehydes to carboxylic acids, can be driven

by copper or iron salts (Liao et al., 2021; Liao et al., 2022). Nevertheless, few studies have investigated the interactions between alkenes and dissolved metal salts, which limits our understanding of the fate and transformation of natural organic matter containing C=C bonds in oceanic hydrothermal systems.

Herein, we conduct a combined theoretical and experimental investigation on the hydrothermal transformation of alkenes. Styrene is selected as a model aromatic alkene to study, because its benzylic structure not only supports a higher reactivity but also allows for facile product extraction and quantitative analysis. Although both aliphatic and aromatic alkenes are present in natural hydrothermal systems, similar reaction mechanisms and pathways could be expected. The goals of this study are to (a) identify the reaction pathways and mechanisms of alkenes in hydrothermal systems, (b) examine the key geochemical parameters in alkene hydrothermal reactions, and (c) investigate the effects of dissolved metal salts on alkene transformations. Metal salts including iron, copper, aluminum, zinc, and sodium are chosen to study because they are widely distributed and discharged from seafloor hydrothermal vents in relatively high quantities (Sander & Koschinsky, 2011).

2.2 Experimental and Modeling Methods

Hydrothermal experiments were conducted following methods developed in previous studies (Fu et al., 2020a; Liao et al., 2021; Yang et al., 2014; Yang & Fu, 2018). Briefly, styrene was injected into fused-silica glass tubes (6 mm OD × 2 mm ID), and deoxygenated water (18.2 MΩ) or metal salt solutions with and without phosphate buffer (PBS) was subsequently added using a gas-tight micro-syringe. The initial concentrations of styrene and metal ions were both 0.1 molal. Although the chosen concentrations of

alkene and metal ions could be higher than those expected in natural hydrothermal systems, it allows the major products and reaction pathways to be fully identified in current laboratory-simulated systems. Experiments were also conducted starting with styrene oxide, styrene glycol, and 1-phenylethanol, with starting concentrations of 0.1 molal for each experiment. After the starting reagents were loaded, the oxygen and air inside the tubes were removed by three freeze-pump-thaw cycles. The tubes were then sealed using an oxyhydrogen flame under vacuum while submerged in liquid nitrogen. The sealed tubes were then heated at 150°C and 5 bar (P_{sat}) for a specific amount of time (0.5–72 hr). These experimental conditions were chosen to represent a relatively mild hydrothermal environment, which allows the alkene pathways and mechanisms to be readily studied.

The reactions were quenched by submerging the tubes in a cold-water bath, and the reaction products were subsequently acidified with HCl and extracted with dichoromethane containing decane as an internal standard. The solution mixtures were then vortexed and centrifuged to ensure separation of the organic products from the aqueous layers. The organic layers were collected and subsequently analyzed by an Agilent 7820A gas chromatography (GC) equipped with a poly-capillary column and a flame-ionization detector. Calibration curves for starting reagents and products were prepared using analytical standards and used to quantify the product concentrations from GC. Products were also identified using GC-mass spectrometry (Agilent 7820A/5975C) based on database matching and fragmentation patterns.

Geochemical calculations of alkene reactions were performed using the revised Helgeson-Kirkham-Flowers (HKF) equation of state, as implemented in SUPCRT92

(Johnson et al., 1992). Model alkene compounds (C3-C6) were used as representative alkenes because of their availability in the database and their relatively simple structure. The equilibrium constants (K_{eq}) for alkene oxidation and hydration were calculated along the water liquid-vapor saturation curve. The specific reactions and calculations are described in further detail in Section 2.4. The software package EQ3/6 (implementing HKF equations of state) (Wolery, 1992) was used to calculate the correct proportions of phosphate species to reach the desired pH at the experimental temperatures. EQ3/6 was also used to calculate the distribution of major aqueous copper species under hydrothermal conditions.

2.3 Results and Discussion

Under the experimental conditions of 150°C and 5 bar, three major reaction pathways are observed for styrene: (a) hydration to form 1-phenylethanol, (b) dimerization to form 1,3-diphenylbutene, and (c) oxidation to form benzaldehyde (Figure 5). Besides these major products, secondary and minor products such as acetophenone, phenylacetaldehyde, and styrene glycol are also observed but in very small amounts (<5 mol% of all products). To compare the relative distribution of each pathway, pathway% (i.e., hydration%, dimerization%, and oxidation%) are quantitatively calculated by summing up the mole% of products formed in each pathway respectively.

2.3.1 Hydration of Alkenes

Hydration is the major hydrothermal pathway for styrene, especially under acidic conditions. Hydration of styrene forms 1-phenylethanol as the major product, which can be subsequently oxidized to acetophenone as a minor product. In acidic solutions (pH 3, Figure A2, Table A1), 1-phenylethanol accounted for 22% of total products after 6 hr and

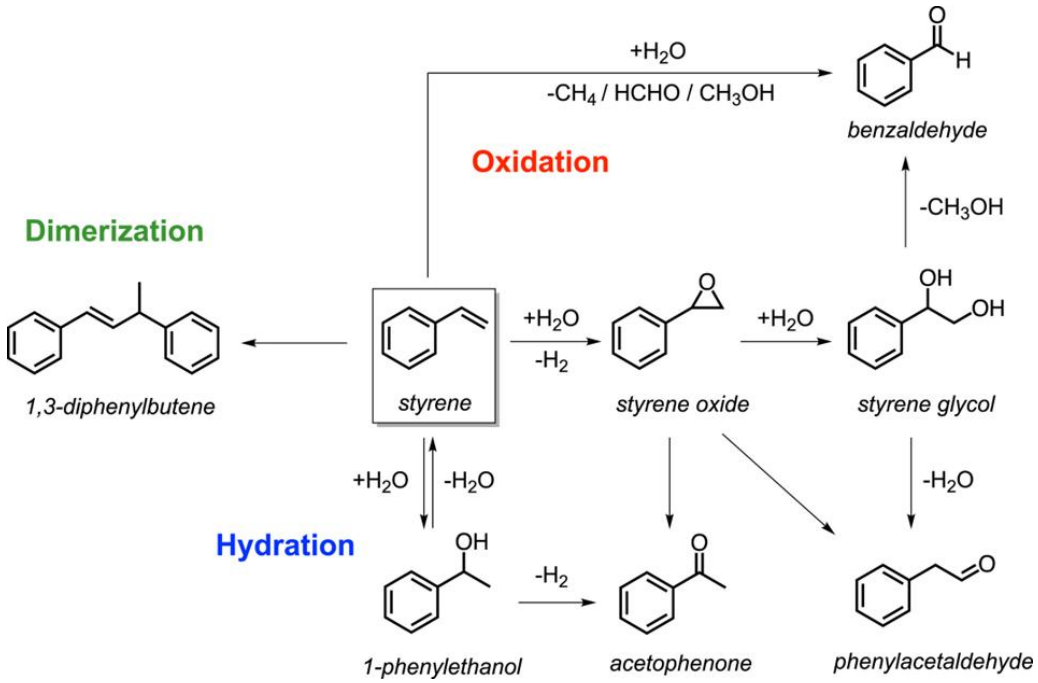

Figure 5. Proposed major reaction pathways for styrene in hydrothermal systems (Taken from Aspin et al., 2023).

stabilized at 29 mol% after 24 hr. The accumulation of 1-phenylethanol corresponds to the decrease of styrene, which reduced to 66 mol% after 24 hr. Compared to acidic conditions, near neutral (pH 5.8) and basic (pH 7.8) conditions (at 150°C) do not favor alkene hydration, with <1 mol% 1-phenylethanol formed after 24 hr (Figure A2). In fact, the degradation of styrene is substantially slower under near neutral and basic conditions, with less than 5 mol% degraded after 24 hr. The results suggest that alkenes have a much higher reactivity in acidic hydrothermal fluids but a higher stability under non-acidic hydrothermal conditions. The extent of alkene hydration is further studied as a function of solution pH (Figure 6a). The hydration pathway% of styrene increases with decreasing solution pH, which were 8.5% and 30.8% at pH 4.5 and 2.5, respectively. In comparison, only 1.3% hydration pathway was observed at near-neutral pH (5.8) and no hydration was detected at pH 7.0 at 150°C. The results suggest that the hydrothermal hydration of

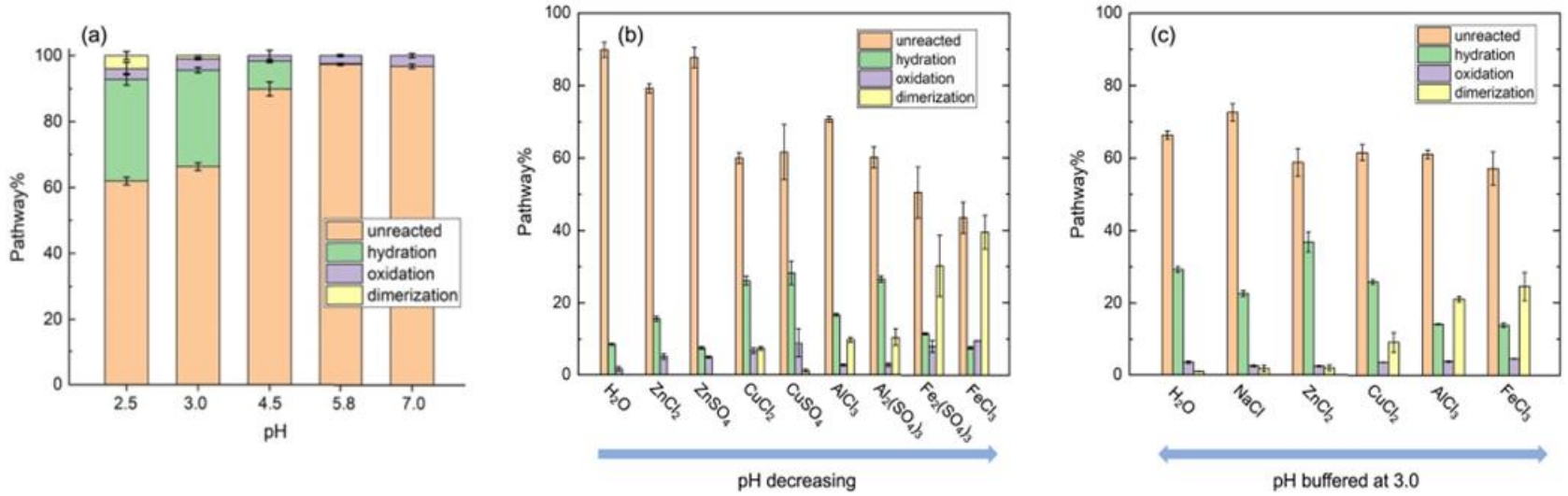

Figure 6. Pathway distribution for styrene as a function of pH (a) and influence of dissolved metal salts on hydrothermal reactions of styrene in unbuffered (b) and pH-buffered (c) solutions at 150°C and P_{sat} after 24 hr. The unbuffered metal salt solutions (b) have a decreasing pH (increasing acidity) from left to right, while the buffered solutions (c) have a constant pH of 3.0 for all metal salts with the PBS buffer (Taken from Aspin et al., 2023).

alkenes is strongly pH-dependent and driven by the acidity in the fluids.

Hydration of styrene mostly occurring in acidic solutions is consistent with an acid-catalyzed reaction mechanism. Hydrolyzing a C=C double bond usually involves protonation to form a carbocation intermediate, which can be catalyzed by Lewis or Brønsted acids such as hydronium ions. At lower pH values, the high concentration of hydronium ions can greatly facilitate the electrophilic addition of protons to the alkene. Subsequently, the addition of water to the carbocation forms an oxonium ion, which then deprotonates to produce the alcohol. Because only 1-phenylethanol (a secondary alcohol) is observed, it can be inferred that this pathway occurs via a Markovnikov hydration mechanism (Beller et al., 2004). This mechanism results with the addition of the hydroxyl group to the most substituted carbon (i.e., the benzylic carbon), which occurs due to the generation of the most stable carbocation along the double bond. Although an anti-Markovnikov hydration mechanism is also possible, the absence of the primary alcohol (2-phenylethanol) suggests that it is not favorable under hydrothermal conditions.

In addition to the hydration pathway producing 1-phenylethanol as the major product, a small amount of acetophenone (<1 mol%) is also observed, most likely through the oxidation of 1-phenylethanol. A previous study of alcohols under similar hydrothermal conditions reported that 1-phenylethanol can be oxidized to acetophenone in water at 200°C and 15 bar (P_{sat}) (Liao et al., 2021). That study also showed that dehydration of 1-phenylethanol readily occurs under hydrothermal conditions, which suggests a reversible interconversion between styrene and 1-phenylethanol as shown in Figure 5. In the present study, styrene degradation and 1-phenylethanol formation leveled

off after 12 hr (Figure A2), suggesting alkenes and alcohols could reach a metastable equilibrium at longer reaction times under the experimental conditions.

In addition to the hydration pathway producing 1-phenylethanol as the major product, a small amount of acetophenone (<1 mol%) is also observed, most likely through the oxidation of 1-phenylethanol. A previous study of alcohols under similar hydrothermal conditions reported that 1-phenylethanol can be oxidized to acetophenone in water at 200°C and 15 bar (P_{sat}) (Liao et al., 2021). That study also showed that dehydration of 1-phenylethanol readily occurs under hydrothermal conditions, which suggests a reversible interconversion between styrene and 1-phenylethanol as shown in Figure 5. In the present study, styrene degradation and 1-phenylethanol formation leveled off after 12 hr (Figure A2), suggesting alkenes and alcohols could reach a metastable equilibrium at longer reaction times under the experimental conditions.

2.3.2 Dimerization of Alkenes

Dimerization of styrene to form 1,3-diphenylbutene is also observed, but only under acidic conditions. As shown in Figure 6a, no dimerization was detected at or above pH 4.5 after 24 hr, where it accounted for 0.9% and 3.9% of all products at pH 3.0 and 2.5, respectively. The dimerization pathway follows a similar pH-dependent trend as the hydration pathway; more dimerization occurs when the solution pH is lower. This suggests that alkene hydrothermal dimerization is also acid-catalyzed, which is in line with previous studies showing Lewis acids can catalyze the reaction (Mayo, 1968; O'Connor & Kojima, 1990). The proposed mechanism for alkene dimerization involves protonation of the C=C π-bond by an acid to form a carbocation intermediate, followed by electrophilic addition of another alkene, and subsequent β-hydrogen elimination to

produce the dimer (Figure A3). However, the solution pH may not be the only driver for dimerization of alkenes under hydrothermal conditions, as metal-anion complexes formed at elevated temperatures and pressures can potentially play another role in alkene transformations (see Section 2.4).

2.3.3 Oxidation of Alkenes

A third pathway for styrene is the oxidation pathway, which forms benzaldehyde as the major product, along with minor products including styrene glycol, acetophenone, and phenylacetaldehyde (Figure 5). As a primary oxidation product from styrene, benzaldehyde was formed in small and comparable amounts (1.6–5.4 mol% after 24 or 72 hr) in the acidic, neutral, and basic hydrothermal experiments (Figure A2), where the other minor products accumulated in even smaller amounts with a total concentration <1 mol%. The oxidation pathway% after 24 hr between pH 2.5 and 7.0 were 1.6%–3.4% (Figure 6a), suggesting the alkene oxidation was not significantly affected by the change of solution pH.

Formation of benzaldehyde from styrene requires breaking a C=C double bond and forming a C=O bond, which could be associated with an oxidative cleavage mechanism. A previous study reported a copper(II)/iron(III)-promoted oxidation pathway from 1-phenylethanol to benzaldehyde via styrene under similar hydrothermal conditions, which suggested an ozonolysis-like oxidative alkene cleavage mechanism (Liao et al., 2021). Oxidative cleavage of styrene to benzaldehyde in aqueous media has also been reported using heterogeneous catalysis and air as the oxidant (Batra et al., 2019; Schäfer et al., 2018). Although the present study differs from the other work that uses strong oxidizing metals or air as the oxidant, it is likely that a similar mechanism could apply to

alkene oxidation under anoxic hydrothermal conditions. Furthermore, during the conversion from styrene to benzaldehyde, a carbon atom is removed. However, due to the extremely low concentration and detection challenges, it remains unclear which form of carbon (e.g., methane, methanol, or formaldehyde) should be present. Geochemical modeling is thus used to compare the likelihood of these oxidation reactions at equilibrium (see Section 2.4).

Although styrene oxide was not detected in hydrothermal experiments with styrene, reactions starting with styrene oxide indicated that the epoxide is highly reactive and can convert to styrene glycol (66 mol%), phenylacetaldehyde (12 mol%), and acetophenone (1.5 mol%) within 15 min (data not shown). Results also show that benzaldehyde (19 mol%) is formed from styrene oxide, which suggests an alternative pathway via styrene glycol (Figure 5). Indeed, hydrothermal experiments starting with styrene glycol confirmed that benzaldehyde and phenylacetaldehyde can be generated from styrene glycol within hours under the same experimental conditions (Figure A4). Proposed reaction mechanisms are provided in Figure A5.

2.3.4 Influence of Metal Salts

To examine the potential roles of dissolved metal salts in alkene hydrothermal pathways, a series of styrene experiments were conducted in chloride or sulfate solutions with zinc(II), copper(II), aluminum(III), and iron(III) (Figures 6b and 6c). Zinc chloride/sulfate do not significantly alter the reactivity or pathways of styrene, however, copper, aluminum, and iron salts all increase the decomposition of styrene and selectively change the pathway distribution. Specifically, in the presence of copper or aluminum salts, the hydration pathway% is facilitated by 8%–20% compared to water alone, while

the dimerization pathway% is increased by 1%–10% (Figure 6b, Table A2). In the iron chloride/sulfate solutions, the hydration pathway% is relatively unaffected, but surprisingly, the dimerization pathway% is promoted substantially by 30%–39% and becomes the dominant pathway, which results in a 39%–46% increase of alkene reactivity. Compared to hydration and dimerization, the oxidation pathway% appears to be less influenced by the metal salts, which shows an increase of 1%–8%, most evident in the presence of copper and iron salts.

The pH of metal salt solutions could differ from each other, depending on the type and concentration of metal ions and their counterions. Although the solution pH at the experimental conditions was not feasible to measure, the relative acidity between the metal salts could be speculated by those measured at room temperature (Table A3). The increased acidity introduced by the metal salts can potentially drive the acid-catalyzed hydration or dimerization of alkenes. Indeed, as shown in Figures 6a and 6b, a pH-dependent trend is observed for the alkene reactivity, in which a higher alkene reactivity or decomposition rate is associated with a higher acidity. With pH decreasing, the hydration and dimerization pathways become more dominating, which is consistent with the proposed acid-catalyzed mechanisms. However, the effect of metal salts on alkenes is not only driven by the solution pH. Figure 6c shows that dimerization is significantly promoted by the iron(III), copper(II), and aluminum(III) salts, even when buffered at the same pH. This is in stark contrast to the hydration pathway, which is not enhanced in the presence of metal chlorides when buffered at the same pH. This suggests that alkene hydration is primarily influenced by the change in pH of the solution when metal salts are

present, whereas dimerization is also driven by the direct interaction between the alkene and metal salts, likely via a complexation process (see Section 2.4).

As described earlier, the mechanism of alkene dimerization likely undergoes a cationic intermediate, which can be catalyzed by Lewis acids (Figure A3). $FeCl_3$ is a commonly used Lewis acid in organic synthesis, which is expected to facilitate the protonation of alkenes. A previous study showed that $FeCl_3$ salt is an efficient catalyst for dimerization of diarylalkenes in organic solvents (Ma & Zhao, 2018), and an $FeCl_3$-based system was also used to initiate the cationic polymerization of isobutylene in dichloromethane (Liu et al., 2011). Although the reaction medium and conditions are quite different from the present study, a similar mechanism may apply to the $FeCl_3$-catalyzed alkene dimerization under hydrothermal conditions. In fact, it has been estimated that up to 22% of deep-ocean dissolved Fe could come from submarine hydrothermal venting (Bennett et al., 2008), which forms complexes that may potentially serve as Lewis acids.

As a non-Lewis acid and non-redox metal compound, both sodium and zinc chloride tend to be minor drivers of organic transformations under hydrothermal conditions. Previous studies of the effects of metal salts on other organic functional groups such as alcohols and aldehydes in hydrothermal systems also showed a relatively inert effect of sodium salts (Liao et al., 2021; Liao et al., 2022). The different controls of alkene pathways by metal salts further demonstrate an important selectivity of dissolved metal species on organic hydrothermal transformations. Not only the fluid pH, but the type and speciation of metal salts can also be determining factors for such organic geochemical processes.

2.4 Geochemical Calculations and Implications

Geochemical calculations were performed to test against the experimental results and to obtain additional information that could be useful to understand alkene transformations in complex hydrothermal environments. In the context of organic functional group interconversions (Figure A1), alkenes can undergo either hydrogenation to form alkanes or hydration to form alcohols, which have been reported in previous studies (Seewald, 2003; Shock et al., 2013). In the present study, however, it is shown that alkenes can also follow an alternative oxidation pathway that directly forms aldehydes under hydrothermal conditions (Figure 5). Thermodynamic calculations predict that this new oxidation pathway of alkenes can occur and even compete with the hydration pathway at increased temperatures and pressures. For example, hydration of alkenes to form alcohols can be modeled by the following general reaction (Equation 1),

$$C_nH_{2n\,(aq)} + H_2O \leftrightarrow C_nH_{2n+1}OH_{\,(aq)} \quad (1)$$

where n ($\geq$2) represents the number of carbons in the starting alkene structure. As shown in Figure 7a, the calculated log K_{eq} for the hydration of simple alkenes are mostly positive between 25 and 300°C but decrease with increasing temperatures. The positive log K_{eq} supports that alkene hydration is thermodynamically favorable at the experimental conditions of 150°C, whereas that decreasing trend of log K_{eq} with temperature suggests that alkene hydration could become less likely at higher temperatures. It should also be noted that the calculated log K_{eq} values between the model alkenes at the same temperature can be orders of magnitude different, which suggests that the tendency of hydration could also be determined by the structure of alkenes. Similar

observations are also reported in the geochemical modeling of alcohol dehydration using multiple alcohol structures (Liao et al., 2021).

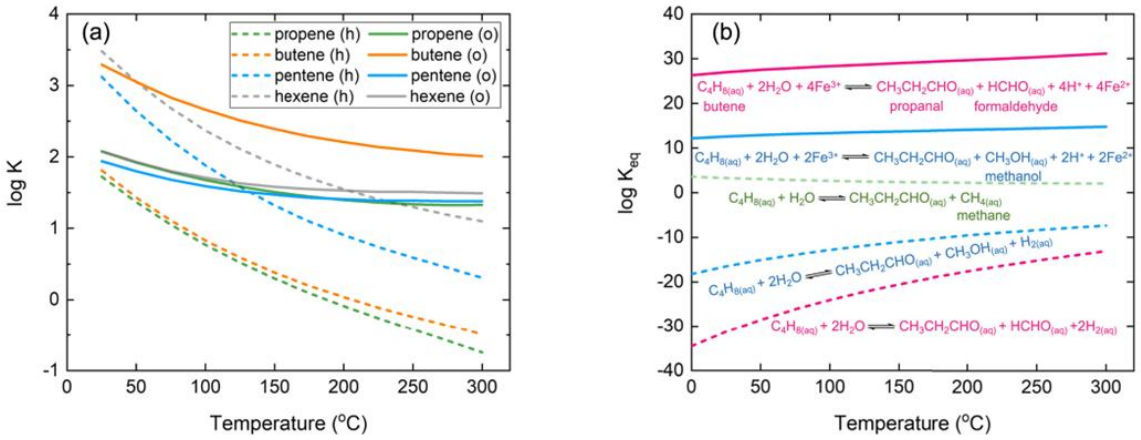

Figure 7. Calculated equilibrium constants (log K_{eq}) for C3-C6 alkene hydration (h) and oxidation (o) reactions (a) and for 1-butene oxidation w/wo Fe^{3+} in water (b) as a function of temperature (Taken from Aspin et al., 2023).

Compared to the hydration pathway, the oxidation pathway from alkenes to aldehydes can be represented by the following reaction (Equation 2)

$$C_nH_{2n\,(aq)} + H_2O \leftrightarrow C_{n-1}H_{2n-2}O_{(aq)} + CH_{4\,(aq)} \quad (2)$$

It shows that log K_{eq} for the oxidation of alkenes also decrease with increasing temperature, but with a much slower trend than that of the hydration of alkenes (Figure 7a). The slower decreasing trend of log K_{eq} suggests that the oxidation of alkenes could become more favorable than alkene hydration above certain temperatures, which in fact is consistent with the experimental results of styrene under neutral and basic conditions at 150°C (Figure A2). But again, the tendency for each pathway to occur is likely determined by the structure and chemical property of alkenes, as the cross point of log K_{eq} between hydration and oxidation varies depending on the alkene structure (Figure 7a).

It is also important to note that modeling of alkene oxidation is conducted under the assumption that methane (CH_4) is formed as a byproduct, however, methanol (CH_3OH) or formaldehyde (HCHO) may also form as potential byproducts (Figure 5). Thermodynamic calculations show that the log K_{eq} for oxidation of 1-butene with the formation of methane is significantly higher than those with the formation of methanol or formaldehyde (Figure 7b), suggesting methane could be more favored to form than the other C1 products under hydrothermal conditions.

The presence of oxidizing metal salts such as iron(III) and copper(II), however, may potentially affect the alkene oxidation pathway and change the product distribution. For example, the calculated log K_{eq} for alkene reactions with Fe^{3+} forming formaldehyde or methanol show orders of magnitude increase than those in water alone (Figure 7b). Thermodynamic calculations on aqueous metal speciation also indicate that the form of metal complexes rather than the freely diffused ions is preferred under hydrothermal conditions. Distribution of aqueous copper species as a function of temperature shows that $CuCl^+$ becomes the dominating species at elevated temperatures (Figure A6). Due to their relatively high solubility and prevalence in hydrothermal vents, metal ions such as iron and copper tend to form strong complexes with organic ligands (Yang et al., 2015). In deep-sea water, more than 98% of dissolved iron could be in complexation with organic compounds (Sander & Koschinsky, 2011). The complexed forms of metal salts in hydrothermal solutions are therefore most likely to play the key role in alkene transformations.

In addition, the shift of log K_{eq} from negative to positive suggests that the presence of oxidizing metal ions (e.g., Fe^{3+}) could drive the thermodynamics and make

selective pathways (e.g., methanol or formaldehyde formation) more favored for alkene oxidation. These modeling results are also consistent with the experimental findings, in which an increased alkene oxidation pathway% is observed in the iron(III) salt experiments (Figure 6). The consistency between modeling and experimental results further suggests that hydrothermal oxidation of alkenes can be influenced by dissolved metal salts, similar to those observed for other functional groups such as alcohols and aldehydes (Liao et al., 2021; Liao et al., 2022). In submarine hydrothermal systems, hydrothermal fluids can be enriched with dissolved metals that have much higher concentrations than those in the surrounding seawater (Tagliabue et al., 2017). This would allow sufficient interactions to occur between metal salts and organic compounds, which could determine the fate and distribution of organic carbon in the deep ocean. Taken together, these findings imply strong and selective roles of aqueous metal species in organic functional group interconversions, which not only control the existing pathways but also initiate new pathways for organic geochemical transformations in natural hydrothermal systems.

2.5 Conclusions

This work examines the transformation pathways and reaction mechanisms of alkenes under geologically relevant hydrothermal conditions. Among the three major pathways of alkenes, acid-catalyzed hydration and dimerization are strongly pH-dependent and become more favorable in lower-pH hydrothermal fluids, while the oxidation of alkenes remains relatively constant over the pH range. Transformation pathways of alkenes can also be significantly influenced by the presence of aqueous metal salts. Dissolution of metal salts with increasing acidity lowers the solution pH and

expedites the alkene hydration. Dimerization of alkenes is not solely driven by solution pH, but it can also be facilitated by specific metal salts such as iron/aluminum chloride, which serve as efficient Lewis acid catalysts. Enhanced oxidation of alkenes occurs in the presence of oxidizing metal salts such as iron(III) and copper(II), which potentially change the redox of hydrothermal solutions. The experimental results also agree with the modeling predictions, which further corroborate the thermodynamic drives for these reactions under hydrothermal conditions. This study provides another example of organic functional group interconversions during hydrothermal geochemical processes, which also highlights that fluid chemistry and metal salt content are determining factors for the fate and transformations of natural organic matter in oceanic hydrothermal environments.

CHAPTER THREE

SURVIVABILITY AND PATHWAYS OF AMINO ACIDS IN OCEANIC HYDROTHERMAL SYSTEMS: A MECHANISTIC STUDY OF PHENYLALANINE

3.1 Introduction

Deep-ocean hydrothermal systems are unique and benign environments for natural organic matter transformations. Water at elevated temperatures and pressures not only serves as an excellent organic solvent but also catalyzes organic reactions by acting as an acid or a base (Akerlof & Oshry, 1950; Akiya & Savage, 2002; Shock et al., 2013; Shock, 1993). Synthesis and degradation of organic molecules in natural hydrothermal systems may provide a source of energy and nutrients for subsurface life (Amend et al., 2011; McCollom & Seewald, 2007). These environments are also thought to serve as a model for conditions where biologically relevant molecules necessary for life could have originated (Martin et al., 2008; Wimmer et al., 2021). To understand the generation and preservation of biomolecular precursors in oceanic hydrothermal environments, it is imperative to identify the reactivity and pathways of organic compounds with diverse structures. Indeed, there has been extensive research on studying the pathways and mechanisms of organic functional group transformations in geologically relevant hydrothermal systems, ranging from alkanes (the most reduced carbon) (Reeves et al., 2012; Seewald, 1994, 2003), to alkenes (Aspin et al., 2023; Seewald, 1994; Shipp et al., 2013a; Venturi et al., 2017), alcohols (Bockisch et al., 2018; Liao et al., 2021), aldehydes/ketones (Fecteau et al., 2019; Liao et al., 2022; Yang et al., 2012, 2018), and carboxylic acids (the most oxidized carbon) (Fu et al., 2020a; Glein et al., 2020; Johnson-

Finn et al., 2021; McCollom & Seewald, 2003). These studies uncover many unique organic chemistry and geochemical pathways that only occur under hydrothermal conditions.

Many of the biological molecules essential for life contain not only carbon but also nitrogen (N) in their structures, such as amino acids and proteins. Organic N is widely distributed in submarine hydrothermal vents on Earth, where their abiotic synthesis could be supporting the deep biosphere in those extreme environments (Amend & Shock, 1998; Barge et al., 2019; Fu et al., 2020c; McDermott et al., 2015; Ménez et al., 2018). N-containing organics are also found in icy ocean worlds such as Saturn's moon Enceladus, where amines and amino acids have been detected in the ice grains emitted from the surface plumes (Khawaja et al., 2019; Postberg et al., 2018b). It is also thought that organic N could be synthesized in extraterrestrial hydrothermal vents such as those expected inside Enceladus, where the distribution and relative abundance of organic N (e.g., enantiomeric excesses of amino acids) may serve as potential biosignatures for life detection beyond Earth (Glavin et al., 2020; Neveu et al., 2024b).

As the key building block of proteins, amino acids are among many important classes of organics that have been studied in the origin of life and astrobiology research within the context of hydrothermal environments (Amend & Shock, 1998; Barge et al., 2019). The hydrothermal stability and reaction pathways of amino acids have been previously studied. Simple amino acids such as glycine, alanine, and aspartic acid are examined under a range of hydrothermal conditions, in which major pathways including deamination, hydrolysis, decarboxylation, and polymerization are observed (Estrada et al., 2017; Körner, 2021; Lemke et al., 2009; McCollom, 2013; Pedreira-Segade et al.,

2019; Sato et al., 2004; Shock, 1992). These amino acid transformation pathways, however, are also expected to be influenced by the hydrothermal solution chemistry and composition, including the presence of inorganic materials such as minerals and dissolved metals. Mineral assemblages such as pyrite-pyrrhotite-magnetite and magnetite-hematite are known to control the activity of aqueous H_2, which is an important variable affecting the redox state and metastable equilibrium of organic species in hydrothermal systems (Shock & Canovas, 2010). Experimental studies on the influence of redox state on amino acid stability under hydrothermal conditions show that dissolved H_2 could suppress the decomposition of amino acids, thereby facilitating their persistence in natural hydrothermal systems (Lee et al., 2014a; Lee et al., 2014b). Previous studies also show that common metal salts such as iron and copper chlorides are effective in changing the transformation pathways of carboxylic acids, alcohols, alkenes, and amides under relevant hydrothermal conditions (Aspin et al., 2023; Fu et al., 2020a; Fu et al., 2020b; Liao et al., 2021). However, it remains largely unknown how Earth-abundant metal salts would affect the hydrothermal stability and pathways of amino acids, which could limit our understanding of the fate of organic N in natural hydrothermal systems.

Herein, we investigate the hydrothermal transformation of amino acids under geologically relevant hydrothermal conditions (e.g., 225–275^{o}C, pH 1.3–8.5), using phenylalanine as a model compound. Phenylalanine is one of the canonical amino acids with an aromatic structure, which is relatively reactive because of the benzylic carbon. Phenylalanine has been detected in both high- and low-temperature hydrothermal vents in the deep sea such as the East Pacific Rise (Longnecker et al., 2018) and the Guaymas

Basin (Haberstroh & Karl, 1989). The presence of phenylalanine was mainly attributed to biological sources and activities near the vents, however, recent studies have also suggested that aromatic amino acids such as tryptophan may have been formed abiotically through Friedel-Crafts reactions and preserved at depths beneath the Atlantis Massif in Mid-Atlantic Ridge (Ménez et al., 2018). There have also been laboratory-simulated experiments to study the degradation rates of phenylalanine under hydrothermal conditions (Abdelmoez et al., 2010; Changi et al., 2012; Sato et al., 2004; Vallentyne, 1964), but detailed examination of degradation pathways and product distributions is lacking, and the interaction between phenylalanine and metal salts has yet to be widely explored. The goals of this study are to 1) identify the stability and reaction pathways of phenylalanine under geologically relevant hydrothermal conditions, 2) determine the key geochemical parameters that govern amino acid transformations, and 3) examine the effects of dissolved metal salts on the product distribution and survivability of amino acids in hydrothermal systems.

3.2 Experimental and Modeling Methods

Hydrothermal experiments were conducted following previously developed methods (Fu et al., 2020c; Yang & Fu, 2018). Briefly, 0.3 mL of phenylalanine (0.07 molal) in Ar-purged deionized (DI) water or metal salt solutions (0.05-1.0 molal) was injected into fused silica glass tubes (6 mm OD × 2 mm ID) using a gas-tight glass syringe. The oxygen in the tubes was then removed by three freeze-pump-thaw cycles and the tubes were sealed using an oxyhydrogen flame under vacuum while submerged in liquid nitrogen. Once thawed, the glass tubes were placed in a pre-heated gas chromatography (GC) oven at the desired temperature under vapor-saturation conditions

(P_{sat}). Hydrothermal experiments of phenylalanine were conducted in replicates at three reaction temperatures (225ºC, 250ºC, and 275ºC) for up to 24 hrs. Phenylalanine experiments under different pH conditions (in-situ pH 1.3 – 8.5), and in the presence of different inorganic salts (e.g., $FeCl_3$, $FeCl_2$, $CuCl_2$, $CuSO_4$, $AlCl_3$, $MgCl_2$, and NaCl), were also conducted at 275ºC and P_{sat}. Additional experiments starting with 2-phenylethylamine (0.05 molal) in DI water or metal salt solutions (e.g., 0.05–1.0 molal of $AlCl_3$, $CuCl_2$, $FeCl_3$, and NaCl) have also been investigated at temperatures of 175ºC, 225ºC, and 275ºC. After the reaction, the tubes were removed from the oven and placed into a cold-water bath to immediately quench the reaction.

The samples were extracted and analyzed following previously developed methods (Aspin et al., 2023; Neveu et al., 2024a). Briefly, 3.0 mL dichloromethane containing 8.8 mM decane as an internal standard was used to extract the organic products. Solutions were alkalified by adding 50 µL of 4.0 M NaOH and vortexed to ensure complete extraction of the amines. Subsequent centrifugation of the samples at 3000 RPM for 3 mins allowed the separation between the aqueous and organic layers. Phenylalanine was analyzed using high-performance liquid chromatography (HPLC, PerkinElmer 200) with a UV-Vis detector, and organic aromatic products were identified and quantified via GC-FID (Agilent 7820A equipped with a poly-capillary column and a flame-ionization detector) and GC-MS (Agilent 7890A/5975C). Dissolved gases and small carboxylic acids are likely to be formed but were not quantified due to low volumes of samples and analytical limitations. However, these small organics were not considered the primary degradation products of phenylalanine because of the absence of an aromatic

structure or the benzene ring, which is known to be relatively inert under similar hydrothermal conditions (Glein et al., 2020; Yang et al., 2012).

In the pH-dependence experiments, a similar protocol was followed, except HCl or NaOH was used to adjust the pH of the phenylalanine solution to mimic different environmental conditions. The pH was measured at room temperature and calculated *in-situ* using geochemical modeling software EQ3/6 (Table B1). The reported pHs in this study are all *in-situ* pHs. Geochemical calculations of *in-situ* pH and the model amine reactions (e.g., elimination deamination and substitution deamination) were performed using the revised Helgeson-Kirkham-Flowers equations of state (Shock & Helgeson, 1988) and thermodynamic data within the software package SUPCRT92 (Johnson et al., 1992) (accessed through the WORM portal). Model amines (C3-C6) were chosen as representative amines because of their availability in the database and relatively simple structures. The equilibrium constants for the elimination and substitution pathways for amines were calculated along the water-vapor saturation curve. Geochemical modeling of the aqueous speciation of salt solutions was also conducted using EQ3/6 to evaluate the dominant inorganic ions and complexes under hydrothermal conditions.

3.3 Results

3.3.1. Product Distribution and Degradation Pathways of Amino Acids

The product distribution of phenylalanine under the studied hydrothermal conditions (275^{o}C and P_{sat} ~59.5 bar) is shown in Figure 8. As the major product of decarboxylation, 2-phenylethylamine accumulated rapidly in early hours and then deaminated to secondary products styrene and phenylethanols (1-phenylethanol and 2-phenylethanol). Styrene was formed in much higher concentrations than phenylethanols,

accounting for >80% (in mole%) of total aromatic products after 24 hrs, whereas phenylethanols accounted for only ~15% (note that 2-phenylethanol was produced in much smaller quantities than 1-phenylethanol).

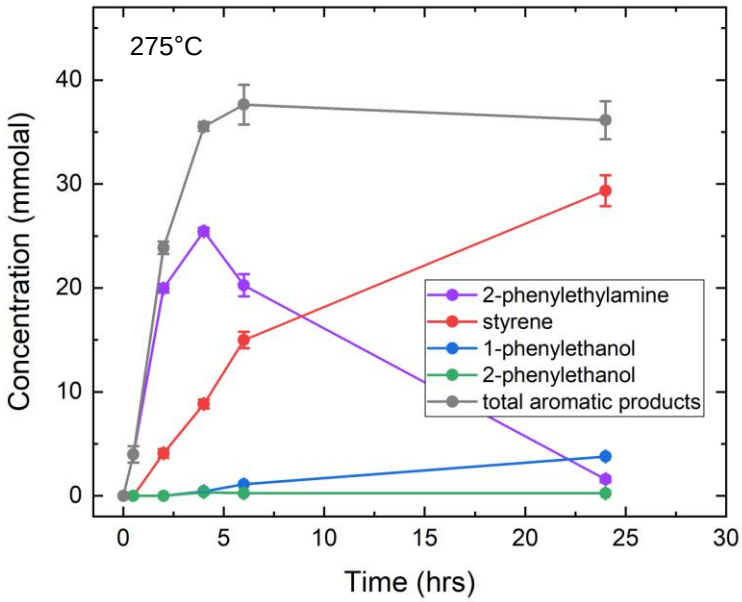

Figure 8. Product distribution of phenylalanine hydrothermal reactions in deionized water (DI) at 275°C and P_{sat} for up to 24 hrs. Total aromatic products refer to the sum of identified aromatic degradation products obtained via GC-FID (Taken from Aspin et al., submitted).

Based on the product distribution observed, the major reaction pathways for phenylalanine under the experimental conditions were proposed. As shown in Figure 9, phenylalanine can first decarboxylate to form 2-phenylethylamine, which can subsequently undergo deamination either via elimination to form styrene or via substitution to form phenylethanols. Hydration and dehydration can occur between styrene and phenylethanols under the hydrothermal conditions. Detailed discussion on the proposed pathways can be found in Section 3.4.1 and 3.4.2.

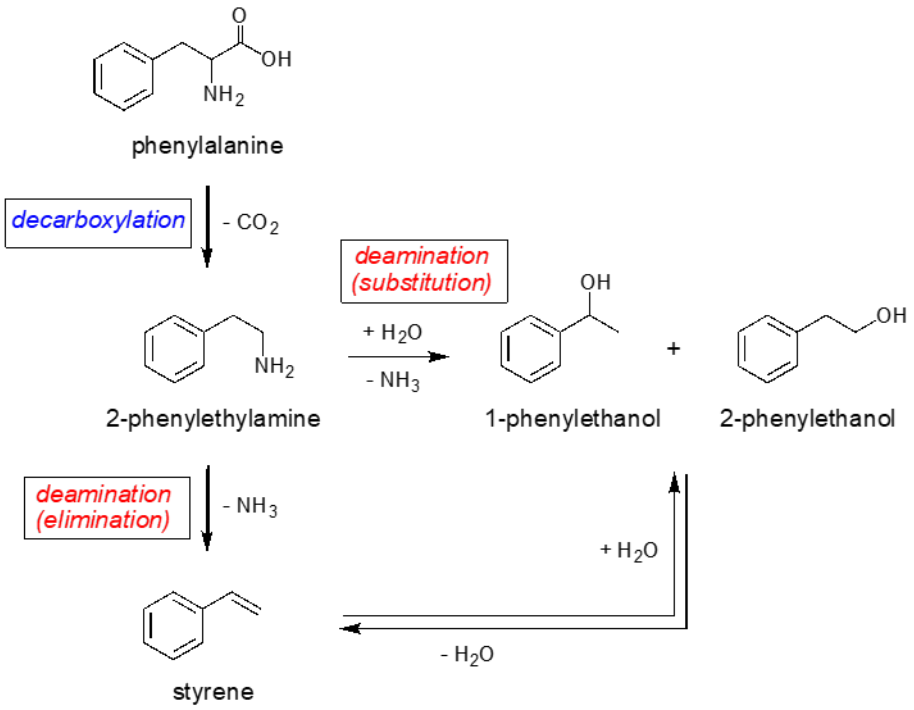

Figure 9. Proposed degradation pathways for phenylalanine under hydrothermal conditions at 275°C and P_{sat} (Taken from Aspin et al., submitted).

3.3.2. Effect of Temperature on Amino Acid Degradation

The kinetics of phenylalanine hydrothermal degradation were examined at three reaction temperatures (225°C, 250°C, and 275°C). Assuming a pseudo first-order reaction, the degradation kinetics of phenylalanine can be expressed by the following equation,

$$-\frac{\mathrm{d}m_{phenylalanine}}{\mathrm{d}t} = k_{phenylalanine} \times m_{phenylalanine} \quad (3)$$

where $m_{phenylalanine}$ represents the molality of phenylalanine, $k_{phenylalanine}$ represents the rate constant, and t represents the reaction time. As shown in Figure 10, the degradation rate constant of phenylalanine increased with increasing temperature, from 0.13 h^{-1} at 225°C, to 0.29 h^{-1} at 250°C, and 0.42 h^{-1} at 275°C, nearly doubling with each 25°C increment.

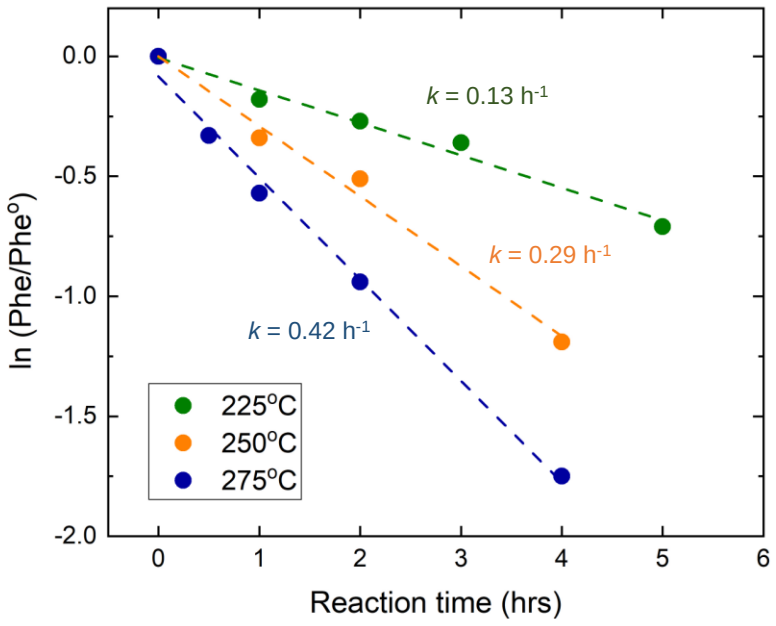

Figure 10. Pseudo first-order kinetics of phenylalanine degradation under hydrothermal conditions of 225°C, 250°C, and 275°C with a starting concentration of 0.07 molal (Taken from Aspin et al., submitted).

The reaction rate constants can also be used to calculate the half-lives ($t_{1/2}$) by the following equation,

$$t_{\frac{1}{2}} = \frac{\ln(2)}{k} \quad (4)$$

in which the half-lives were calculated to be 5.3 hr, 2.4 hr, and 1.6 hr at 225°C, 250°C, and 275°C, respectively (Table B2).

The temperature effect on deamination reactions was also examined under hydrothermal conditions. Experiments starting with 2-phenylethylamine (0.07 molal), the primary degradation product of phenylalanine, showed that its conversion increased from 3.7±1.3% at 175°C after 24 hrs to 40.6±0.9% at 275°C after 6 hrs (Table B3). The major degradation products of 2-phenylethylamine were styrene and 2-phenylethanol, although very little amount of 1-phenylethanol was also observed (<0.1 mmolal). The formation of

styrene and phenylethanols from 2-phenylethylamine further supports the proposed pathways for phenylalanine (Figure 9). With increasing temperature, styrene was formed in much greater amounts than phenylethanols, suggesting elimination deamination becomes more dominant over substitution deamination at higher reaction temperatures. At 275^{o}C, the styrene/phenylethanols concentration ratio was ~64.2 after 6 hrs, while it was only ~0.7 at 175^{o}C after 24 hrs. In addition, geochemical modeling of deamination reactions using simple amines such as propanamine, butanamine, and heptanamine also predicted that elimination deamination can become more favorable than substitution deamination in aqueous solutions at temperatures above 200^{o}C (Figure 11), which is consistent with the experimental observations.

3.3.3 Effect of pH on Amino Acid Degradation

A pH-dependence of phenylalanine degradation was observed under the hydrothermal conditions (Figure 12). The conversion of phenylalanine to total aromatic products at 275^{o}C after 6 hrs was 35-38% between pH 2.7 and 5.4, while it decreased to 15-16% at pH 1.3 and 8.5. The product distributions of phenylalanine were also found to be pH-dependent (Figure 12a). At pH 1.3, the major product was 2-phenylethylamine with no styrene being formed, while between pH 2.7-8.5 both styrene and 2-phenylethylamine were formed in comparable amounts. Benzylamine was only observed at pH 8.5 but did not form in appreciable amounts at the lower pH conditions. Figure 12b shows the ratio of styrene/2-phenylethylamine as an indicator for deamination/decarboxylation, which demonstrates favorable decarboxylation at lower pH but favorable deamination at higher pH. Over the pH range of 2.7-5.4, both the product distribution and deamination/decarboxylation ratios remained relatively stable, with the

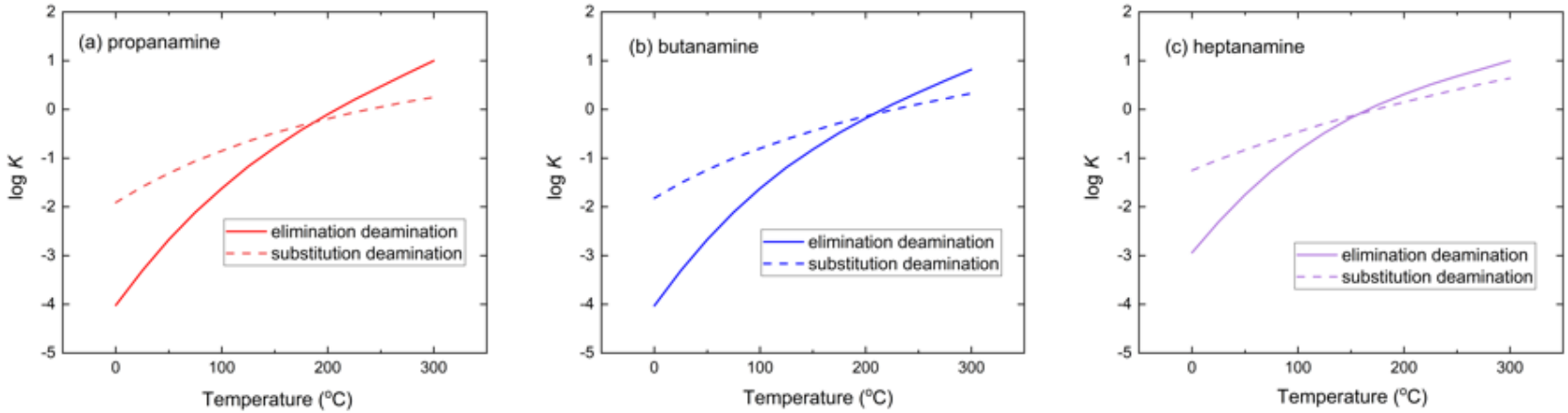

Figure 11. Calculated equilibrium constants (log K) for elimination deamination and substitution deamination using propanamine (a), butanamine (b), and heptanamine (c) as model amines as a function of temperature. Geochemical calculations were performed using the revised Helgeson-Kirkham-Flowers equations of state (Shock & Helgeson, 1988) and thermodynamic data in SUPCRT92 (Johnson et al., 1992) (Taken from Aspin et al., submitted).

major products consisting of 2-phenylethylamine and styrene, and deamination/decarboxylation ratios between 0.7 and 0.9. In addition, the kinetics of phenylalanine degradation between pH 5.4 and pH 6.4 were also studied, in which a 28% decrease in rate constant was observed from pH 5.4 to 6.4 (Figure B1).

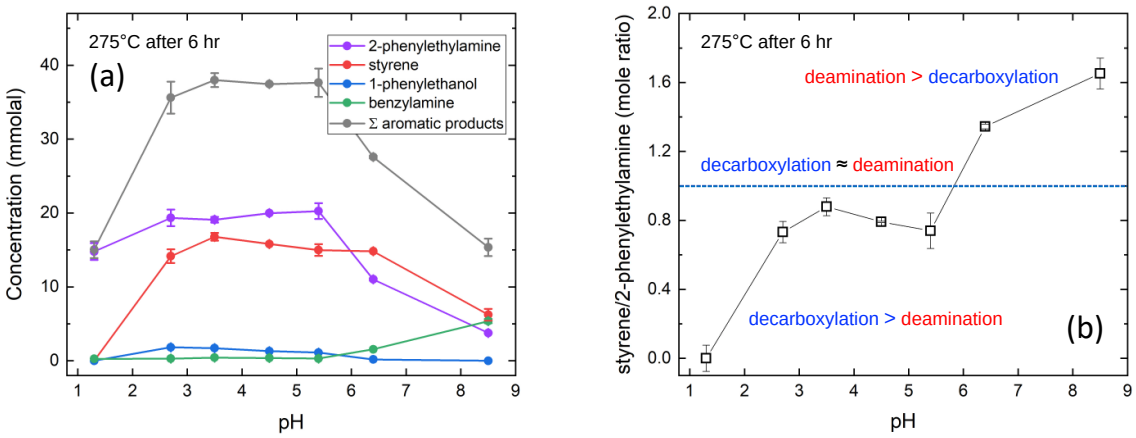

Figure 12. Product distribution (a) and relative ratios of deamination/decarboxylation pathway (b) for phenylalanine hydrothermal reactions at 275°C after 6 hrs as a function of calculated *in-situ* pH. Total aromatic products refer to the sum of identified aromatic degradation products obtained via GC-FID. Deamination/decarboxylation ratios were plotted using the concentration ratio between styrene and 2-phenylethylamine (Taken from Aspin et al., submitted).

3.3.4. Influence of Inorganic Salts on Amino Acid Survivability

Although previous studies have extensively investigated the reactivity and pathways of amino acids under hydrothermal conditions, the effects of inorganic materials such as dissolved metal salts on amino acid decomposition were much less explored. In oceanic hydrothermal systems, dissolved metal species may significantly influence organic matter transformations, such as through redox processes, complexation, and acting as Lewis acid/base catalysts. To investigate how metal salts may influence amino acid stability and pathways, a group of common inorganic salts was chosen to study in the phenylalanine experiments (Figure 13).

In general, an inhibitory effect was observed for most metal salts on phenylalanine, which decreased the formation of total aromatic products from 36% to 14-35% at 275°C after 6 hrs, aside from $FeCl_2$ and NaCl (0.1 molal) which slightly increased to 39-42% (Table B4). Not only did the salts lower the amino acid reactivity, but they also changed the product distribution significantly. As shown in Figure 13a, the relative abundance of 2-phenylethylamine (mole%) was much higher in the presence of metal salts (0.05 molal) than that in DI, but the metal salts strongly inhibited the formation of styrene. Using the ratio of styrene/2-phenylethylamine as an indicator for deamination/decarboxylation, it clearly showed that the deamination was greatly reduced in the presence of metal salts (Figure B2). Experiments starting with 2-phenylethylamine further confirmed this inhibitory effect, in which much less styrene was produced in the $AlCl_3$, $CuCl_2$, and $FeCl_3$ solutions (0.05 molal) than in DI (Figure 13b). The presence of

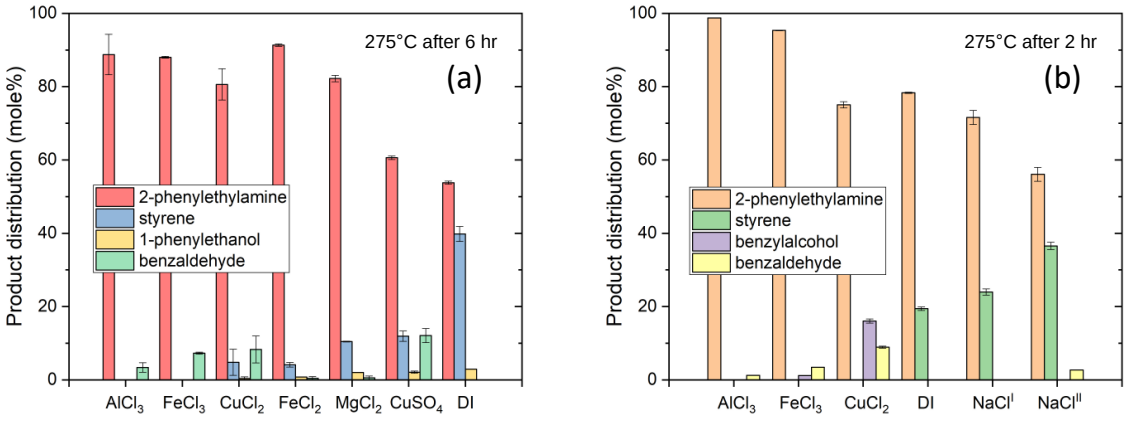

Figure 13. The relative product abundances in the phenylalanine (0.07 molal) hydrothermal experiments with metal salts (0.05 molal) at 275°C after 6 hrs (a), and in the 2-phenylethylamine (0.07 molal) hydrothermal experiments with metal salts (0.05 molal) at 275°C after 2 hrs (b). The $NaCl^I$ and $NaCl^{II}$ concentrations in the 2-phenylethylamine experiments (b) were 0.1 and 0.2 molal, respectively. The metal salts were positioned with an increasing pH from left to right on the x-axis in both (a) and (b) (Taken from Aspin et al., submitted).

metal salts could change the solution pH under hydrothermal conditions. The *in-situ* pHs of metal salt solutions (except for NaCl) were calculated to be 1.5-4.7, which were all below the pH of DI (5.4) under the experimental conditions (Table B4). By plotting the metal salts with an increasing pH from left to right (Figure 13), an increasing trend of styrene formation (i.e., elimination deamination of 2-phenyethylamine) can be observed, which suggests a pH-related effect of metal salts. In the presence of neutral NaCl solutions (0.1 and 0.2 molal), however, a higher mole% of styrene was observed, which could be attributed to the increased ionic strength (see below). In addition, an oxidation pathway for phenylalanine the produces benzaldehyde was also observed, mainly with the Fe(III) or Cu(II) salts (Figure 13a).

Geochemical modeling was conducted to evaluate the fluid speciation in the solutions of inorganic salts under hydrothermal conditions. Examples of the metal distributions are shown in Figure 14. The most abundant copper species in the 0.05 molal $CuCl_2$ solutions at 25°C was the Cu^{2+} ion, however, as temperature increases, the activity

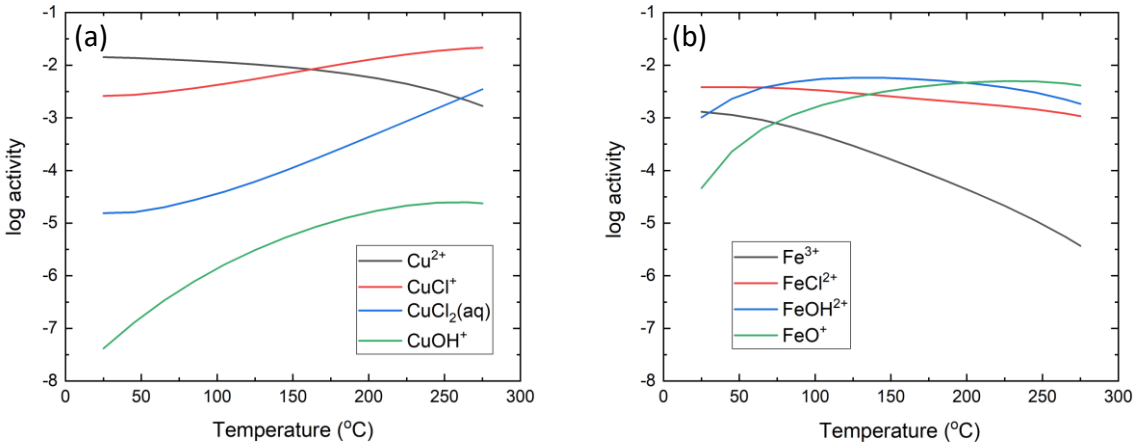

Figure 14. Calculated speciation and distribution of the major aqueous copper (a) and iron (b) species as a function of temperature and P_{sat} at equilibrium, for 0.05 molal $CuCl_2$ and $FeCl_3$ in water, respectively (Taken from Aspin et al., submitted).

of Cu^{2+} ion decreased by nearly an order of magnitude at 275°C, while other complex species such as $CuCl^{+}$ and $CuCl_{2(aq)}$ became the major copper species (Figure 14a). Similarly, geochemical calculations of 0.05 molal $FeCl_3$ in water show that the Fe^{3+} ion activity decreased significantly with increasing temperature, while $FeOH^{2+}$, FeO^{+}, and $FeCl_2^{+}$ became the dominant species at elevated temperatures. These results suggest that the complex forms of metal species rather than the uncomplexed metal ions could take part in the amino acid reactions under hydrothermal conditions.

The effect of ionic strength on phenylalanine hydrothermal degradation was also examined through hydrothermal experiments with NaCl over a range of concentrations (Figure 15). Results show that higher salt concentration and ionic strength decreased the production of total aromatic products from 39% in 0.1 molal NaCl solution to 21-29% in 0.2-1.0 molal NaCl solutions at 275°C after 6 hrs (Table B4). The relative product distributions of phenylalanine were also influenced by the ionic strength, which is

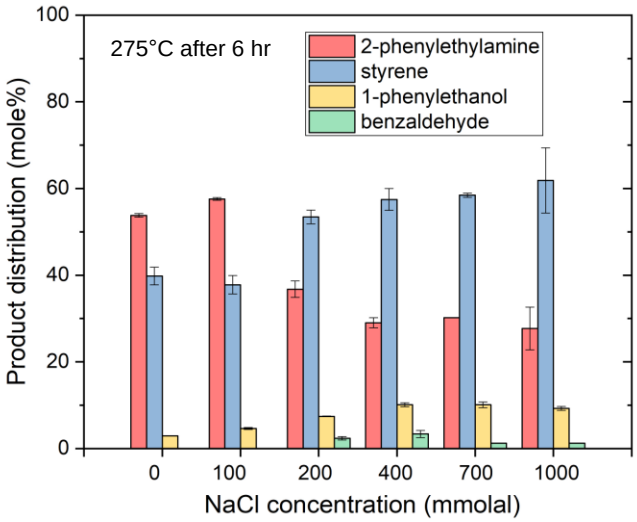

Figure 15. The relative product abundances in the phenylalanine (0.07 molal) hydrothermal reactions with NaCl at various concentrations (0.1-1.0 molal) at 275°C after 6 hrs (Taken from Aspin et al., submitted).

evidenced by the facilitated deamination pathway (e.g., styrene formation) at higher NaCl concentrations (Figure 15). Experiments of 2-phenylethylamine with NaCl showed a similar trend, which also indicates an enhancement of deamination with higher ionic strength (Figure 13b).

Fluid speciation calculations predict that increasing temperature can decrease the solution's ionic strength. For example, the 1.0 molal NaCl solution had an ionic strength of 0.940 molal in water at 25°C, while it decreased to 0.653 molal at 275°C (Table B4). Theoretical calculations of activities of Na^+, Cl^-, and NaCl(aq) in a 0.1 molal NaCl solution as a function of temperature showed that the activity of NaCl(aq) increased by a factor of 7 from 25°C to 275°C (Figure B3). These results suggest that fluid composition and ionic strength could play a role in the survivability of amino acids in oceanic hydrothermal systems.

3.4. Discussion

3.4.1. Decarboxylation of Amino Acids

Decarboxylation of phenylalanine in high-temperature aqueous environments has been previously studied. For example, Vallentyne reported 2-phenylethylamine as a primary decarboxylation product of phenylalanine at temperatures between 216°C and 280°C (Vallentyne, 1964); Sato et al. observed a rapid first-order decomposition of phenylalanine in water at 300°C and 20 MPa where ammonia, acetic acid, and formic acid were formed as the main products (Sato et al., 2004); Abdelmoez et al. reported that decarboxylation and deamination were the major pathways for phenylalanine in subcritical water (Abdelmoez et al., 2010); and Changi et al. examined the degradation kinetics and product distribution of phenylalanine at 220-350°C (Changi et al., 2012).

The decarboxylation rates of phenylalanine under similar hydrothermal conditions are summarized and compared in Table B2. In this study, the rate constant of phenylalanine increased from 0.13 h^{-1} at 225°C to 0.29 h^{-1} at 250°C, which is comparable to the previously reported rates of 0.17 h^{-1} at 230°C (Abdelmoez et al., 2010) and 0.50-0.57 h^{-1} at 250°C (Abdelmoez et al., 2010; Changi et al., 2012; Li & Brill, 2003). At higher temperatures, however, less similarities in rate constants are observed. In the present study, the rate constant at 275°C was 0.42 h^{-1}, while a relatively wide range of rate constant (0.96-4.20 h^{-1}) at 260-290°C has been reported by other studies (Table B2). The differences in decarboxylation rates could be attributed to variations in experimental conditions and analytical procedures among the studies. It should also be noted that the degradation products of phenylalanine have been found to be different – some studies reported 2-phenylethylanine, styrene, and oligomers as the major products (Abdelmoez et al., 2010; Changi et al., 2012; Vallentyne, 1964), while others reported small carboxylic acids such as formic and acetic acids were mainly formed (Sato et al., 2004).

The solution pH plays an important role in hydrothermal degradation of phenylalanine. A larger extent of degradation is observed at mid-pH range (2.7-5.4), whereas decreased activity of phenylalanine is observed in very acidic or basic solutions (Figure 12a). The pH dependence suggests that phenylalanine reactivity could be influenced by the overall charge of the molecule. The pKa values of the amino and carboxyl groups in phenylalanine are 9.13 and 1.83 at room temperature, respectively (Lide, 1991), but they are expected to change at higher temperatures. Robinson et al. calculated the pKa of aminiums as a function of temperature, predicting that a protonated amine with a pKa between 8.5-10.5 at room temperature could have a pKa of 5.0-5.8 at

275°C (Robinson et al., 2019). In a study on the decarboxylation of phenylacetic acids, Glein et al. modeled the change in pKa of carboxylic acids over a range of temperatures, predicting the pKa of benzoic acid could increase from 4.25 at 25°C to roughly 5.25 at 275°C (Glein et al., 2020). Although the pKas of phenylalanine under hydrothermal conditions are unknown, it would be reasonable to expect the pKas of the amino and carboxyl groups to be more near neutral at elevated temperatures than at room temperature.

When the solution pH is lower than $pKa_{(carboxyl)}$, phenylalanine will be in a cationic form, while at pH higher than $pKa_{(amino)}$, the amino acid will change into its anionic form (Figure 16). Our experimental results suggest that the degradation of phenylalanine is inhibited in its ionic forms, which is also in alignment with another study of glycine that showed the ionic forms of glycine decarboxylated 10 times slower than the zwitterion form in a potassium phosphate buffer solution at 170-260°C (Snider & Wolfenden, 2000). Although the reaction conditions may differ, they also showed that glycine reactivity remained relatively stable over the mid-pH range of 5.8-7.8 (measured

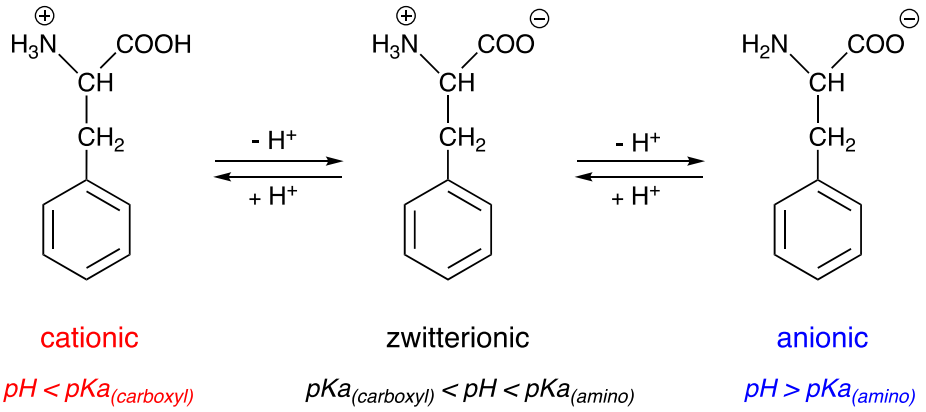

Figure 16. The cationic, zwitterionic, and anionic forms of phenylalanine as affected by the solution pH. The $pKa_{(carboxyl)}$ and $pKa_{(amino)}$ of phenylalanine at room temperature are 1.83 and 9.13, respectively (Taken from Aspin et al., submitted).

at room temperature). A study on alanine decarboxylation at 280-330^{o}C also showed that the decarboxylation rate was three times faster in the zwitterionic form than in the cationic or anionic form (Li et al., 2002). Another study on glutamic acid stability under different pH conditions also reported a decrease in amino acid decomposition in more alkaline solutions (e.g., at pH 10) (Lee et al., 2014a). The consistency between the previous studies and this work suggests that the formation of a zwitterion plays a key role in promoting amino acid decarboxylation, where the *in-situ* pH is between the pKas of the amino acid under hydrothermal conditions (Table B1).

Density functional theory (DFT) suggests that the zwitterion is more stable in water than the neutral form and that water molecules could stabilize the zwitterionic amino acid through hydrogen bonding with the carboxylate and aminium groups (Li & Brill, 2003; Rodziewicz & Doltsinis, 2007). In the transition state, the hydrogen in the water molecule could be "swinging" from the carboxyl group to the α-carbon (Li & Brill, 2003) (Figure B4). When the carboxyl group is released as CO_2, a carbanion intermediate will be formed and hydrogen-bonded to water, which is highly unstable in solution. The water molecule then facilitates the transfer of a proton from the amine group to the carbanion, resulting in the release of an amine and the regeneration of the water molecule. Increased hydration of the system could also increase the stability of the zwitterion in solution and thus allow for more possible orientations of hydrogen bonding with the amino acid. In general, water molecules between the amine and carboxyl groups allow the stabilization of zwitterionic amino acids and thus potentially facilitate the decarboxylation mechanism (Rodziewicz & Doltsinis, 2007). Additionally, the presence of an aromatic ring at the β-carbon can act as an electron sink that helps dissipate the

negative charge forming at the α-carbanion (Li & Brill, 2003), as is the case for phenylalanine. Although these theoretical predictions may not exactly reflect the experimental conditions in this study, they may help explain the role of water in stabilizing the zwitterionic form of amino acids and how decarboxylation could be promoted. Other experimental studies also seem to support the proposed mechanism, which involves a carbanion intermediate for amino acid decarboxylation in aqueous systems (Bada & Miller, 1970; Körner, 2021).

3.4.2. Deamination of Amino Acids

Following the decarboxylation of phenylalanine, there is an increase in the production of styrene and phenylethanols over the reaction time studied (Figure 8). Since styrene is generated at earlier reaction times than phenylethanols, it suggests that styrene could be a primary product of 2-phenylethylamine. However, phenylethanols could also be formed directly from 2-phenylethylamine through substitution deamination, as suggested by previous studies showing benzylalcohol as a primary product of benzylamine under hydrothermal deamination (Robinson et al., 2019; Robinson et al., 2021b). Furthermore, it is also likely that styrene and phenylethanols can interconvert through (de)hydration, as reported by other hydrothermal studies (Aspin et al., 2023; Changi et al., 2012; Liao et al., 2021).

Thus, there are two competing deamination pathways for 2-phenylethylamine under hydrothermal conditions, i.e., elimination deamination to form styrene and substitution deamination to form phenylethanols (Figure 9). Substitution reactions typically proceed either via a unimolecular nucleophilic substitution (S_N1) or a bimolecular nucleophilic substitution (S_N2) mechanism. Previous studies on the

deamination substitution of amines suggest that both S_N1 and S_N2 mechanisms may occur (Robinson et al., 2019; Robinson et al., 2021b). An S_N1 deamination typically involves the formation of a primary carbocation intermediate, which can undergo rearrangement to form a secondary carbocation with higher stability. An S_N2 deamination, however, is a concerted process with no carbocation intermediate formed. Thus, evidence for the S_N1 deamination in this study would include the generation of both secondary (1-phenylethanol) and primary (2-phenylethanol) alcohols from 2-phenylethylamine, while the S_N2 deamination would only produce the primary alcohol. Since 1-phenylethanol is observed in higher quantities than 2-phenylethanol at 275^{o}C (Figure 8), an S_N1 deamination mechanism is likely to occur in the phenylalanine experiments.

However, the S_N2 deamination cannot be entirely ruled out, because both mechanisms could be present concurrently, as suggested by others (Cox & Seward, 2007; Robinson et al., 2019). The S_N1 pathway is more entropically favored than the bimolecular S_N2 pathway, suggesting that S_N2 could be preferred at lower temperatures. This may also help explain the preference for 1-phenylethanol over 2-phenylethanol via S_N1 and S_N2 mechanisms at 275^{o}C, while lower temperature experiments of 2-phenylethylamine show exclusive deamination to 2-phenylethanol with no formation of the secondary alcohol, even after 120 hrs (Table B3). These results suggest that the S_N2 deamination does occur and may become more favorable at lower temperatures.

Compared to the substitution deamination pathway, elimination deamination is observed to be far more favorable under the experimental conditions (275^{o}C). Over the studied pH range, elimination deamination dominates over substitution, which is evidenced by the ratio of styrene to phenylethanol being greater than 1 (Figure B5). With

increasing pH, the ratio also increases, suggesting a based-catalyzed pathway for elimination deamination. Additionally, reaction temperature also seems to play a role in the preference for elimination or substitution deamination. At higher temperatures (275^{o}C), elimination tends to dominate over substitution, while substitution is found to be more competitive at lower temperatures (e.g., styrene/phenylethane ratio ~0.80 175^{o}C after 24 hrs). A previous study showed a similar trend, with phenylethanol being produced in higher quantities than styrene at lower temperatures (220-250^{o}C), yet up to 10 times as much styrene than phenylethanol was observed at a higher temperature (350^{o}C) (Changi et al., 2012). These experimental observations are further supported by geochemical modeling of the equilibrium constants for both deamination reactions, which shows that elimination can become more thermodynamically favorable than substitution at higher temperatures (Figure 11). Since elimination reactions increase entropy (one molecule forming two molecules) and substitution reactions do not (two molecules forming two molecules), higher temperatures would likely enhance the entropic contribution to the system free energy change, making elimination reactions more thermodynamically favorable (Yang & Aspin, 2023).

3.4.3. Interactions Between Amino Acids and Metal Salts

Natural hydrothermal systems vary in salt content, mineralogy, and redox potential, which could all influence organic hydrothermal transformations. The hydrothermal experiments in this study were not redox buffered, however, the redox state constrained by inorganics such as mineral assemblages in natural hydrothermal systems is expected to play an important role in controlling amino acid reactivities. Studies that focused on the effect of dissolved H_2 on glutamic acid stability conclude that with high

enough concentrations of H_2, the stability of amino acids may be enhanced and that the irreversible decarboxylation could be inhibited (Lee et al., 2014a; Lee et al., 2014b).

In the present study, most of the dissolved salts show an inhibitory effect on the decarboxylation of phenylalanine. Similar observations are also reported such as the enhanced recovery of amino acids (L-proline, L-serine, L-alanine, and glycine) in the presence of dissolved metals (Chandru et al., 2013), and the inhibited decarboxylation of amino acids with electrolyte KCl and NaCl (Changi et al., 2012; Li et al., 2002). Although the effects of metal salts could be mainly attributed to the change of chemical properties of hydrothermal fluids, such as solution pH and ionic strength, which have both been shown in this study to affect the reactivity of phenylalanine, the specific metal ions and complexes may have additional contributions. For example, phenylalanine experiments containing 0.05 molal $FeCl_3$ or $AlCl_3$ have similar pHs at 275^{o}C (1.6 and 1.5, respectively), yet the concentrations of the formed aromatic products in the $FeCl_3$ solutions are twice as much as with $AlCl_3$ (Table B4). Solutions containing 0.05 molal $CuCl_2$ or $FeCl_2$ have similar ionic strengths at 275^{o}C (69 and 87 mmolal, respectively), yet much fewer decarboxylation products are formed with $CuCl_2$ than with $FeCl_2$. These results suggest that the metal species and complexation they form under hydrothermal conditions may play an important role in the amino acid reactions.

Geochemical calculations show that in solutions with chloride ions, complexes between the metal ion and Cl^- (e.g., $CuCl^+$, $FeCl^+$, and $FeCl_{2(aq)}$) become one of the major species at higher temperatures, while the free metal ions are less prevalent (Figure 14). Previous studies have suggested that anionic speciation could strongly affect the hydrogen-bonding environments in water (Foustoukos, 2016). Anions such as Cl^- are

considered “structure breakers”, which form weaker bonds with water than water bonds themselves, promoting the coupling between water molecules (Ahmed et al., 2014). In contrast, other anions with large charge densities such as SO_4^{2-} are considered “structure makers”, which may cause electrostatic ordering by forming strong hydrogen bonds with water, thereby disrupting the inter-water hydrogen bonding (Hu et al., 2022; Waluyo et al., 2011). The fact that the phenylalanine experiment with $CuSO_4$ produced the lowest amount of degradation products among all the studied metal salts (Table B4), seems to support this hypothesis.

The influence of ions on water structure and hydrogen bonding may also help explain the results of the ionic strength experiments (Figure 15), as the stability of the hydrogen-bonded water network is proportional to the solution’s electrolyte concentrations (Foustoukos, 2016; Kanno et al., 2006). Increasing ionic strength has also been shown to have a negative impact on the activity of water (Aranovich & Newton, 1996), which may inhibit the decarboxylation of phenylalanine, considering water molecules can potentially promote the transfer of protons through the decarboxylation mechanism (Figure B4).

Although the interaction mechanisms between amino acids and metal salts under hydrothermal conditions have not been fully uncovered, previous theoretical DFT simulations predicted that the addition of metal salts could form complexes with the carboxyl group of zwitterionic amino acids (Ganesan et al., 2013; Liu et al., 2022; Remko et al., 2011). A recent theoretical study also showed that metal ions tend to be more strongly adsorbed to amino acids containing more carboxyl groups (e.g., aspartic and glutamic acids) (Liu et al., 2022). It is likely that the metal ions stabilize the zwitterionic

amino acids and lower their activity, thereby preventing their degradation. Furthermore, the metal ions could also be stabilized by solvation with water molecules, which may cause higher steric hindrances and possibly weaken the hydrogen bonding with the α-carbon and amine group which is potentially responsible for the decarboxylation mechanism (Ganesan et al., 2013). More theoretical and experimental studies on metal speciation and organic-inorganic interactions under hydrothermal conditions would be needed to fully elucidate the salt influence on amino acid reactivity and survivability in salty hydrothermal systems.

3.4.4. Implications for Amino Acid Survivability in Ocean Worlds

Geochemical properties vary among the hydrothermal vents at the seafloor of Earth, and likely, in other ocean worlds such as Saturn's moon Enceladus. Vent systems differ in temperature, pH, salt content, mineralogy, and redox potential, which could all influence organic hydrothermal transformations in the ocean worlds. Identifying the specific geochemical constraints is therefore important for understanding the chemistry and fate of organic molecules including biosignatures in those environments. This study specifically focuses on the survivability of amino acids, which shows the zwitterionic form tends to degrade faster than the cationic or anionic form, being consistent with other studies (Abdelmoez et al., 2007; Lee et al., 2014b; Li et al., 2002). This pH-dependence implies that amino acid survivability could be slightly higher in very acidic or alkaline hydrothermal vents, such as Rainbow with vent pH below 3 (Seyfried et al., 2011) and Lost City with highly alkaline vent fluids (Lang & Brazelton, 2020). In icy ocean worlds such as Enceladus, the pH of the ocean is inferred to be 8 – 10 (Glein & Waite, 2020), which may also help to preserve amino acids to some extent in the expected

hydrothermally active ocean. The preservation of biomolecules in icy ocean worlds would allow for the detection of biosignatures prior to degradation, which is one of the primary goals for future search-for-life missions (Neveu et al., 2024a; Neveu et al., 2018). However, it should also be pointed out that the lifetimes for amino acid degradation at relevant hydrothermal temperatures are relatively short. Truong et al. have proposed that any primordial amino acids at Enceladus could have already been destroyed, and the preservation of amino acids, if detected on Enceladus, should have been recently formed (Truong et al., 2019).

Furthermore, while many studies have been focusing on hydrothermal reactions of organic molecules in pure water, natural oceanic hydrothermal systems are enriched in a complex array of inorganic materials. Solid minerals or dissolved metal salts will inevitably come into contact with the organic compounds in these environments and influence their reaction pathways. Here, this study reveals that the presence of common metal salts or relatively high ionic strength could play a protective role in amino acid breakdown, thereby enhancing their survivability under hydrothermal conditions. In Earth's hydrothermal vents, the concentration of dissolved metals in high-volume fluids can reach up to micromolar or millimolar (Cohen et al., 2021; Lough et al., 2019; Sander & Koschinsky, 2011), while concentrations of dissolved free amino acids could be several orders of magnitude lower such as in the nanomolar or picomolar range (Fuchida et al., 2014; Longnecker et al., 2018). In Enceladus' ocean, amino acids are expected to be in the nanomolar-micromolar range (MacKenzie et al., 2022; Steel et al., 2017), while the salt concentration is inferred to be 0.5-2% (sodium and potassium salts by mass) (Postberg et al., 2011). It is thus likely that the inorganic:organic ratios in natural

hydrothermal systems could be substantially higher than those in the present study, implying a stronger protection from the metal salts may occur.

In addition, although the present study uncovered some interesting effects of individual metal salts on phenylalanine reactivity, it cannot simply represent complex oceanic hydrothermal systems, which contain a mixture of dissolved salts and minerals with varying fluid composition, pH, and redox state. Further work of using natural or simulated seawater would be necessary to elucidate the overall and real impact of inorganics on amino acid transformations in natural hydrothermal fluids. Rainbow vent fluids that contain high concentrations of dissolved H_2 (Charlou et al., 2002; Holm & Charlou, 2001), enriched chloride relative to seawater (Douville et al., 2002; Holm & Charlou, 2001), and high amounts of transition metals such as dissolved iron (Allen & Seyfried, 2003; Schmidt et al., 2007), would be a good example to study. Moreover, this study sought to investigate phenylalanine alone, which is in contrast to natural environments that usually contain a suite of amino acids. Vallentyne reported that glycine, alanine, and phenylalanine decomposed more rapidly in mixtures than alone (Vallentyne, 1964), while Abdelmoez et al. also showed a 2- to 3-fold increase in decomposition rate of amino acid mixture (e.g., leucine, isoleucine, phenylalanine, and histidine) compared to that of single amino acids in subcritical water (Abdelmoez et al., 2007). These studies further suggest that the reactivity and survivability of amino acids may become more complex in natural systems, in which a wide variety of inorganic and organic matter may interplay and contribute to the decomposition or stabilization of amino acids in hydrothermal fluids.

3.5. Conclusions

This work investigates the reactivity and transformation pathways of phenylalanine under geologically relevant hydrothermal conditions. A general amino acid degradation pathway that involves decarboxylation, followed by deamination via two competing mechanisms (i.e., substitution vs. elimination), has been identified. The reactivity of amino acids is strongly pH-dependent, with the zwitterionic form exhibiting the highest reactivity, while the cationic and anionic forms both decrease the reactivity in very acidic or alkaline solutions. Furthermore, dissolved metal salts may affect both the degradation and product distribution of amino acids, and the stability of amino acids could be enhanced in the presence of inorganic salts or relatively high ionic strength in hydrothermal solutions. Overall, these results suggest that dissolved inorganic composition and fluid chemistry play important roles in amino acid hydrothermal reactivity and pathways, which may provide new insights into understanding the fate and survivability of amino acids in oceanic hydrothermal systems on and outside Earth.

CHAPTER FOUR

EFFECT OF THE LIQUID-VACUUM TRANSITION ON THE RELATIVE ABUNDANCES OF AMINO AND FATTY ACIDS SOUGHT AS BIOSIGNATURES ON ICY OCEAN WORLDS

4.1 Introduction

In our Solar System, several icy moons and dwarf planets harbor subsurface oceans (Hendrix et al., 2019). A few of these ocean worlds display surface or plume activity indicating that subsurface liquid material is being expressed at or above the surface. These include Enceladus (Porco et al., 2006; Villanueva et al., 2023b), Ceres (Ruesch et al., 2016), and, perhaps, Europa (e.g., (Quick et al., 2017; Roth et al., 2014; Villanueva et al., 2023a), and references therein). The detection or expectation of sources of bioavailable energy and bioessential elements from the interiors of Enceladus and Europa, respectively (Hand et al., 2009; Hsu et al., 2015; Khawaja et al., 2019; Postberg et al., 2023; Postberg et al., 2018b; Vance et al., 2023; Villanueva et al., 2023a; Waite et al., 2017), makes them prime places to search for life without having to access the (sub)surface (Cable et al., 2021; Dotson, 2020; Hand et al., 2022; MacKenzie et al., 2022).

Any search for signs of life and contextual information in erupted materials requires inferring, from the measurements, characteristics of their subsurface liquid source and mechanisms for release to the surface and subsequent processing (e.g., radiation exposure at the surface or in orbit) before collection. The nonvolatile solute composition may be preserved through eruption, e.g., if the liquid source composition is frozen in due to rapid cooling (Thomas et al., 2019; Vu et al., 2020; Vu et al., 2023),

albeit (1) with bulk concentration or dilution due to loss of water to vaporization or condensation of water sublimated from a solid source (Khawaja et al., 2019; Postberg et al., 2018a), and (2) at spatial scales larger than individual ice grains (Fox-Powell & Cousins, 2021).

Erupted material could also undergo broader compositional changes. In the plume of Enceladus, water vapor (90–99 mass% of the plume at ~100 km altitude; (Postberg et al., 2018a) dominates over ice. Plume ice grains falling back to the surface may not, alone, explain this high vapor enrichment compared to the ≈1:7.5 vapor:ice proportions expected from exposing liquid water at the triple point to vacuum (Spencer et al., 2018). This suggests a role for additional processes, such as accretion of grains on conduit walls or ice sublimation from these walls, which might distill or cycle nonvolatile material between the subsurface liquid and the surface vent. Along the way, moderately volatile organic compounds might be selectively adsorbed onto ice (Bouquet et al., 2019; Khawaja et al., 2019). The plume also contains percent-level gasses other than water: e.g., CO_2, CH_4, N_2 or CO, H_2, NH_3, and HCN (Peter et al., 2023; Waite et al., 2017). These volatile compounds are likely exsolved from the fluid, which can alter such fundamental chemical properties of erupted material as its pH (e.g., via CO_2–carbonate equilibria), affecting the molecular form of most chemical elements in water (Fifer et al., 2022). These processes may alter material properties that search-for-life missions seek to measure.

The overall process certain to occur during eruption on airless ocean worlds is the phase transition of water from the liquid phase to vapor and ice in vacuum (hereafter "liquid-vacuum transition"). At Enceladus, this transition occurs in subsurface plume

source conduits (Ingersoll & Nakajima, 2016; Nakajima & Ingersoll, 2016; Schmidt et al., 2008). At Ceres, it may occur as erupted material flows onto the surface (Ruesch et al., 2016; Ruesch et al., 2019; Scully et al., 2020). At Europa, both eruption styles are possible (e.g., Fagents, 2003; Roth et al., 2014).

Here we investigate whether, and to what extent, the liquid-vacuum transition can change relative abundances of amino and carboxylic (fatty) acids in erupted material targeted by search-for-life measurements (Dorn et al., 2003; Hand et al., 2022; MacKenzie et al., 2022). Amino and fatty acids that differ in their volatility, solubility, charge, or other physicochemical properties may be partitioned differently in material transported into vacuum than in its aqueous source.

We report the results of experimental injections of aqueous solutions of amino and fatty acids into a vacuum chamber, using a procedure described in Section 2. Despite significant deposition along the fluid path, we find moderate changes in relative proportions (< 50% relative to glycine) of amino acids, and less constrained but slightly larger changes in those of fatty acids, when considering material aggregated by section of the fluid path (Section 3). We discuss possible causes for these changes in Section 4. We find them small compared to differences in relative abundance patterns between example biological and abiotic sources. We conclude in Section 5 on the prospects for recognizing evidence of life based on relative abundances of amino and fatty acids in materials having undergone the liquid-vacuum transition.

4.2 Materials and Methods

4.2.1 Injection of Liquid into Vacuum

To inject aqueous solutions into vacuum, we designed and built an experimental setup at NASA's Goddard Space Flight Center (Figure 17). This setup consists of an organic-clean (no elastomer seals), bakeable vacuum chamber (Sharon Vacuum Co., Inc.) into which a solution is injected using a low-flow valve. The resulting abundant water vapor is evacuated by a turbo mechanical pump (Agilent TwisTorr 74 FS) backed by a dry scroll forepump (Agilent IDP-7), and also partly condensed on a copper plate cooled by a Stirling cryocooler (Sunpower/Ametek Cryotel MT). The condensed fraction of the vapor can be recovered post-injection for analysis. The rest of the chamber is at room temperature, as is, roughly, the injection line (see below). An aluminum collection cup of diameter ≈ 5 cm, of the type typically used as a weighing container, was placed inside the chamber, facing the port through which material was injected, on a stand of ultra-high

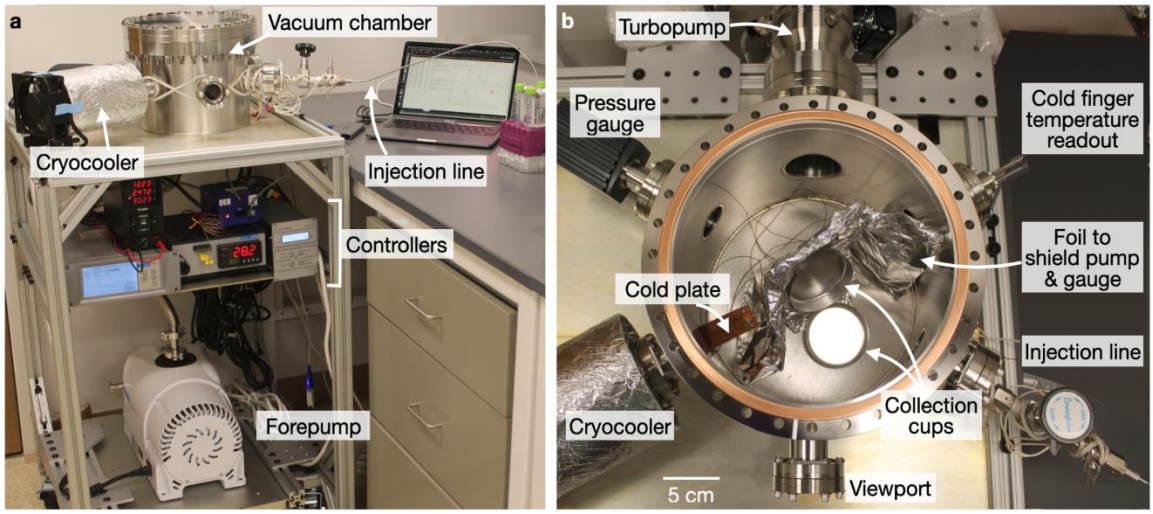

Figure 17. (a) Overview of the experimental setup with the injected solution to the right, on the purple stand. (b) Top view of the chamber with, inside, a cryocooled copper plate (to condense part of the water vapor), aluminum collection cups, and aluminum foil stand/shield (Taken from Neveu et al., 2024a).

vacuum aluminum foil (All Foils, Inc.) that also shielded the gauges and pumps from particles. A second cup was placed at the chamber bottom to collect material that had fallen from the port facing cup.

The chamber's base pressure is 5×10^{-7} Torr. Upon injection of liquid, it increases along the water vapor pressure curve at the cryocooled plate temperature. The pressure along this curve was controlled by adjusting the fluid flow rate using the low-flow valve to remain below the triple point pressure of H_2O (P_t = 611 Pascals = 4.6 Torr), ensuring the injected material underwent a complete liquid-vacuum transition. When depressurization brings the injected water to P_t, water partially boils; the corresponding enthalpy of phase change ($L_{vap} \approx 2500$ kJ kg^{-1}) would tend at thermodynamic equilibrium to freeze L_{vap} / $L_{freeze} \approx 7.5$ times as much water, since the enthalpy of 7 freezing is L_{freeze} = 334 kJ kg^{-1} (Spencer et al., 2018). Freezing in the injection line could cause ice to clog it, resulting in an ice-vacuum sublimation interface rather than the liquid-vacuum transition we sought to investigate. Although dissolved salts and supercooling could delay ice formation (e.g., Pruppacher & Klett, 2010), in pilot injections we noticed segments of the injection line becoming cold, and therefore opted to heat the injection line to 30±15ºC to prevent freezing up to, and excluding, the chamber flange (see Figure 18). Injection rates ranged from 1 to 25 mL h^{-1}. Lower flow rates resulted in impractically long injection times (weeks for a ≥ 200 mL solution). Higher flow rates resulted in vapor loads above P_t. The ratio of flow rate to conduit cross-sectional area up to the flange, (1–25 g h^{-1}) / (7.9–32 mm^2), is 0.009–0.88 kg m^{-2} s^{-1}. It is similar to the ratio obtained for one of ≈100 vents (C. Porco et al., 2014), meters in scale (Goguen et al., 2013; Ingersoll & Nakajima, 2016), that together provide a flow rate of 300 kg s^{-1} relevant to Enceladus

(Villanueva et al., 2023b): (300 kg s^{-1}) / 100 / (3–300 m^2) = 0.01–1 kg m^{-2} s^{-1}. The length:diameter ratio of section of the injection line depressurized below P_t, about (15 cm)/(3 mm) = 50, is at the low end of the ratio estimated for Enceladus conduits, ~(0.5–1 km)/(1–10 m) = 50–1000, since the neutral buoyancy level of liquid water in pure water ice would be at ≈10% of the depth of a ≈5–10 km-thick ice shell in the south polar region (Hemingway & Mittal, 2019). Other aspects of this experimental setup differ from known or expected properties of eruption conduits through Enceladus' ice shell in such a way that grain-wall interactions are not accurately emulated. First, experimental conduit walls are not made of ice, but stainless steel. Second, the experimental ratio of grain velocity to conduit length, i.e., residence time in the conduit, is three to four orders of magnitudes lower in the experimental setup (see Section C1 and below).

The injected liquid is expected to have turned to vapor and droplets of size d ranging from μm to mm resulting from burst bubbles (e.g., Cochran et al., 2016; Porco et al., 2014, and references therein) that partially vaporized. The energy loss from vaporization can freeze a droplet core of diameter d in t_{freeze} ~ 0.03 (d / 1 mm) second (Miller et al., 2022; Steddum, 1971), i.e., ~10 to 10^5 μs. Dissolved salt may delay complete freezing, but the low salt concentration in our solutions (~1 wt.%, see below) and the low energy loss needed to cool from 273 K to the water-salt eutectic temperature ($C_p \Delta T \approx$ 80 kJ kg^{-1}, i.e., ~25% of L_{freeze}, where C_p is the heat capacity of water and ΔT the temperature contrast, about 20 K for NaCl) suggest this delay is not significant. Supercooling to as low as 230 K (Pruppacher & Klett, 2010) may cause another ~25% delay. The fluid cooling rate can be roughly estimated as the difference between the room or conduit temperature and the H_2O triple point temperature (T_{triple} = 273 K), about 25 K,

divided by an inferred residence time of ~0.005 s (Section C1), i.e., ~103 K s^{-1}. Such cooling rates have been invoked for ocean droplets undergoing ejection on Enceladus (Section 4.4 of Fox-Powell & Cousins, 2021, and references therein). However, they are much higher than a bulk fluid cooling rate of $(T_{triple}–T_{vent})/t$ ~ 0.1 K s^{-1} calculated for conduit parameters relevant to Enceladus, with a fluid transport timescale of t ~ 500 s (Nakajima & Ingersoll, 2016) between the liquid at T_{triple} (v_{fluid} = 5 m s^{-1}) and the surface vent at $T_{vent} \approx$ 200 K (Goguen et al., 2013) (v_{fluid} = 150 m s^{-1}). The two classes of cooling rates result in different salt compositions and microscale spatial distributions (Fox-Powell & Cousins, 2021; Thomas et al., 2019). Such previously observed differences in spatial distribution are likely not relevant at the macroscopic scales (centimeters) considered here, which comprise all grains in a given section of the fluid path. However, we cannot exclude the possibility that the formation of different salts affects salt-organic interactions (Vu et al., 2023), and therefore, affects changes in the relative abundances of organic compounds.

We report the results of two sets of injections: one of a mixture of twelve amino acids (three injections of the same volume of the same solution), and one of a mixture of two fatty acids (two injections of different volumes of the same solution). All compounds were purchased from Sigma-Aldrich (≥98% or higher purity) and used without further purification. The amino acids listed in Table 1 were chosen to span compounds found only naturally on Earth in biological samples (e.g., histidine), only in abiotic samples (e.g., 2-aminoisobutyic acid and γ-aminobutyric acid), and in both types of samples (see Figure 18 and references in its caption). The two fatty acids were chosen as structural end-members: phenylacetic acid is a short aromatic compound, whereas palmitic acid is a

long aliphatic fatty acid commonly found in biological cellular membranes (Madigan et al., 2011). The compounds were dissolved in deionized water (DI; 18.2 MΩ•cm) containing 1 mass% NaCl (Sigma-Aldrich, ≥ 99%) and a sub-mass% amount of Na_2CO_3 to adjust the pH to around 9. These salt composition and pH are intended to approximate the salt composition and pH of Enceladus' ocean, inferred to be 0.5–2 mass% Na- and K-chloride and carbonate (Postberg et al., 2011) and pH 8–10 (Fifer et al., 2022; Glein & Waite, 2020) based on analyses of plume grains. These current best estimates are limited by the potentially biased sampling by the Cassini spacecraft of only those plume grains that could reach sufficiently high altitudes. Although ejected material has been best characterized at Enceladus, this composition is broadly relevant to the NaCl and carbon-bearing deposits observed at, and deemed endogenic to, Ceres, Europa, and Ganymede (De Sanctis et al., 2016; Tosi et al., 2024; Trumbo et al., 2022; Villanueva et al., 2023a). They do not encompass, e.g., $MgSO_4$-rich compositions that are part of possible compositions for Europa's ocean (e.g., Melwani Daswani et al., 2021).

Amino and fatty acid concentrations were on the order of mmol per kg H_2O (millimolar or mM). This is one to five orders of magnitude more concentrated than estimates for icy world subsurface oceans (e.g., (Guzman et al., 2019; Hand et al., 2016; MacKenzie et al., 2022; Steel et al., 2017)), but necessary to ensure detectable amounts of these organic compounds in compositional analyses (Sections 4.2.2 and 4.2.3). Millimolar concentrations are below saturation for all amino acids and phenylacetic acid, but above saturation for palmitic acid (Table 1), whose undissolved solid fraction could

Table 1.

Concentrations and properties of the amino and fatty acids injected into vacuum (Taken from Neveu et al., 2024a)

Compound	**Concentration (mM)**	**Solubility in H_2O at room temperature (mM)**	**pKa**		
			-COOH	**-NH_2**	**Side Chain**
Amino Acid Experiment (Volume 3x200 mL)					
Glycine (Gly)	2	3330.2	2.35	9.78	N/A
Alanine (Ala)	1	1000.1	2.35	9.87	N/A
Glutamic Acid (Glu)	0.4	58.7	2.10	9.47	4.07
Aspartic Acid (Asp)	0.4	31.6	1.99	9.90	3.9
Leucine (Leu)	1	175.3	2.33	9.74	N/A
Threonine (Thr)	0.6	719.4	2.09	9.10	N/A
2-aminoisobutyric acid (AIB)	2	1755.2	2.36	10.21	N/A
γ-aminoisobutyric acid (γAB)	2	998.8	4.53	10.22	N/A
Histidine (His)	1	277.2	1.80	9.33	6.04
Phenylalanine (Phe)	2	99.9	2.20	9.31	N/A
Tyrosine (Tyr)	0.2	2.6	2.20	9.21	10.46
Tryptophan (Trp)	0.1	64.6	2.46	9.41	N/A
Fatty Acid Experiment (Volumes 280 and 470 mL)					
Phenylacetic acid	8	110	N/A		
Palmitic acid	0.5	0.028	N/A		

be seen suspended in solution, presumably as micelles, as well as in clumps at the surface of the solution. The incomplete dissolution of palmitic acid did not affect our ability to detect it in compositional analyses, but prevented quantification of exactly how much palmitic acid was injected into vacuum. The suspended solids were injected, but the surface clumps were not because the inlet of the injection line was dipped below the surface –and often near the bottom– of the injected solutions.

After injection, the chamber was opened and the cup and supporting foil were stored inside sterilized 50-mL polypropylene tubes. The injection line was taken apart and the dry residue, presumably a mixture of salts and amino or fatty acids, was scraped and transferred using fine pointed tweezers or a metal spatula into separate polypropylene tubes for each section of the line: (1) the two valves ("Valves"), (2) the flange attaching the injection line to the vacuum chamber port ("Flange"), (3) the chamber port ("Port"), and (4) the collection cups and supporting foil ("Chamber") (Figure 18). In two pilot injections, the ice on the cold finger (Figure 18a) was also recovered by letting it melt inside a polypropylene tube. Although post-experiment reactivity of the samples was not a concern, all tubes were sealed with Parafilm (not a contamination concern at the relatively high organic concentrations of our experiments) and kept at room temperature at GSFC. Sample tubes were shipped uncooled to Oakland University promptly after completion of the last replicate experiment and received within six weeks of completion of the first replicate injection. Thereafter, sample tubes were kept in a –20ºC freezer until the day of analysis.

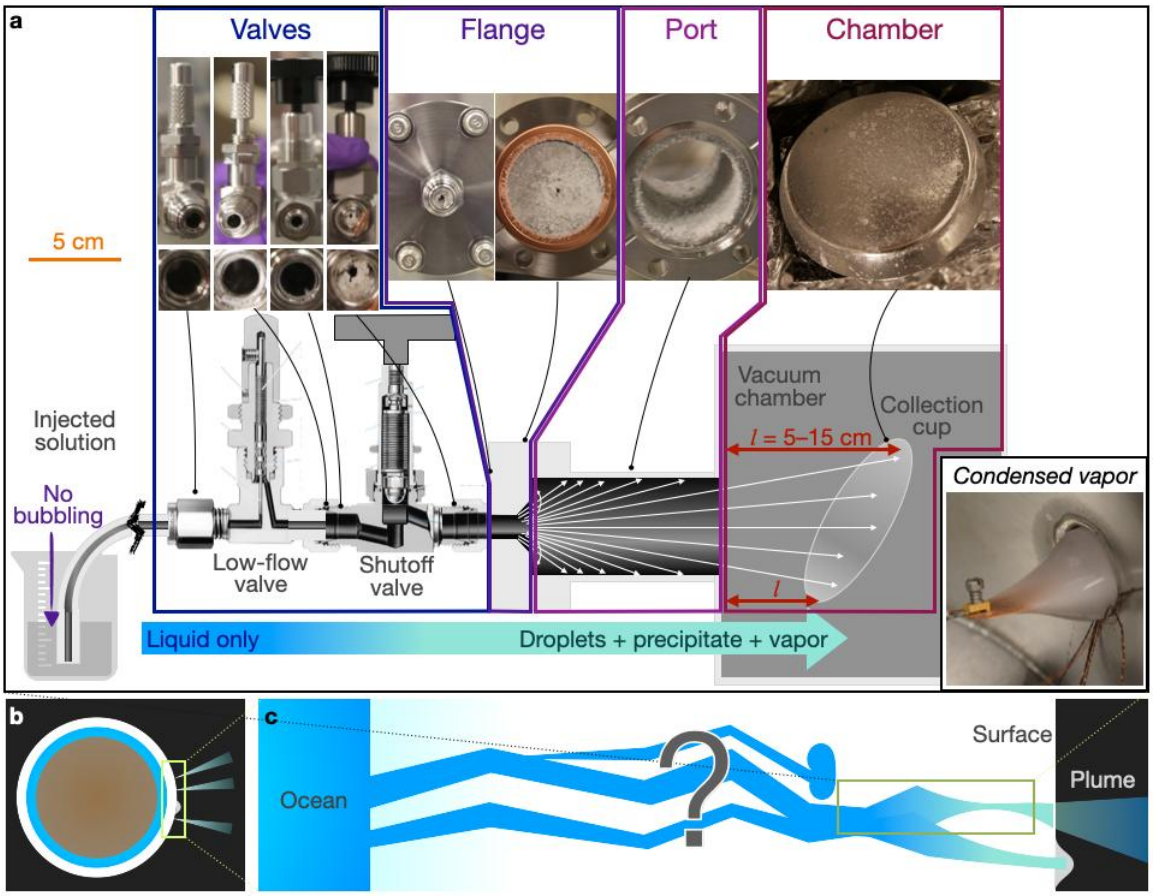

Figure 18. (a) Cutaway, approximately to scale, of the injection line, showing the "valves", "flange", "port", and "chamber" sections in which dry residue was collected post-injection. Photographs taken during sample recovery point to corresponding locations in the line. The inset at bottom right shows vapor condensed as ice on the cryocooled copper plate inside the vacuum chamber, which could be recovered to measure its total organic carbon content. (b-c) Rough correspondence between the injection path and the liquid-vacuum transition undergone by ocean samples erupted on airless icy worlds. The question mark depicts the uncertainty on the nature of the conduit(s) bringing ocean material to the surface (Taken from Neveu et al., 2024a).

4.2.2 Amino Acids Analysis

In the amino acid experiments, the collected samples were extracted using DI water containing 10 mM phenol and 10 mM glutamine. Glutamine (≥99%), and phenol (99%) from Sigma-Aldrich were used as internal standards for amino acid abundance quantification by high performance liquid chromatography (HPLC). DI water (18.2 MΩ•cm) was obtained from Barnstead Nanopure system. The potential salt effect on amino acid quantification was examined by comparing measured abundances of amino acids at identical concentrations in solutions with and without salt (e.g., 1% NaCl plus Na_2CO_3 to adjust the pH to 9.5). The differences observed in retrieved abundances between the salted and unsalted samples on HPLC were < 5%, which is generally less than the uncertainty among replicates (see Figure 19). For the analysis of aromatic amino acids (histidine, phenylalanine, tyrosine, and tryptophan), the samples were directly injected into the HPLC without derivatization. For the analysis of the other eight non-aromatic amino acids, the samples were derivatized following previous methods (Concha-Herrera et al., 2005; Concha-Herrera et al., 2010). Briefly, 2.50×10^{-2} M of o-phthaldialdehyde (OPA) and 5.0×10^{-2} M of N-acetylcysteine (NAC) were prepared in a 1 M boric acid buffer solution (pH 9.5) as the derivatization reagent. The mixture was protected from light with aluminum foil, stored at 4ºC, and prepared on a weekly basis to avoid degradation. An aliquot of 50 µL of the amino acid sample solution was mixed with 500 µL of the derivatization reagent for a 10-min reaction prior to the HPLC analysis. NAC (≥99%), OPA (≥97%), and NaOH (98%) were purchased from Sigma-Aldrich; boric acid (≥99%) was purchased from Alfa-Aesar.

The HPLC (PerkinElmer 200 series) is equipped with a Flexar binary pump, a Shim-pack CLC-C18 column (Shimadzu), and a UV-Vis detector. The mobile phases include a citric acid buffer (A) at pH 6.5±0.1 and acetonitrile (B) (HPLC-grade). Two different mobile phase programs were used for underivatized and derivatized samples. For underivatized amino acids, the mobile phase composition was programmed to start at 100%A (3 min), to 80%A and 20%B (3 min), to 78%A and 22%B (4 min), to 70%A and 30%B (6 min), followed by another hold for 2 min. The mobile phase flow rate was 1.00 mL min^{-1} and the UV detection wavelength was at 225 nm. For the derivatized amino acids, the mobile phase composition was programmed to start at 100%A (1 min), to 97%A and 3%B (2 min), to 90%A and 10%B (10 min), to 80%A and 20%B (20 min), to 75%A and 25%B (6 min) and hold for another minute. The mobile phase flow rate was also 1.00 mL min^{-1} and the UV detection wavelength was at 335 nm. For both methods, 50 µL of sample was injected with a 20 µL sample loop.

4.2.3 Fatty Acids Analysis

In the fatty acid experiments, the samples were first acidified using HCl to ensure the carboxylates were protonated and fully extractable by the organic solvent. The samples were then extracted with dichloromethane (DCM, VWR, 99.9%), vortexed, and centrifuged to separate the organic layer from the aqueous layer following previous procedures (Aspin et al., 2023; Fu et al., 2020a). The aqueous layer was additionally washed twice with DCM, and the DCM extract was combined with the previous organic layer to ensure sufficient extraction. The separation of DCM extract from the aqueous phase also removed the sodium salts (e.g., NaCl and Na_2CO_3) from the protonated fatty acids prior to the gas chromatography (GC) analysis. After evaporating DCM at room

temperature, the solid lipids were redissolved in a 0.5 mL DCM solution containing 0.88 mM decane (Sigma-Aldrich, ≥99%) as the internal standard for GC quantifications (Fu et al., 2020a; Liao et al., 2022).

The GC (Agilent 7820A) is equipped with a poly-capillary column, an autosampler, and a flame-ionization detector. Helium was used as the carrier gas, and the GC oven was programmed to initiate at 50ºC for 8 min, ramp at 10ºC min^{-1} up to 220ºC, hold for 10 min, ramp at 20ºC min^{-1} to reach 300ºC for 5 min. The injection temperature was at 275ºC, and the detector temperature was set to 300ºC with air flow at 400 mL min^{-1}, H_2 flow at 30 mL min^{-1}, and N_2 flow at 25 mL min^{-1}.

4.3 Results

Dry residue was recovered not only inside the vacuum chamber (cups and foil), but also in the chamber port, its cover flange, the shutoff valve (Figure 18), and in some injections, as far upstream as between the low-flow and shutoff valves. Most of the residue coated the inner surfaces of the port and flange, due presumably to a combination of (a) low pressure favoring water loss and solute precipitation, (b) high area for deposition, and (c) a cross-sectional area small enough relative to the port length to allow the flow to interact extensively with the port wall. Further upstream, the line's lower cross-sectional area limited the surface area available for deposition (Figure 18). During injections, precipitate intermittently clogged the line, as evidenced by spontaneous decreases in the injection rate (change in remaining solution volume as a function of time), episodic pressure spikes from the baseline H_2O vapor pressure at the copper plate temperature, and occasional observations of collection cup deflections upon grain impact when increasing the injection flow rate (Supplementary video) concurrent with

precipitate accumulation in the cup. The size of residue grains could only be reliably verified in the collection cup where, unlike in the injection line, the surface was not uniformly coated, allowing observation of individual grains. Sizes were not quantified, but macroscopic inspection (e.g., Figure 18a) confirmed that residue grains had sub-millimeter sizes, presumably extending down to microscopic (Section 4.2).

Aside from a negligible fraction of carbonate salt converted to CO_2 at pH > 9, all solutes are less volatile than H_2O (Section 4.4). The vapor condensed onto the copper plate cold finger during two pilot injections indeed had a total organic carbon content of < 0.015% and < 0.001% of that of the injected solution.

4.3.1 Amino Acid Fractionation

The total mass of each amino acid in all four sections of the flow path was 60% to 120% of their masses in the injected solution, with a recovery of 80 to 110 mass% for most (Figure 19a). The highest measured recoveries are compatible with 100% within two standard deviations from the mean of three replicate injections. We ascribe the measurement uncertainty to variations in sample collection, extraction, dilution, and/or quantification among replicates. Four amino acids had low recovery, more than two standard deviations away from 100%: Asp, AIB, Tyr, and Trp (Figure 19a). Three of those have relatively low solubility in water (Table 1, see also Figure 23a), which might account for some of the losses (e.g., material remaining inside valves or not transferred across steps of the preparation for analysis).

The amount of deposited amino acids increased downstream (Figure 19b) from the valves (10–20% of the mass of each amino acid collected post-injection), through the

flange (22–26%), to the port (50–60%), consistently with the amounts of residue recovered (Figure 18), and with the caveat that the uncertainties on recoveries from the valves and flange sections overlap. In most cases, there was no difference among amino acids within one standard deviation uncertainty. Only 6–12% reached the vacuum chamber.

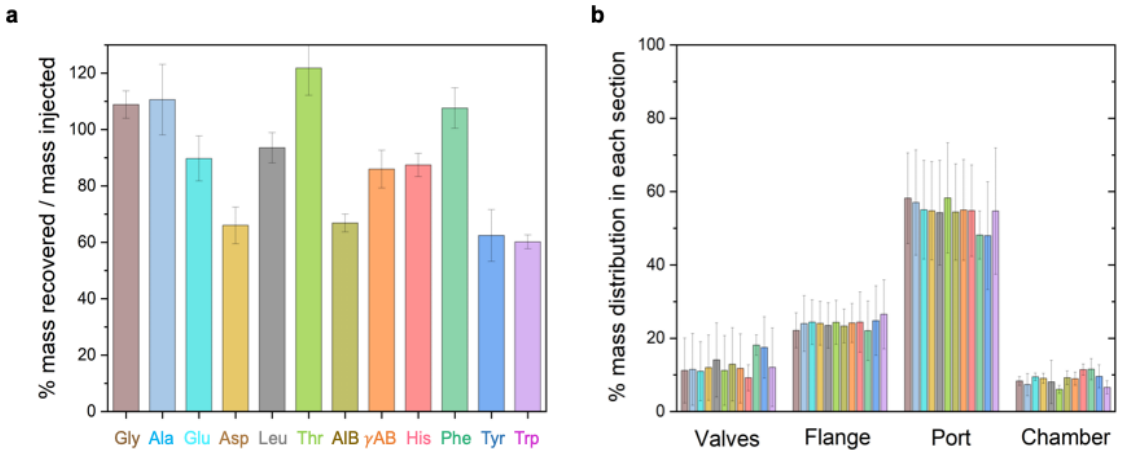

Figure 19. (a) Total recovery (mass%) of each amino acid in all four sections of the injection path (outlined in Figure 18a). (b) Distribution (mass% of total amino acids in (a)) in each section. Error bars indicate one standard deviation from the mean of three replicate injections (Taken from Neveu et al., 2024a).

4.3.2 Fatty Acid Fractionation

Distributions of fatty acids along the injection path were similar: most of the mass was collected in the main port, and a few percent in the chamber (Figure 20a). The total mass of phenylacetic acid recovered in all four sections was 81% of the mass injected, which is consistent with an empirically determined ≈85% efficiency of the lipid extraction method (Section 4.2). However, the total mass of palmitic acid recovered was only 9.9% of the mass that should have been injected with palmitic acid fully dissolved. This low recovery is likely due in part to the incomplete injection of palmitic acid, which

was supersaturated in the injected solution, and in part due to analytical uncertainties arising from recovered palmitic acid amounts (0.1 to 0.8 mg across all flow sections) close to the limit of detection (0.14 mg).

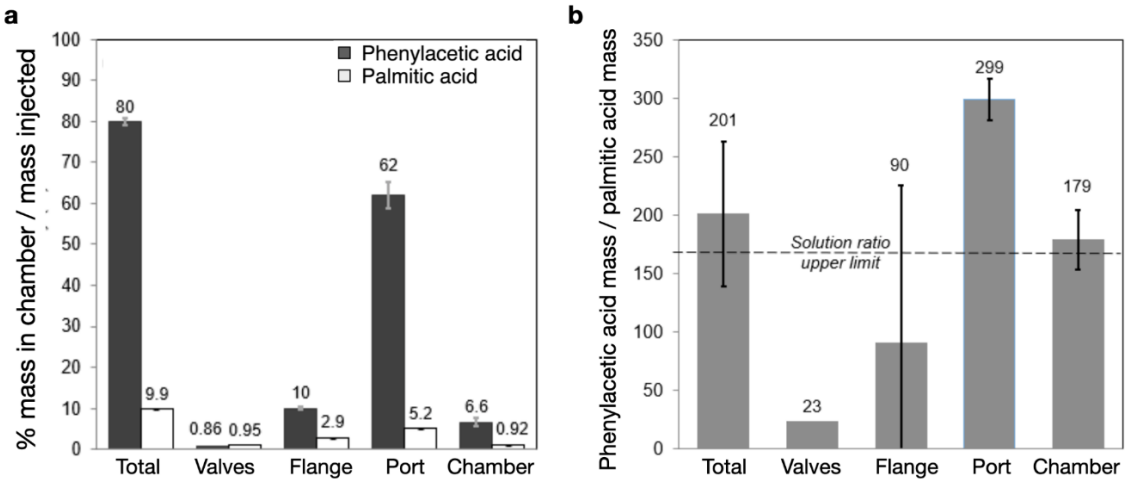

Figure 20. (a) Mass fraction (%) of fatty acids recovered in sections of the injection path relative to the dry mass added to water when preparing the solution for injection. (b) Mass ratio of phenylacetic acid to palmitic acid in each section of the injection path. Error bars indicate one standard deviation (volume-weighted) from the volume-weighted mean of two injections of 280 mL and 470 mL of the same solution (Taken from Neveu et al., 2024a).

Notwithstanding this systematic uncertainty in palmitic acid abundance determination, we observed a striking change in the relative abundance (mass ratio) of phenylacetic acid to palmitic acid in the downstream direction of the flow. This mass ratio was 45 at the valves, increasing to 132 at the flange and 301 in the port (Figure 20b). The ratio in the injected solution is expected to be higher than 8 (had all palmitic acid fully dissolved) and 152 or less (had only palmitic acid dissolved up to saturation been injected, excluding suspended micelles). The upper limit is broadly consistent with the recovered mass ratio in the chamber (182) and summed over all four sections (201) given the uncertain palmitic acid abundance determinations.

4.4 Discussion

4.4.1 Interpretation of Relative Abundance Measurements by Spacecraft

The observed limited amino acid abundance fractionation is sensible in that amino acids have limited volatility relative to water. They are also very soluble in water, with which they primarily interact via the amine and carboxyl functional groups that drive the aqueous behavior of all amino acid compounds investigated here. This suggests a low propensity for selectively coming out of solution as either solid or vapor, even at the high end of conduit temperatures (> 250 K), confirmed by the present experiments.

The changes in relative amino acid abundances between the injected solution and the vacuum environment (chamber; last group of Figure 19b), shown in Figure 21b, do not appear to affect the relative distributions of amino acids in example biological and abiotic samples (Figure 21a) in ways that prevent distinction between these two representative end-member sources (Figure 21c). Barring fractionation processes not produced by our experimental procedure, the proportions of amino acids in material having undergone the liquid-vacuum transition during eruption should be as indicative of their origin as those in the subsurface liquid source. Thus, measurements of amino acid relative abundances by spacecraft that would analyze macroscopic samples (homogenizing grain-to-grain differences) of material having undergone the liquid-vacuum transition during eruption on Europa (Hand et al., 2022) and Enceladus (MacKenzie et al., 2022) should be able to distinguish biological from abiotic end-member sources for these compounds without needing to correct for abundance fractionations arising from this environmental transition. Interpretation of such measurements may need to consider additional processes that could cause abundance

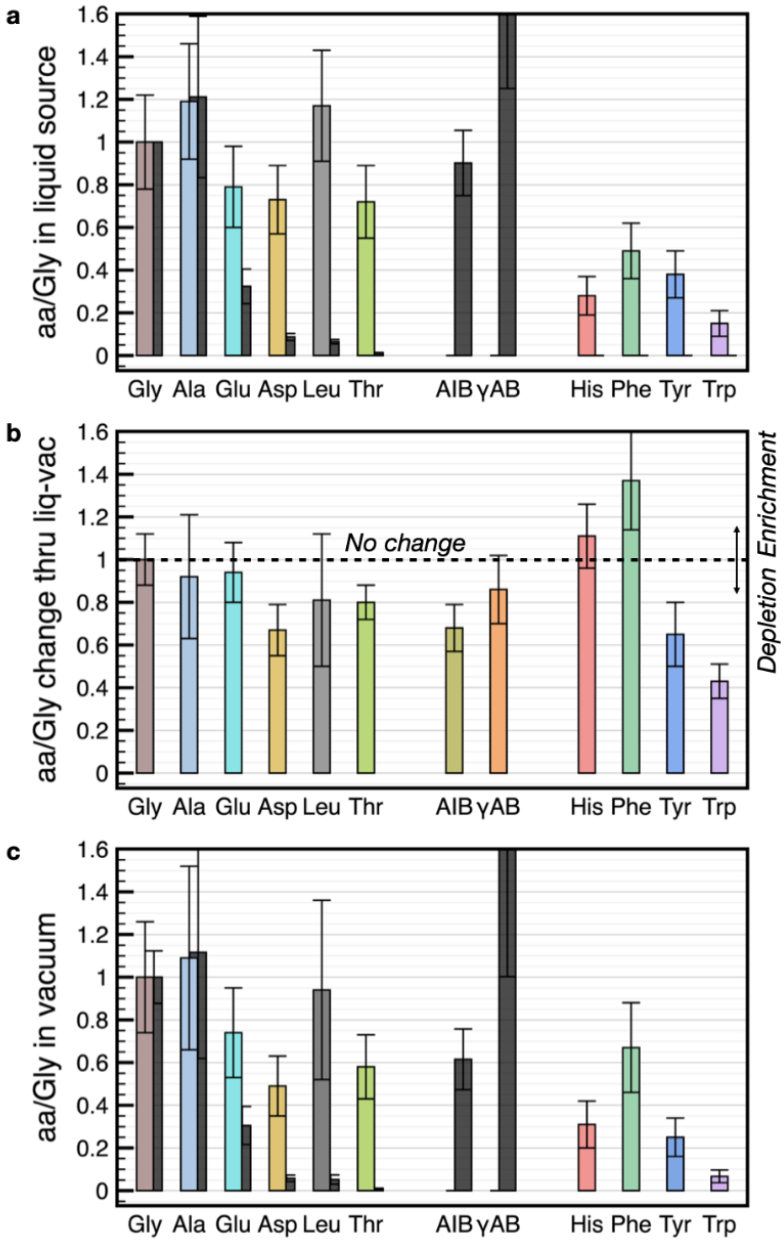

Figure 21. (a) Example biological (colored bars) and abiotic (shifted dark bars just to the right of the colored bars) mass ratios of amino acids to glycine ("aa/Gly") for the twelve amino acids injected. The abiotic γAB:Gly ratio is 2.5±1.3 (off scale). (b) Ratio of Chamber aa/Gly to injected solution aa/Gly for these amino acids. A ratio higher or smaller than 1 indicates, respectively, enrichment or depletion of the corresponding amino acid relative to Gly in vacuum. (c) Same distributions as in (a) but multiplied by the ratios in (b) to show predicted relative amino acid abundances in ejected material with initially example biological or abiotic end-member amino acid abundance distributions. The abiotic γAB:Gly ratio is 2.2±1.2 (off scale) (Taken from Neveu et al., 2024a). *Cont. in Appendix Text C2.*

fractionations, such as space weathering (e.g., irradiation), any possible biases introduced by the sampling altitude or surface location, or the possibility of mixing with material encountered on the way to the surface.

Whether the liquid-to-vacuum transition changes the relative abundances of fatty acids is less clear. The mass ratio of phenylacetic acid to palmitic acid in the vacuum chamber (182±25), may be close to the ratio injected (152, if the palmitic acid injected was only that dissolved to saturation in the parent solution). However, the injected ratio would have been as low as 8.4, had all palmitic acid particulates (suspended and floating) been injected as well. While the suspended material was likely injected, the clumpy floating material was not. This floating material comprised an estimated 87 mg of the 129 mg added during solution preparation (67 mass%), so the injected ratio was likely ≥ 8.4 / (1 – 87/129) = 26 and the mass ratio likely did not change by a factor higher than (182±25)/26 = 7±1.

A factor-of-7 or lesser change in relative abundances could alter patterns arising from relevant example biological and abiotic sources, but likely not so much as to make them unrecognizable. Abiotic straight-chain fatty acids (alkanoic acids) formed in water from formic acid (an expected conversion product of accreted carbon monoxide (Neveu et al., 2015; Shock, 1993) have relative abundances that track those of straight-chained alkanes (McCollom et al., 1999), which themselves decrease monotonically by a factor of 3 between C_n- and C_{n+4}-compounds comprising n = 10 to 24 carbon atoms (McCollom & Seewald, 2006). In microorganisms, alkanoic acid abundances peak at specific carbon numbers (Hamerly et al., 2015), with abundance ratios of 2 to 10 between alkanoic acids

differing by one carbon atom in their chain lengths (Bühring et al., 2005). Thus, a factor of $\leq 7\pm1$ change in the relative abundances of alkanoic acids differing by a few carbon atoms in their chain length would complicate recognition of an abiotic or biological source from abundance patterns (Hand et al., 2016; MacKenzie et al., 2022). However, the liquid vacuum transition would likely cause a much smaller change, as there are much less structural differences between these compounds than between the phenylacetic acid (a short-chain aromatic acid) and palmitic acid (C_{16} alkanoic acid) investigated here.

Amino and fatty acid distributions may well result from a mixture of biological and abiotic end-member sources, but the ability to discern individual source contributions to abundance patterns appears not to be affected much by abundance changes induced by the liquid-vacuum transition. Interpretation of Figure 21c suggests that example biological and abiotic sources would remain identifiable through the presence of amino acids that are not observed in the other end member, such as the right-most six amino acids in Figure 18. Regarding fatty acid abundance patterns, as shown in Figure 22a and 22b, respectively, the dominant modeled example biological (even over odd) or abiotic contribution (decrease with increasing carbon number) to the pattern remains qualitatively identifiable even if the minor contributor accounts for 20% of the signal, assuming the liquid-vacuum transition induces a –likely overestimated– random factor-of-7 change in abundances. In a mixture where modeled biological and abiotic contributions are equal (Figure 22c), the modeled abundance patterns remain qualitatively faintly identifiable, but only if the liquid-vacuum transition changes abundances by a random factor of ≤ 2.

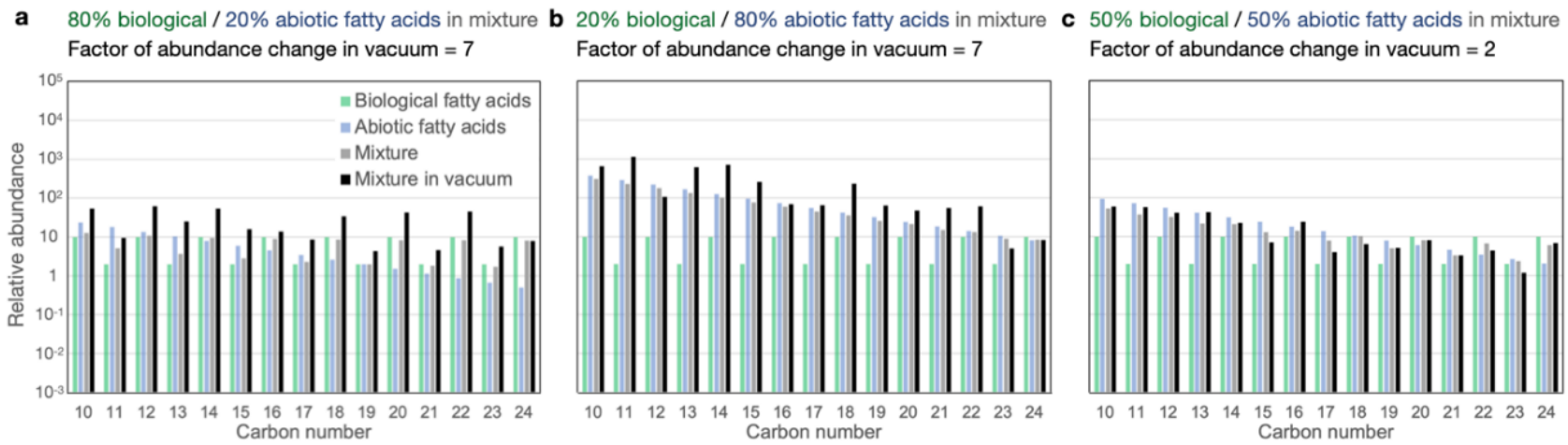

Figure 22. (a) Modeled relative abundance patterns of a mixture of fatty acids deriving from idealized biological and abiotic sources. The modeled biological source (green histograms) has an arbitrary abundances of 10 for alkanoic acids with odd carbon numbers and 2 for those with even carbon numbers (even/odd abundance ratio = 5). The modeled abiotic source (blue histograms) has abundances decreasing by a factor of $3^{1/4}$ between adjacent carbon numbers. The mixture (grey histograms) is the sum of the two. The effect of the liquid-vacuum transition is modeled as a random change in abundances by an arbitrary factor (black histograms). (a) Mixture of 80% biological / 20% abiotic pattern, with a factor-of-7 random abundance change induced by the liquid-vacuum transition. (b) Mixture of 20% biological / 80% abiotic pattern, with a factor-of-7 random abundance change. (c) 50% / 50% mixture, with a factor-of-2 random abundance change (Taken from Neveu et al., 2024a).

4.4.2 Possible Causes for Relative Abundance Changes

Despite overall preservation of amino and fatty acid mass ratios at scales relevant to identifying their source, the liquid-vacuum transition causes up to 50% changes in the mass ratios of amino acids and possibly larger changes in those of phenylacetic and palmitic acid. Below, we investigate possible causes for these changes, arising either from intrinsic physicochemical properties of these compounds or from the experimental procedure. Among these, solubility –and, relatedly, flow rate– appear to have the most effect. While other properties could sensibly fractionate compound abundances, no strong effects of these were observed.

4.4.2.1 *Solubility* The abundant precipitate formed along the fluid path (Figure 18 and 19b), as water is lost to vaporization, suggests that compound solubilities could affect their relative abundances in the chamber. The mass of amino acids in the collection chamber shows a weak increasing correlation with compound solubility (Figure 23a) and injected concentration (Figure 23b). Considering additionally the fatty acid experiment and pilot, singleton injections of amino and fatty acids, compound depletion through the liquid-vacuum transition generally decreases with increasing concentration:solubility ratio (Figure 23c). Lesser saturation may increase the retention of amino and fatty acids in the aqueous phase, thus increasing their propensity for reaching the vacuum environment.

Irrespective of compound solubility, most of the dry residue was recovered from the "Port" section partway through the fluid path (Figure 18 and 19b), rather than inside the chamber. This is in part due to the port's significant surface area (65 cm^2), equivalent to the material deposition area inside the chamber ($\approx$ 60 cm^2 for two collection cups plus

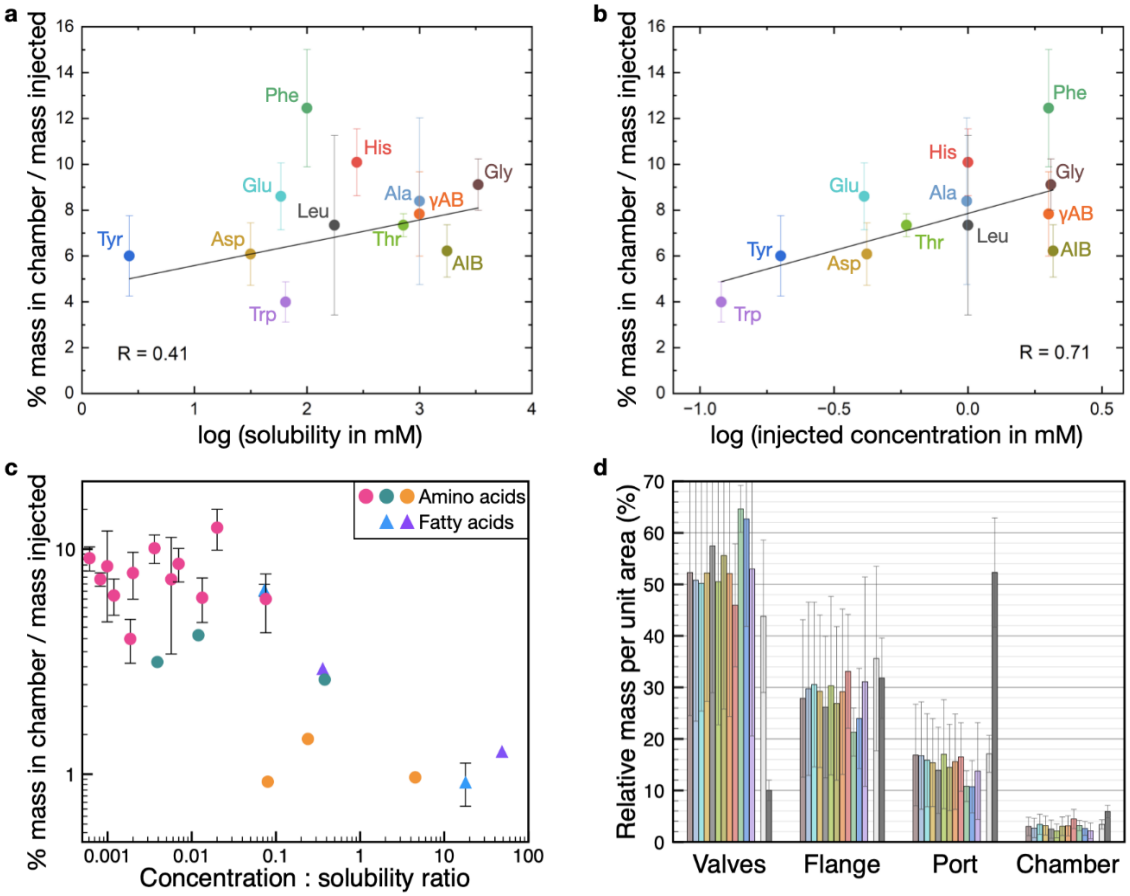

Figure 23. (a) Solubility effect on the propensity of amino and fatty acids for transport through the liquid-vacuum transition. (b) Mass percent of each amino acid in the collection chamber as a function of, respectively, its solubility or injected concentration. Error bars indicate one standard deviation from the mean of three replicate injections. (c) Mass percent of amino and fatty acids, aggregated across experiments, as a function of the ratio of their concentration in the injected solution to their solubility. Circles denote amino acids (pink for the experiment reported here, teal and orange for two pilot singleton injections; triangles denote fatty acids (blue for the experiment reported here, purple for one pilot singleton injection). Error bars indicate one standard deviation from the mean of three or two replicate injections (pink or blue data points, respectively). (d) Areal mass density of organic acid (color coded as in Figure 16b and 17a) per section of the injection path, relative to the areal mass density averaged across the full injection path. Error bars indicate uncertainty propagated from one standard error from the mean of three or two replicate injections (amino or fatty acids, respectively). For the fatty acids in (d), the standard error is the volume-weighted standard deviation from the volume-weighted mean, divided by $\sqrt{2}$ (Taken from Neveu et al., 2024a).

part of the support foil; Figure 17b). Scaling Figure 19b and 20a to the estimated surface area of deposition for each section (≈ 18 cm^2 for the Flange, 26 ≈ 5 cm^2 for the Valves), most relative areal mass densities of compounds decrease monotonically in more downstream sections (Figure 23d).

On icy moons, expected amino and fatty acid concentrations in the subsurface ocean are much lower (sub-micromolar; Section 4.2) than in the millimolar solutions we injected. Lower concentrations may lessen the effect of solubility on relative abundance fractionation for these compounds. So, too, may the lower temperatures of eruption conduits relative to the 30ºC±15ºC of our injection line (Section 4.2.1), because less water would be lost from the condensed phase. However, for more concentrated and possibly less soluble compounds such as those observed and inferred to be sourced from subsurface liquid water at Enceladus (~0.03 mM; (MacKenzie et al., 2022; Postberg et al., 2018b) and Ceres (percent-level abundances in surface materials; (Daly et al., 2023; Kaplan et al., 2018), precipitation could both coat the eruption conduit walls with precipitate whose solubility decreases with increasing depth and skew relative abundances in materials exposed to vacuum during eruption.

4.4.2.2 *Volatility* Vaporization or sublimation of amino and fatty acids is an improbable cause of abundance fractionation. First, the total organic content measured in vapor condensed inside the vacuum chamber was negligible. Second, amino and fatty acids are less volatile than water: although –to our knowledge– unreported, their vapor pressures should be lower, and their triple points at higher temperature and pressure, than those of smaller acetic acid (CH_3COOH), whose vapor pressure is itself lower, and triple point higher, than those of H_2O (NIST, 2023, and references therein).

4.4.2.3 *Charge and Organic-Salt Interactions* The respective pH of the injected amino and fatty acid solutions were 9.2 and 9.7. At pH 9.2, the carboxyl groups of the amino acids are deprotonated (COO^-) because of their low pKa values (1.8–2.4), whereas the amine groups could be protonated (NH_3^+; pKa 9.1–10.5). Amino acids Asp, Glu, His, and Tyr also have pH-sensitive side chains with pKa 3.9–10.4. At pH 9.7, phenylacetic acid and palmitic acid too were present as their carboxylates (pKa 4.31 and 4.95, respectively). The COO^- groups of amino and fatty acids likely interact with the Na^+ in solution; protonated amine groups and charged side chains could also affect ionic interactions with the salts.

Such organic-salt interactions can fractionate relative abundances of lipids at liquid water-gas interfaces (Cochran et al., 2016), and co-locate glycine and (more strongly) aspartic acid with salts in frozen brines of sodium chloride and carbonate, particularly with sodium carbonate due its higher charge density (Vu et al., 2023). Because salts are in large excess (mass%-level) both in our experiments and in relevant icy world environments (Castillo-Rogez et al., 2018; Melwani Daswani et al., 2021; Postberg et al., 2011) relative to amino and fatty acids, partial precipitation of salts along the liquid-vacuum path could induce co-precipitation of these organic acids that can fractionate their relative abundances. We measured no significant effect on the ratio of {mass in chamber} to {mass injected} between overall negatively charged Tyr, Asp, Glu, and Thr and the other, overall electrically neutral amino acids (Figure C1), suggesting no detectable effect of organic salt interactions on abundance fractionations at this macroscopic scale. However, we cannot exclude that the possibly different organic-salt interactions resulting from the expected cooling rates at Enceladus, which are likely to be

much lower than those of our experiments (Section 4.2.1), could fractionate amino acids depending on their electrical charge.

4.4.2.4 *Chemical Structure and Functionality* The investigated amino acids consist of both aromatic and non-aromatic structures, some more electrically polar and others more hydrophobic (Bull & Breese, 1974). Studies of aerosol formation from aqueous solutions (e.g., seawater) have shown that amino acids could affect aerosol properties such as surface tension, surface activity, hygroscopicity, and potential surface reactions (Herboth et al., 2021; Marsh et al., 2017), and that pH can play an important role in the amino acid distribution in aerosols. For example, hydrophilic amino acids such as Gly tend to be distributed in the bulk of aerosol droplets, whereas amphiphilic and hydrophobic amino acids such as Ala and Phe tend to be located on droplet surfaces. Although the aerosol studies were carried out at 1 bar, the chemical properties of amino acids may also shape patterns of distribution at solid liquid-vapor interfaces at the sub-P_t regime investigated here.

However, these properties do not appear to affect the ratio of {mass in chamber} to {mass injected} for specific amino acids (Figure C2 and C3). The polar-basic His, as well as Gly, have a slightly higher ratio than the polar-neutral Thr, but the effect is small. If chemical structure and functionality influence the ability of organic compounds in solution to be transported to vacuum environments in water droplets or grains, this influence appears to be similar among compounds that all have in common carboxyl and amine functional groups.

4.4.2.5 *Flow Rate* As observed during experiments, higher fluid flow rates can move more solutes along the fluid path by limiting the gradual loss of water and can

mechanically dislodge prior precipitate. Despite the use of a low-flow valve, flow rate was only coarsely controlled during the injection experiments because precipitation tended to effectively decrease conduit diameters in a way that could be neither quantified nor adjusted. Thus, the flow rate could vary across the full practical 1–25 mL h^{-1} range during individual experiments.

The effect of such variable flow rates on the distributions of organic precipitate along the fluid path may be captured by replicate-to-replicate differences in these distributions (error bars in Figure 19, 20, 21b, and 22; standard deviations in Table C1). These variations were generally a few percent of the injected mass of each compound. Variations relative to the amount of material deposited in each section of the injection path were about 20–65%. The highest relative variations were in the valves, which are both the farthest (highest-pressure) section from the vacuum chamber and the section with the lowest volume and surface area, i.e., the most sensitive to variations in flow rate. The lowest relative variations were in the chamber port, where the most material was deposited.

Flow rate thus likely acts in combination with solubility to affect the distribution of organic precipitate along the fluid path, both in these experiments and in eruption conduits at ocean worlds. We suspect that the effects of solubility discussed above are increasingly pronounced at lower flow rates. In addition to flow rate, other factors such as salt content may also influence the solubility of organic acids, especially for those with low solubility (e.g., palmitic acid). Future experiments with varying salt composition and concentration are needed to identify other drivers for changing relative abundances of biosignature compounds in cryovolcanic ocean worlds.

4.5 Conclusions

The liquid-vacuum transition does not appear to alter relative abundances of amino and fatty acids enough to prevent distinction between end-member example biological or abiotic sources. Measured changes in relative abundances are primarily attributed to differences in compound concentrations in relation to their solubility in water, but these changes are only significant over a wide range of concentration:solubility ratios. Their importance may be modulated by the fluid flow rate, and may be lower at ocean worlds where amino and fatty acid abundances are expected to be orders of magnitude more diluted than in the present experiments. Thus, barring fractionation processes not produced by our experimental procedure, the proportions of amino and fatty acids in erupted material –measurable by spacecraft– having undergone the liquid-vacuum transition should broadly reflect those in the subsurface liquid source.

CHAPTER FIVE

SUSTAINABLE DEGRADATION OF PLASTICS USING HYDROTHERMAL CATALYSIS

5.1 Introduction

Plastic has become an integral part of the modern world, offering many valuable characteristics suitable for everyday life. Its durability, versatility, low cost, ease of manufacturing, and chemical resistance have contributed to its widespread use in the packaging, construction, automotive, electrical, and healthcare industries. Due to its excellent performance and extensive functionalities, global plastic production has surged to over 300 million tons in 2017 compared to just 15 million tons in 1964 (Zhao et al., 2018a; Zhao et al., 2018b). Simultaneously, the rate of plastic waste accumulating in the environment is increasing yearly. In 2016, estimates of global waste emissions into bodies of water (i.e., rivers, lakes, oceans) ranged from 9-23 million tons, with an additional 13-25 million tons emitted into terrestrial environments (Borrelle et al., 2020; Lau et al., 2020). The collective amount of plastic waste released into the environment is projected to increase to well over 100 million tons per year by 2050 assuming a business-as-usual scenario with no significant changes in plastic production or consumption (Cordier et al., 2021; Lau et al., 2020; Lebreton & Andrady, 2019).

Plastic pollution is ubiquitous across the world, with plastic particles being found within the ocean (Koelmans et al., 2017), at the seafloor (Tekman et al., 2020), in terrestrial soils (Bläsing & Amelung, 2018), on Mount Everest (Napper et al., 2020), and even in precipitation like snow or rainwater (Bergmann et al., 2019; Brahney et al.,

2020). The accumulation of these synthetic polymers in the environment can have detrimental effects on the health of ecosystems. Over 900 marine species and 50 fresh-water species are known to have ingested plastics or become entangled within the debris (Gall & Thompson, 2015; Kühn & van Franeker, 2020; Rochman et al., 2016). Additionally, due to the pervasiveness of plastics in the terrestrial environment, it is also common for wildlife to interact with the polluted plastics. For example, terrestrial birds have been shown to ingest microplastics (Zhao et al., 2016) and bees have been observed to incorporate polyurethane and polyethylene plastic wastes into their nests (MacIvor & Moore, 2013). Humans, who use and interact with plastics daily, are exposed to high amounts of microplastics through the ingestion of contaminated food or beverages, the inhalation of dust and fragments from clothing or furniture, and via dermal contact with the plastics (Sun & Wang, 2023). Indeed, microplastics have been detected within blood (Leslie et al., 2022) and even in human placentas (Ragusa et al., 2021). These studies all point to the fact that plastic pollution is widespread within the environment and is detrimental to the health of ecosystems. It is thus crucial to address the problem and take transformative steps to prevent such accumulation.

Traditional handling of plastics includes disposal in landfills, incineration, and primary and secondary recycling. It has been estimated that 60% of all plastics ever produced are accumulating in landfills or the natural environment (Geyer et al., 2017), which many developing countries use as the primary method of waste disposal to reduce handling costs. However, disposal in landfills often results in the breakdown of plastics to microplastics, which can spread and leak into nearby waterways or surrounding soils. In addition, the microplastics can adsorb other pollutants such as heavy metals or organic

contaminants, and act as a vector to carry the pollutants to the surrounding environment (Sui et al., 2017). Comparatively, 12% of all plastic waste has been incinerated, which is an alternative method used when space is limited. This method is often viewed as a "terminator" of plastic waste as it was thought the plastic completely degrades during combustion, however, recent studies confirmed that micro- and nano-plastics are left behind in incineration plants (Shen et al., 2021; Yang et al., 2021) and can be a source of microplastic emission into the surrounding environment. Additionally, the incineration process can lead to the production of greenhouse gases, along with the release of toxic chemicals and air pollutants, which can subsequently affect human and animal well-being (Kasmuri et al., 2022). Primary and secondary recycling is the recycling of waste plastic and accounts for only 9% of all plastic ever produced (Geyer et al., 2017), which can be processed into products with similar or inferior properties. These methods suffer from some drawbacks, such as the need for separation by plastic type, the presence of impurities that need to be thoroughly washed, an additional drying stage, and the low number of cycles plastics can be recycled (Mwanza, 2021). In fact, only about 10% of the recycled plastic (~1% of all produced plastic) is recycled more than once (Geyer et al., 2017). After the recycled material loses its properties, the waste is then disposed of traditionally, either in landfills or incineration. Thus, primary and secondary recycling simply delays the disposal in landfills or incineration, rather than avoiding it.

The concept of tertiary recycling has gained traction in recent years, whereby the plastic waste is degraded by thermal or chemical means to recover the chemical monomers to then be used as feedstocks for repolymyerization of synthetic polymers or redirected into other applications such as fuels (Mwanza, 2021). There are different types

of tertiary recycling, including pyrolysis, gasification, and chemolysis (Helmer Pedersen & Conti, 2017; Lee & Liew, 2021; Mwanza, 2021). Pyrolysis refers to the breakdown of polymers into smaller intermediate products in the presence of heat and the absence of oxygen (Lee & Liew, 2021), oftentimes at temperatures up to 850^{o}C (Shah et al., 2023). The products from pyrolysis are mostly in the liquid form and contain organic acids, phenols, polycyclic aromatic hydrocarbons, and alcohols. Gasification is a similar process, however, temperatures are even more extreme, ranging from 800-1,100^{o}C if oxygen is present and up to 1,500^{o}C without oxygen (Shah et al., 2023). In this recycling method, gaseous products are the most commonly formed fractions. Chemolysis is the targeted chemical depolymerization of plastics (i.e., hydrogenolysis, methanolysis, hydrodeoxygenation). However, this method often requires the addition of a catalyst and only works for condensation polymers like polyethylene terephthalate, but not for additive polymers like polypropylene and polystyrene (Al-Salem et al., 2017; Yadav, 2024). In general, these tertiary recycling methods require toxic catalysts and harsh reaction conditions, making them not so green or sustainable.

Hydrothermal treatment, however, is recognized as an appealing thermochemical technique and is widely used in various applications, including waste biomass recycling (Alper et al., 2020; Shi et al., 2013b), decontamination of sewage sludge (Malhotra & Garg, 2020; Shan et al., 2023), and even plastic waste upcycling (Helmer Pedersen & Conti, 2017; Thunman et al., 2019; Zhao et al., 2018b). Water at elevated temperatures and pressures possesses unique characteristics that can promote organic reactions. For example, the dielectric constant decreases with increasing temperature, indicating its ability to act as an organic solvent and better dissolve insoluble compounds or polymers

(Heger et al., 1980). Additionally, the elevated dissociation constant of water enables it to directly participate in organic reactions as an acid or base catalyst (Holzapfel, 1969). Compared to the other tertiary recycling methods, hydrothermal treatment occurs under much milder temperatures (<300^{o}C), without the need for toxic catalysts, and in the most environmentally available and benign reaction medium, making it a more green and sustainable recycling method.

In this project, we study the hydrothermal treatment of plastics to determine their recyclability under hydrothermal conditions. Two types of plastics are chosen to study, including polystyrene and polycarbonate, as they vary structurally. Polystyrene represents a polymer with an entirely C-C backbone while polycarbonate is a polymer containing C-O bonds in the backbone. Additionally, the effect of Earth-abundant and nontoxic minerals (i.e. hematite, magnetite, sphalerite, quartz) on plastic conversion is investigated for their potential use as catalysts for plastic recycling.

5.2 Materials and Methods

5.2.1. Materials

Polystyrene (≥95%; average M_w ~350,000) and polycarbonate were purchased from Sigma-Aldrich and used for the hydrothermal experiments. Intermediate compounds such as styrene (99%), ethylbenzene (98%), cumene (99%), toluene (98.5%), α-methylstyrene (analytical standard), phenol (99%), and bisphenol A (≥99%) were purchased from Sigma-Aldrich. Minerals including iron(III) sulfide (Fe_2S_3; 99.90%), sphalerite (ZnS; 98%), and corundum (Al_2O_3; 99.70%) were purchased from Alfa-Aesar, while quartz (SiO2), hematite (Fe_2O_3; ≥99%), and magnetite (Fe_3O_4; 97%) were purchased from Sigma-Aldrich. Dichloromethane (DCM, 99%) was obtained from VWR

and was used as the organic solvent for the extraction of reaction products. Hydrochloric acid (50%; VWR) was purchased from VWR and used to acidify the extracted solutions. Decane (99%) and dodecane (≥99%) were purchased from Sigma-Aldrich and used as the internal standards for gas-chromatography (GC) quantitative analysis. Deionized water (18.2 MΩ) was obtained from a Barnstead Nanopure system.

5.2.2. Methods

Hydrothermal experiments were conducted following previously developed methods (Aspin et al., 2023; Fu et al., 2020a; Liao et al., 2021). Briefly, 5 mg of PS or PC were loaded into fused-silica glass tubes (6 mm OD × 2 mm ID), and 0.3 mL of Ar-purged deionized (DI) water was added using a gas-tight syringe. In mineral experiments, 5 mg of a mineral was added to the tube before DI water. The oxygen was then removed by three freeze-pump-thaw cycles and the tubes were sealed with an oxyhydrogen flame under vacuum while submerged in liquid nitrogen. The tubes were then placed in a preheated GC oven at the desired reaction temperature (250°C for PC and 275°C-300°C for PS), for the desired reaction time (1 hr – 1 week). After the desired reaction time, the tubes were removed from the ovens and placed in a room-temperature water bath, which quenches the hydrothermal reaction.

Extraction of the samples followed previously developed methods (Aspin et al., 2023; Fu et al., 2020a). Briefly, the samples are extracted with 3 mL of an organic solvent (dichloromethane; DCM) containing 8.8 mM decane or dodecane as the internal standard (for the PS and PC experiments, respectively). The samples were then acidified 50 µL of 4 M HCl, vortexed, and centrifuged for 3 minutes at 3000 rpm to ensure full separation of the organic and aqueous layers. The organic layer was collected in a glass

vial and injected on an Agilent 7820A gas chromatography (GC) equipped with a poly-capillary column and a flame-ionization detector. Calibration curves for reaction products were prepared using analytical standards and used to quantify the product concentrations from GC. Products were also identified using GC-mass spectrometry (Agilent 7820A/5975C) based on fragmentation patterns and database matching.

5.3 Results and Discussion

5.3.1 Hydrothermal Degradation of Polystyrene

Under the conditions studied (300^{o}C and 86 bar), polystyrene degradation was slow, with ~15% conversion after 48 hrs. The major products contain alkenes (styrene and α-methyl styrene) as well as alkanes (ethyl benzene and cumene). At shorter reaction times, the alkenes are formed in higher concentrations than the alkanes, with styrene being the major product for up to 24 hrs (Figure 24). After 6 hrs, the alkanes begin to accumulate, with ethyl benzene becoming the major product at 24 hrs. Toluene is also observed to form in longer reaction times, although in smaller amounts than all other products even at 48 hrs. Coupling of the aromatic compounds is also observed, forming 1,3-diphenylbutane from two monomers. Similar product distributions on high-impact polystyrene (copolymer of polystyrene and butadiene) or polystyrene degradation under hydrothermal conditions have also been reported (Bai et al., 2019; Kwak et al., 2006; Zhao et al., 2018a; Zhao et al., 2018b).

A proposed pathway for polystyrene degradation is shown in Figure 25. Polystyrene first breaks down into monomer alkenes (styrene and α-methyl styrene), followed by hydrogenation to form the corresponding alkanes (ethyl benzene and cumene, respectively). Additionally, the experiments beginning with alkenes confirm that

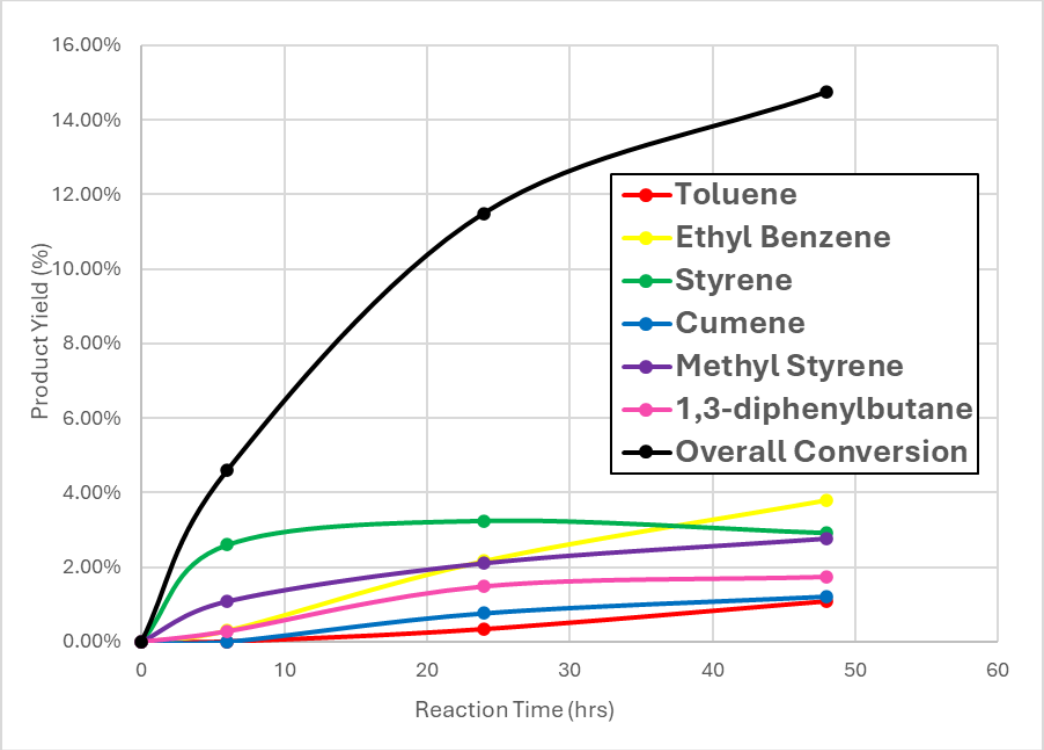

Figure 24. Product distributions of polystyrene experiments for up to 48 hrs, studied at 300°C, 86 bar.

hydrogenation to alkanes can occur, showing cumene's formation from α-methyl styrene and ethyl benzene formation from styrene. This is in agreement with a study by Kwak et al., who showed a decrease in styrene selectivity and an increase in ethyl benzene selectivity at longer reaction times at 400°C and 280 bar (Kwak et al., 2006). The product 1,3-diphenylbutane is also observed in the hydrothermal experiments starting with styrene, but not in the α-methyl styrene experiments, suggesting that coupling of styrene molecules or its breakdown products could lead to the formation of the coupling product.

Previous studies on hydrothermal degradation of plastics report free-radical mechanisms for the depolymerization of the plastic or for the recombination to form the small aromatic compounds (i.e. α-methyl styrene, cumene, toluene; (Seshasayee &

Savage, 2020; Zhao et al., 2018a). However, these studies were conducted at much higher reaction temperatures than here, up to 450°C, which may promote free-radical reactions (Bühler et al., 2002; Seshasayee & Savage, 2020). In general, supercritical water promotes free-radical reactions because the density of water is much lower at temperatures above the critical point. Conversely, ionic reactions are more favorable in subcritical water, where the density remains high enough to support hydrogen bonding (Seshasayee & Savage, 2020). In this study, polystyrene degradation was investigated well below the critical temperature of water, suggesting an ionic mechanism may be likely.

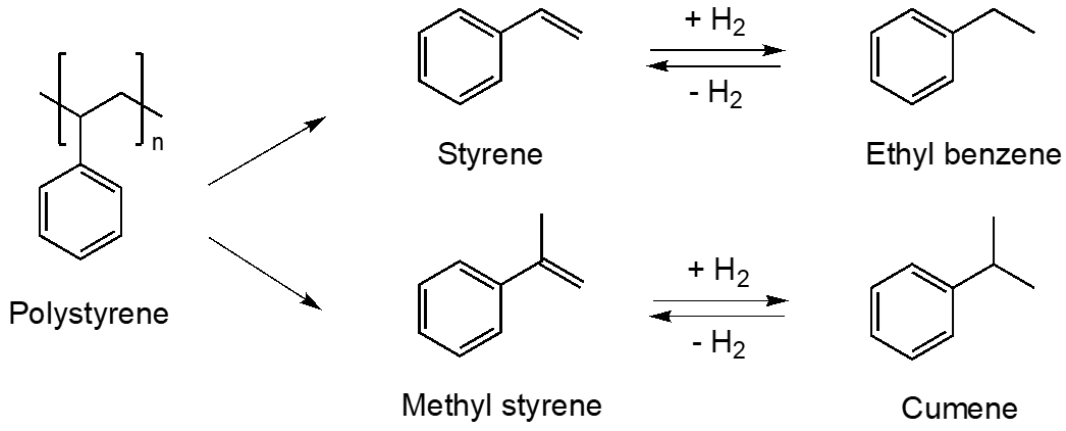

Figure 25. Proposed hydrothermal degradation pathways of polystyrene (300°C, 86 bar)

5.3.2 Hydrothermal Degradation of Polycarbonate

Compared to polystyrene, polycarbonate degraded much quicker under hydrothermal conditions. At lower reaction temperatures (250°C), the overall conversion of polycarbonate reached ~76% (Figure 26). Bisphenol A (BPA) is the major product at earlier reaction times, increasing to roughly 15% yield after only 4 hrs. After 4 hrs, the BPA yield begins to decrease, corresponding to a sharp increase in phenol, which

becomes the major product at 6 hrs (53% yield). Small amounts of phenol-like compounds are also formed (<3% collectively after 6 hrs), including isopropenyl phenol and isopropyl phenol. Similar products from the hydrothermal degradation of polycarbonate have been reported in other studies (Seshasayee & Savage, 2020; Zhao et al., 2018a; Zhao et al., 2018b). Additionally, a coupling product, 1,2,3,4-tetrahydro-1,1,6-trimethyl naphthalene is also observed in up to 15% yield after 6 hrs.

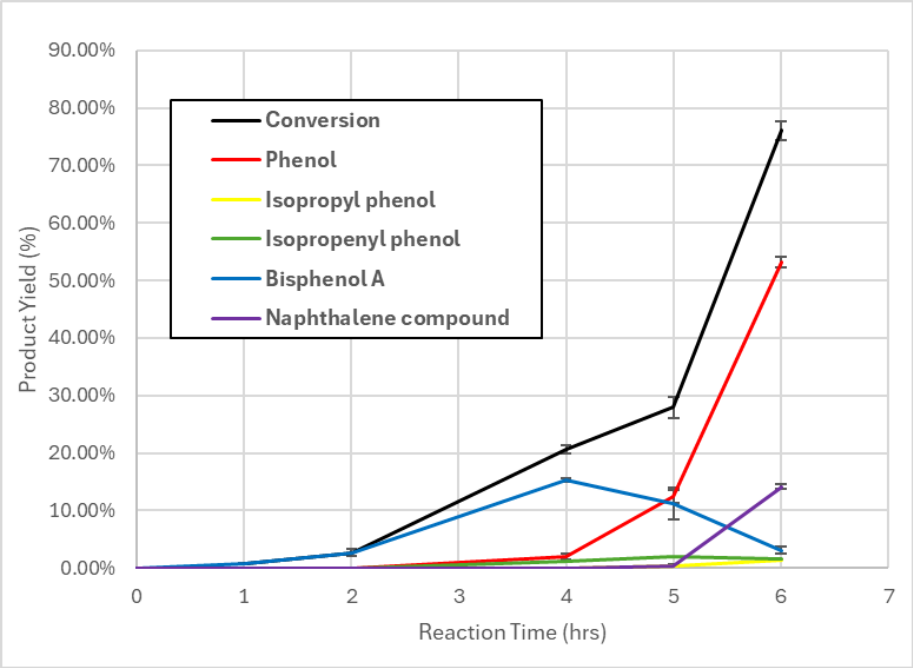

Figure 26. Product distribution of polycarbonate experiments up to 6 hrs (250°C, 43 bar)

The proposed decomposition mechanism of polycarbonate under hydrothermal conditions is shown in Figure 27. Based on the time-series data, it is likely that polycarbonate first undergoes hydrolysis of the carbonic ester bond, forming BPA as the primary product. The BPA can then break further to form phenol, isopropyl phenol, and isopropenyl phenol. Like polystyrene, previous studies investigate polycarbonate degradation under higher temperatures (up to 450°C) and report a free-radical mechanism

(Zhao et al., 2018a). In this study, however, a much lower reaction temperature of 250°C was used, suggesting an ionic mechanism may be more likely. Further reactions between phenol and its derivatives are also expected to occur. For example, the conversion of isopropenyl phenol to isopropyl phenol is plausible, as hydrogenation has been shown to occur under hydrothermal conditions (Seewald, 1994; Shipp et al., 2013a). Additionally, isopropenyl phenol can likely be further degraded to phenol (Zhao et al., 2018a).

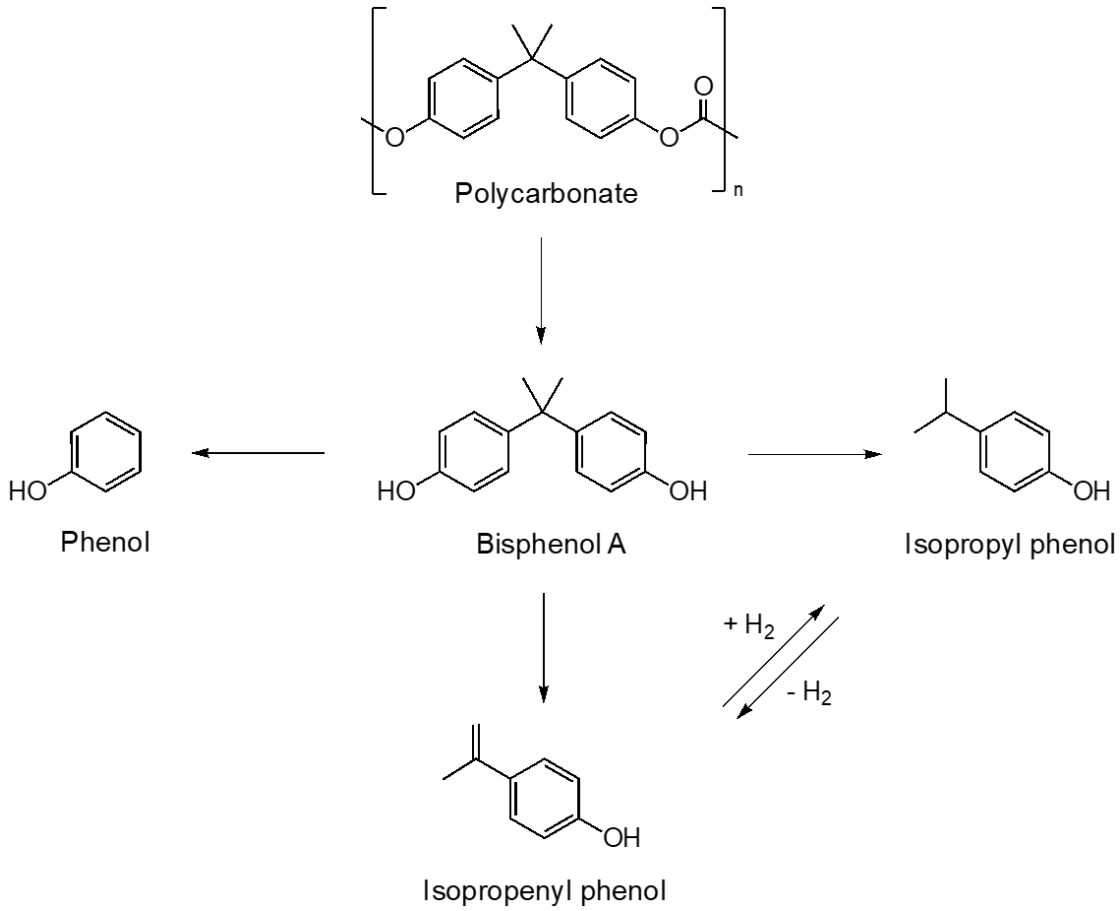

Figure 27. Proposed hydrothermal degradation pathways of polycarbonate (250°C, 43 bar)

5.3.3 Influence of Minerals and Metal Salts on Hydrothermal Plastic Degradation

Although the degradation of polystyrene and polycarbonate was observed to occur at high temperatures in pure DI water, the addition of Earth-abundant and nontoxic minerals may enhance their conversion to make this recycling technique even more green and sustainable. A suite of different minerals was selected to study based on their widespread availability and low cost, including oxides (hematite, Fe_2O_3; magnetite, Fe_3O_4; corundum, Al_2O_3), sulfides (iron(II) sulfide, FeS; sphalerite, ZnS), and a silicate (quartz, SiO_2). These minerals have also been shown in previous studies to influence organic reaction pathways in hydrothermal systems. For example, hematite and magnetite are known to control the redox state of hydrothermal fluids, which can control redox reactions like (de)hydrogenation of alkanes and alkenes (Shock et al., 2019; Venturi et al., 2017). In addition to controlling the redox state of the solution, iron oxide minerals have been shown to act like surface catalysts, promoting bond-cleavage and bond-coupling reactions (Yang et al., 2018) and by facilitating the oxidation of carboxylic acids (Johnson-Finn et al., 2021). As another example, sphalerite can activate carbon-hydrogen bonds by breaking and making a covalent bond (Shipp et al., 2013b).Thus, it is of interest to investigate their potential role in controlling plastic degradation as a green and sustainable additive.

The effect of minerals on hydrothermal polystyrene degradation is studied at 275^{o}C for 7 days. The overall yield of degradation products remained relatively constant, at about 13-14%, with no clear difference among the tested minerals (Figure 28). The product distributions are also similar in the presence of different minerals compared to DI water alone, comprised of alkenes (styrene and α-methyl styrene) and alkanes (ethyl

benzene and cumene). No new products were identified and no products disappeared in the mineral experiments compared to those without minerals added.

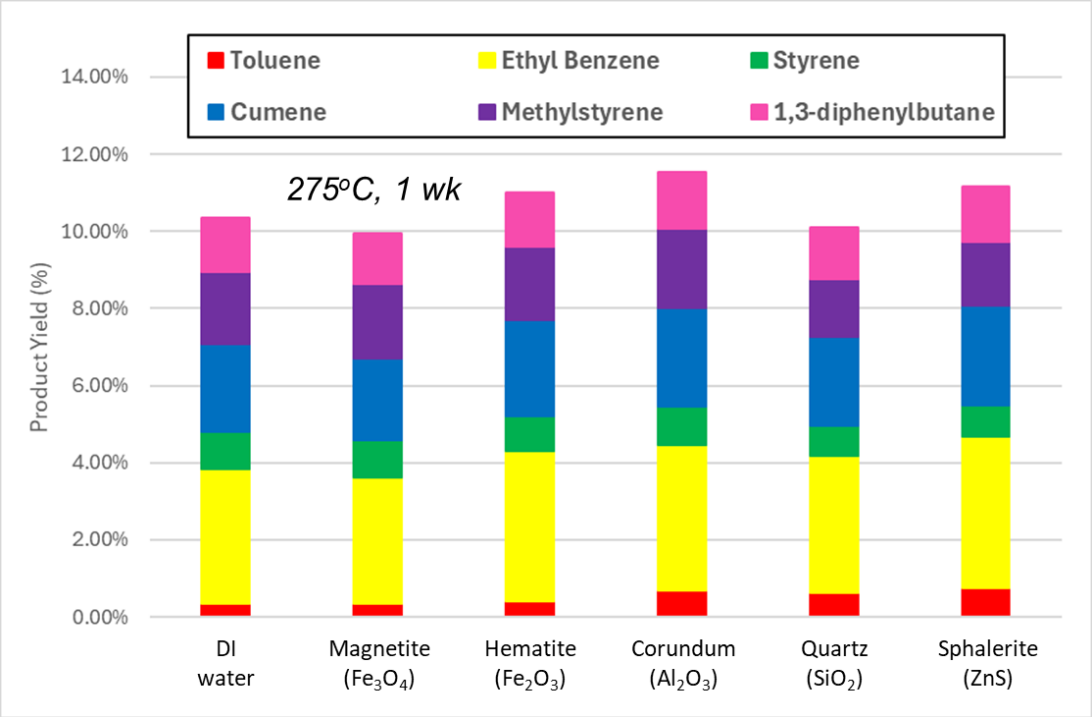

Figure 28. Effect of minerals on polystyrene conversion (275°C, 1 wk)

Conversely, each mineral is observed to promote the degradation of polycarbonate under hydrothermal conditions. At the studied conditions (250°C, P_{sat}), polycarbonate conversion was ~28% after 5 hrs in pure DI water. The oxide minerals (hematite, magnetite, corundum) slightly enhanced the conversion to 33-38%, while the sulfides (iron(II) sulfide, sphalerite) and quartz increased it to 43-63% (Figure 29). The product distributions were also affected by the addition of minerals, most of which increased the selectivity for phenol compared to pure water experiments (Figure 29). Isopropenyl phenol production was also enhanced in the presence of iron-containing minerals.

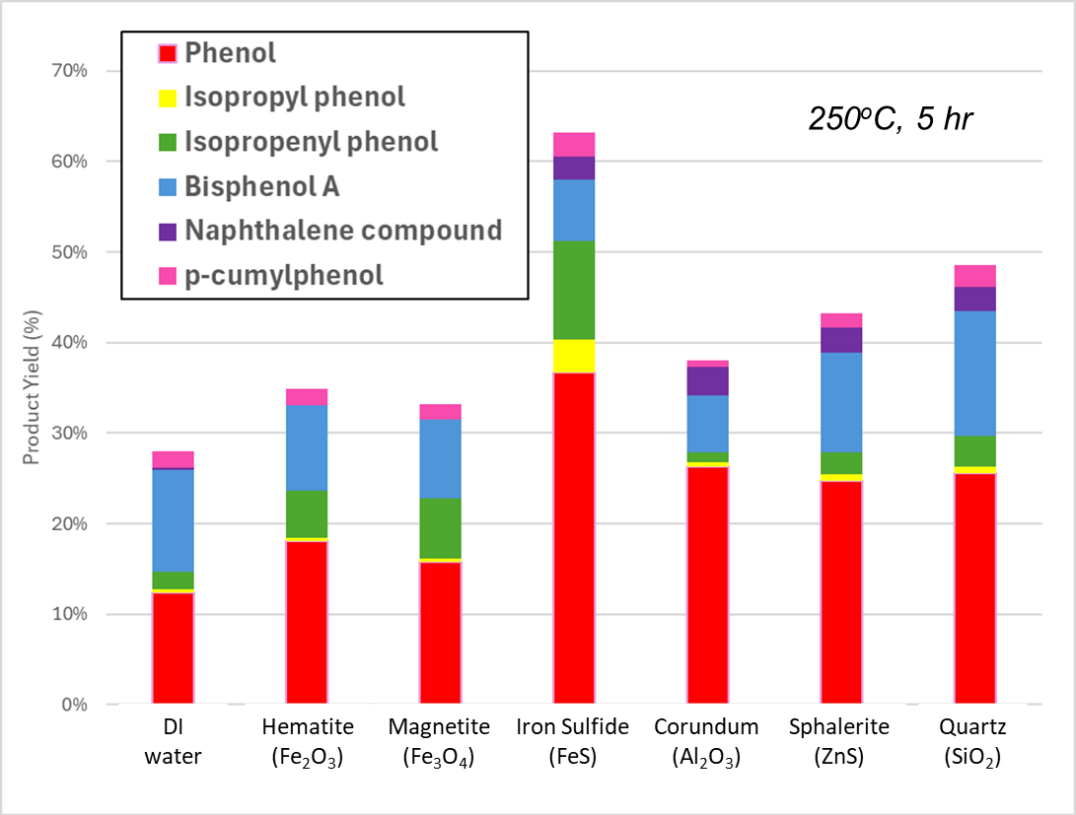

Figure 29. Effect of minerals on polycarbonate conversion (250°C, 5 hrs)

The effects of minerals on hydrothermal plastic degradation are not consistent among both types of polymers; the minerals seem to play a minor role in controlling the conversion of polystyrene, but a more noticeable role in polycarbonate degradation. This suggests that the minerals may be strong enough to facilitate the breaking of heteroatomic bonds such as in PC, but not the C-C bonds forming the backbone of PS. Further detailed studies will be necessary to determine the specific mechanisms for how minerals influence plastic degradation under hydrothermal conditions.

5.4 Conclusions

This work investigated the green and sustainable recycling of two types of plastics, including polystyrene and polycarbonate, which differ by their backbone structure. Polystyrene degradation depended significantly on the reaction temperature,

with relatively low yields of aromatic monomers, even after 7 days at 275^{o}C (~13%). Comparatively, polycarbonate degradation was much faster, with ~76% conversion after only 6 hrs at 250^{o}C, showcasing that reactivity is strongly affected by the polymer backbone. Structures with a C-C backbone (i.e. polystyrene, polypropylene, polyethylene) are more likely to require more energy to break the C-C bonds, while structures with a C-X backbone (i.e. polycarbonate, polyurethane, polyethylene terephthalate) are easier to degrade due to the presence of easily hydrolysable functional groups, which are weaker bonds than those between two carbons. The addition of minerals as Earth-abundant and nontoxic catalysts has been shown to enhance polycarbonate degradation (particularly the sulfides and quartz), while minimal effects were observed on polystyrene conversion. In general, this study highlights the green chemistry application of hydrothermal treatment in the recycling of polymeric waste. Further studies on other plastic types or mixtures of plastic waste will provide more advances in the field of sustainable chemistry.

CHAPTER SIX

CONCLUSIONS AND FUTURE PROSPECTS

6.1 Overview

The investigations detailed in this dissertation have shed light on the importance of organic geochemistry in varying applications, including prebiotic synthesis, extraterrestrial habitability, and green chemistry. Chapters 2 and 3 focused on identifying the reactions of alkenes and amino acids under geochemically relevant hydrothermal conditions, respectively, as well as determining how inorganic materials influence their pathways. Alkenes were observed to undergo three pathways, including hydration to alcohols, oxidation to aldehydes, and dimerization to larger and more complex alkenes (Aspin et al., 2023). Geochemical parameters such as solution pH and the presence of dissolved metal salts influenced the pathway distributions, with acidic conditions strongly promoting hydration and metal salts enhancing the dimerization pathway. Metal salts also promoted the hydration reaction, however, buffered metal experiments showed the change in solution pH induced by the dissolution of metal salts enhanced the reaction, while the metal ions themselves directly facilitated the dimerization of alkenes (Aspin et al., 2023). Amino acids were observed to decarboxylate to form amines, followed by deamination to form alcohols and/or alkenes. Amino acid reactivity was strongly influenced by reaction temperature, with higher temperatures favoring the decomposition of amino acids and lower temperatures favoring their stability. Geochemical parameters like solution pH and inorganic ion speciation also played a major role in controlling amino acid reactions in high-temperature environments. A relatively mid-pH range

promotes the degradation of amino acids, while extremely acidic and moderately basic pHs inhibit their conversion. Additionally, the presence of dissolved inorganic salts prevents the degradation of amino acids, increasing their survivability in solutions of high ionic strength. These two studies provide insights into prebiotic synthesis on early-Earth by investigating key intermediates and biomolecules necessary to form and sustain life.

Chapters 3 and 4 had implications for extraterrestrial habitability and the search for life beyond Earth. Hydrothermal experiments of amino acids showed their enhanced preservation in basic solutions and the presence of dissolved metal salts. These observations are relevant to Saturn's moon Enceladus, which is one of the prime astrobiology targets to study habitability, as the subsurface ocean is expected to be hydrothermally active, basic in pH (8-10; (Fifer et al., 2022), and high in ionic strength (<2 wt% Na- and K- chlorides/carbonates; (Postberg et al., 2011). The preservation of amino acids in relevant conditions may suggest these biomolecules could be preserved in Enceladus' ocean. Indeed, amino acids have been detected in the plume materials ejected from the icy surface (Khawaja et al., 2019; Postberg et al., 2018b). Future search-for life missions would like to better characterize the plume materials to determine if Enceladus' subsurface ocean is inhabited, but to do so would require inferring the abundances of biosignatures from what is analyzed in the plumes. Chapter 3 addresses this issue by comparing relative biosignature abundances that have been injected through the liquid-vacuum plume simulator to their distribution prior to injection. This study shows that the relative abundances did not change enough to prevent distinction between biological or abiotic sources of biosignatures in future search-for-life missions, suggesting measurements by spacecraft would be representative of what is in the subsurface ocean.

Finally, Chapter 5 investigated the application of hydrothermal treatment on two types of plastic waste, including polystyrene and polycarbonate, as a green and sustainable recycling method. The two types of plastics had different reactivity in hydrothermal conditions, which depended on their polymeric structure. Plastics with a C-C backbone are much more difficult to degrade, with a much lower conversion than plastics containing a C-O backbone. The addition of minerals as Earth-abundant and nontoxic catalysts facilitated the degradation of polycarbonate (up to twice the conversion compared to pure DI water experiments), while their influences were minimal on polystyrene degradation.

6.2 Future Work

One important theme of this dissertation is that inorganic materials can have an influence on organic transformations in high-temperature and high-pressure environments. While there are studies investigating the interaction between inorganics and organics in hydrothermal systems (Aspin et al., 2023; Fu et al., 2020a; Johnson-Finn et al., 2021; Liao et al., 2021; Yang et al., 2018), there are many studies focusing on hydrothermal transformations in pure water alone. These studies may provide useful data on pathway mechanisms, but they do not truly reflect natural hydrothermal systems, which are highly complex mixtures of various salts, organics, and mineral assemblages. Here, the pathways of one simple alkene and one simple amino acid were probed, in the presence of one metal salt at a time. Future work investigating the influence of complex fluids, whether that includes several dissolved metals concurrently, mineral assemblages with dissolved metals, or even multiple types of compounds, on organic transformations is essential to better characterize their occurrence in natural systems. Furthermore,

hydrothermal experiments on different alkene structures or amino acids would be important to gain a wider scope of their transformations.

The use of hydrothermal treatment in the field of "geomimicry" is a relatively new research avenue. In general, hydrothermal conditions have been used in biomass recycling (Alper et al., 2020; Fan et al., 2018), sewage sludge decontamination (Malhotra & Garg, 2020; Shi et al., 2013b), pollutant removal (Shi et al., 2013a), and plastic recycling (Seshasayee & Savage, 2021; Zhao et al., 2018b). The work in this dissertation sought to enhance the hydrothermal recycling of two individual plastics. However, studies also show a synergistic effect of reacting a mixture of plastic waste (Seshasayee & Savage, 2021), in which reactive intermediates from one type of plastic can possibly enhance the degradation of other plastics. Future work on the hydrothermal treatment of plastic mixtures with minerals may also be an important investigation to conduct. From an economic standpoint, this would enhance the recycling method efficiency, considering that the separation of plastics (which is important for primary and secondary recycling methods) would not be necessary. Furthermore, studies on the co-treatment of plastics with biomass waste also suggest a synergistic effect (Lu et al., 2020; Yao & Ma, 2018), in which the conversion of plastic is enhanced in the presence of biomass waste. Taken together, the synergistic effects observed during the co-hydrothermal treatment of plastic and biomass waste mixtures could make the treatment of municipal waste easier.

APPENDIX A

SUPPORTING INFORMATION FOR EXPERIMENTAL AND THEORETICAL INVESTIGATION OF ALKENE TRANSFORMATIONS IN OCEANIC HYDROTHERMAL FLUIDS: A MECHANISTIC STUDY OF STYRENE

Text A1

Styrene (99%), styrene oxide (97%), styrene glycol (97%), acetophenone (99%), benzaldehyde (99%), 1-phenylethanol (99%), and phenylacetaldehyde (95%) were purchased from Sigma-Aldrich. Metals salts including sodium chloride (99%), aluminum chloride (99%), copper(II) chloride (99%), zinc sulfate (monohydrate, 99%) were also obtained from Sigma-Aldrich, while iron(III) sulfate (pentahydrate, 97%) was obtained from Acros Organics, and zinc chloride (97%) and iron(III) chloride (anhydrous, 98%) were obtained from Alfa Aesar. Dichloromethane (DCM, 99%) was obtained from VWR and was used as the organic solvent for the extraction of reaction products. Decane (99%) was purchased from Sigma-Aldrich and used as the internal standard for gas-chromatography (GC) quantitative analysis. Deionized water (18.2 MΩ) was obtained from a Barnstead Nanopure system. Sodium phosphate monobasic (99%), sodium phosphate dibasic (99%), and phosphoric acid (99%) were purchased from Sigma-Aldrich and used for the pH-buffered experiments. The PBS solutions were prepared with proportions of phosphoric acid, sodium phosphate monobasic and dibasic to reach the desired pH, at least three times the initial concentration of styrene to ensure a sufficient pH buffering capacity, following previously established methods (Robinson et al., 2019; Robinson et al., 2021b).

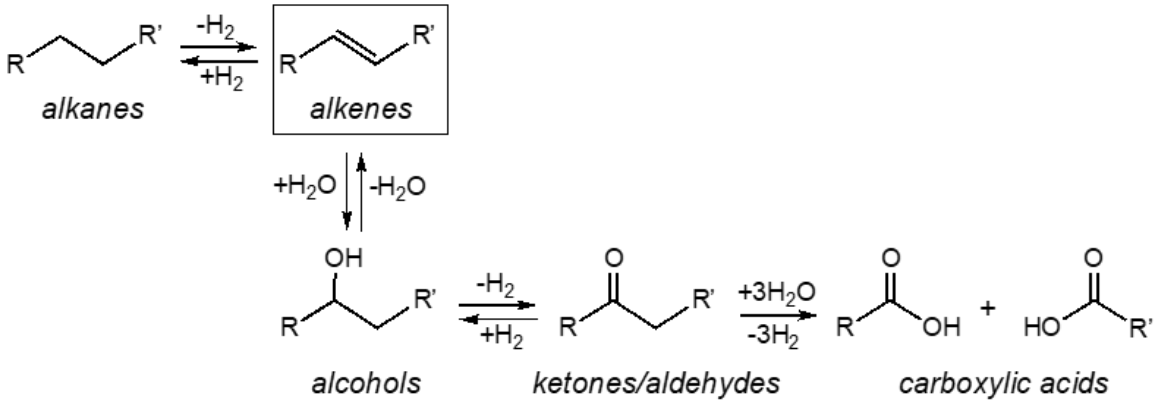

Figure A1. Organic functional group interconversions in oceanic hydrothermal systems (After Seewald, 2003).

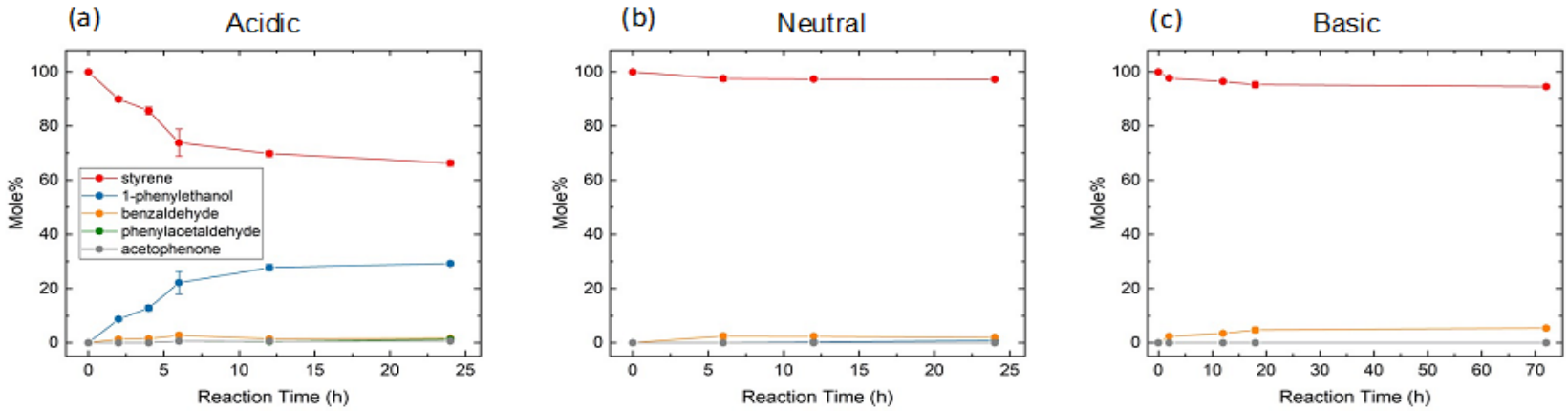

Figure A2. Hydrothermal reactivity and reaction products of styrene at acidic (pH 3), near neutral (pH 5.8), and basic (pH 7.8) conditions. pH values are calculated at hydrothermal conditions at 150°C and P_{sat} with PBS buffers. The mole% are calculated based on all the observed major products and the remaining styrene, assuming a 100% mass balance (Taken from Aspin et al., 2023).

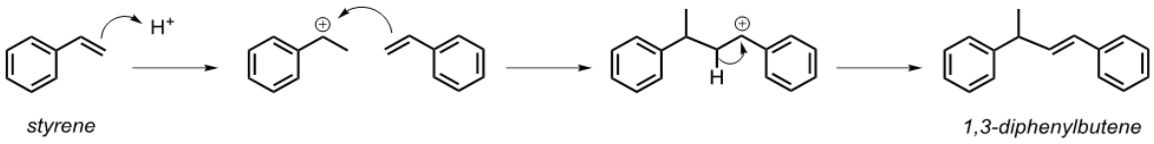

Figure A3. Proposed mechanism for dimerization of styrene under hydrothermal conditions (Taken from Aspin et al., 2023).

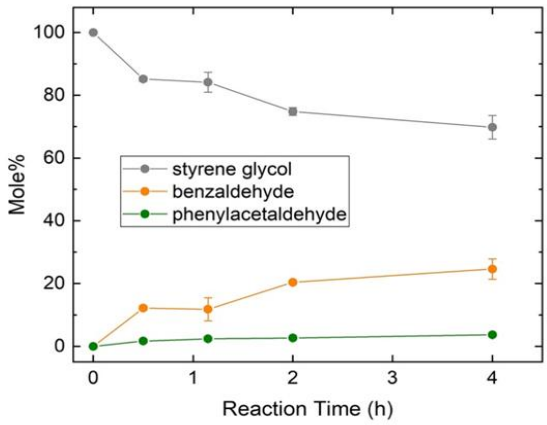

Figure A4. Product distribution (as mole%) of hydrothermal reaction of styrene glycol (0.1 molal) as a function of reaction time at 150^{o}C and P_{sat}. The mole% are calculated based on all the observed major products and the remaining styrene, assuming a 100% mass balance (Taken from Aspin et al., 2023).

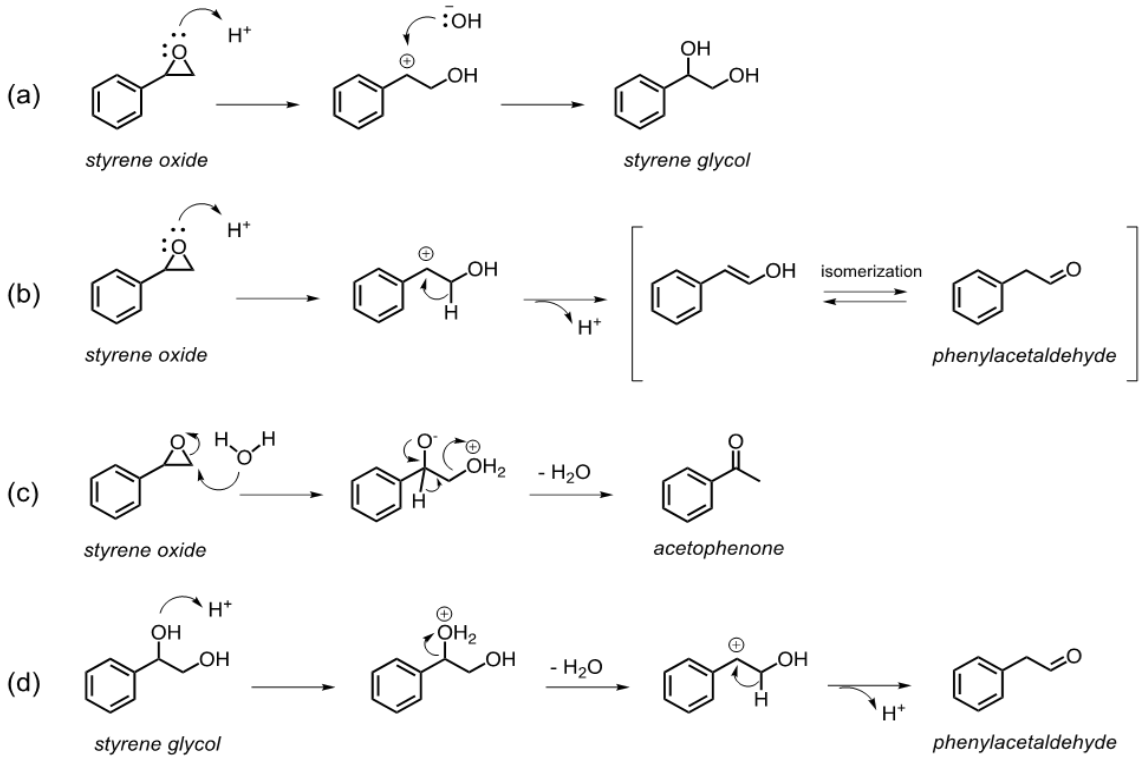

Figure A5. Proposed mechanisms for reactions from styrene oxide to styrene glycol (a), phenylacetaldehyde (b), and acetophenone (c), as well as for the reaction from styrene glycol to phenylacetaldehyde (d) under hydrothermal conditions (Taken from Aspin et al., 2023).

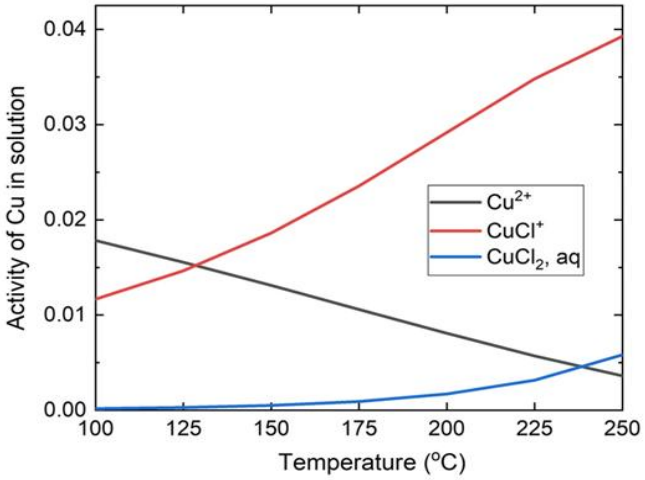

Figure A6. Distribution of the major aqueous copper species (shown as activity in solution) for 0.1 molal $CuCl_2$ as a function of temperature at pH 4.5 (Taken from Aspin et al., 2023).

Table A1.

Hydrothermal reactions of styrene in acidic (pH 3), near neutral (pH 5.8), and basic (pH 7.8) solutions with PBS buffer at 150°C and P_{sat}. The mole% are calculated based on all the observed major products and the remaining styrene, assuming a 100% mass balance. Mass balances less than 100% could be due to the loss of products during extraction or minor unquantified products that are below the detection limit of GC (Taken from Aspin et al., 2023).

Reaction condition	**Styrene (mole%)**	**1-phenyl-ethanol (mole%)**	**Benzald-ehyde (mole%)**	**Phenyl-acetaldehyde (mole%)**	**Acetophen-one (mole%)**	**Mass Balance (%)**
Acidic, 2 h	89.9±0.8	8.7±0.7	1.3±0.1	<0.1	<0.1	97.3±2.1
Acidic, 4 h	85.7±1.4	12.8±1.1	1.5±0.3	<0.1	<0.1	89.7±5.2
Acidic, 6 h	73.8±4.9	22.1±4.2	2.7±0.6	0.6±0.2	0.6±0.1	84.1±9.3
Acidic, 12 h	69.8±1.2	27.8±1.2	1.4±0.1	0.4±0.1	0.5±0.1	83.1±3.9
Acidic, 24 h	66.3±1.1	29.3±0.8	1.6±0.2	1.2±0.1	0.6±0.1	81.3±5.9
Neutral, 6 h	97.5±1.0	<0.1	2.5±1.0	<0.1	<0.1	89.1±2.1
Neutral, 12 h	97.4±0.4	0.3±0.1	2.4±0.4	<0.1	<0.1	85.4±3.4
Neutral, 24 h	97.2±0.1	0.8±0.1	1.9±0.1	<0.1	<0.1	86.9±7.6
Basic, 2 h	97.7±0.1	<0.1	2.3±0.1	<0.1	<0.1	92.0±3.1
Basic, 12 h	96.4±0.1	<0.1	3.5±0.1	<0.1	<0.1	89.2±2.2
Basic, 18 h	95.3±1.1	<0.1	4.7±1.1	<0.1	<0.1	86.0±0.9
Basic, 72 h	94.5±0.1	<0.1	5.4±0.1	<0.1	<0.1	82.5±3.7

Table A2.

Hydrothermal reactions of styrene with metal salts in pH-buffered (pH 3) and unbuffered solutions at 150°C and P_{sat} after 24 h. The pathway% are calculated based on the products formed in each pathway among all the products and the remaining styrene after the reaction. Mass balances less than 100% could be due to the loss of products during extraction or minor unquantified products that are below the detection limit of GC (Taken from Aspin et al., 2023).

Reaction Conditions	**Unreacted styrene (%)**	**Hydration pathway (%)**	**Oxidation pathway (%)**	**Dimerization pathway (%)**	**Mass balance (%)**
H_2O, unbuffered	89.9±2.1	8.4±0.4	1.6±0.6	<0.1	92.3±3.9
$ZnCl_2$, unbuffered	79.3±1.3	15.7±0.7	5.0±0.7	<0.1	87.2±4.8
$ZnSO_4$, unbuffered	87.7±2.8	7.3±0.4	4.9±0.3	<0.1	90.3±3.4
$CuCl_2$, unbuffered	60.1±1.5	26.1±1.2	6.6±0.8	7.2±0.5	82.6±7.6
$CuSO_4$, unbuffered	61.6±7.6	28.3±3.2	8.9±4.0	1.1±0.4	77.2±10.2
$AlCl_3$, unbuffered	70.7±0.8	16.8±0.3	2.6±0.3	9.8±0.7	85.4±2.8
$Al_2(SO_4)_3$, unbuffered	60.2±2.9	26.6±0.8	2.7±0.4	10.5±2.5	82.3±6.1
$Fe_2(SO_4)_3$, unbuffered	50.4±7.1	11.4±0.3	7.9±1.6	30.2±8.4	76.7±15.3
$FeCl_3$, unbuffered	43.5±4.3	7.6±0.4	9.5±0.1	39.5±4.7	80.5±9.2
H_2O, buffered	66.3±1.1	29.3±0.8	3.5±0.3	0.9±0.1	81.3±5.9
NaCl, buffered	72.6±2.4	22.7±0.8	2.5±0.2	1.7±0.9	87.3±2.7
$ZnCl_2$, buffered	58.8±3.8	36.9±2.8	2.4±0.2	1.9±0.8	83.9±7.3
$CuCl_2$, buffered	61.5±2.2	25.8±0.6	3.6±0.1	9.1±2.7	86.2±5.3
$AlCl_3$, buffered	61.0±1.1	14.1±0.2	3.8±0.2	21.0±0.7	78.7±8.8
$FeCl_3$, buffered	57.1±4.5	13.8±0.6	4.6±0.1	24.5±3.9	77.4±7.3

Table A3.

The pH of the metal salt solutions measured at room temperature and their relative acidity. The total concentrations of metal ions in each salt solution are all 0.1 molal (Taken from Aspin et al., 2023).

Metal salt solution	**pH**	**Relative acidity (low to high)**
$ZnCl_2$	5.7	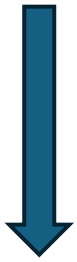
$ZnSO_4$	5.3	
$CuCl_2$	4.1	
$CuSO_4$	3.8	
$AlCl_3$	3.5	
$Al_2(SO_4)_3$	3.1	
$Fe_2(SO_4)_3$	2.0	
$FeCl_3$	1.7	

APPENDIX B

SUPPORTING INFORMATION FOR SURVIVABILITY AND PATHWAYS OF AMINO ACIDS IN OCEANIC HYDROTHERMAL SYSTEMS: A MECHANISTIC STUDY OF PHENYLALANINE

Text B1. Materials

DL-Phenylalanine (99%) was obtained from Sigma-Aldrich. Styrene (99%), 2-phenylethylamine (≥99%), benzaldehyde (99%), 1-phenylethanol (99%), 2-phenylethanol (≥99%), benzyl alcohol (99%), and benzylamine (99%) were also purchased from Sigma-Aldrich. Dichloromethane (DCM, 99%) was obtained from VWR and used as the organic solvent to extract the reaction products. Decane (≥99%) was purchased from Sigma-Aldrich and used as the internal standard for quantitative analysis on gas chromatography (GC). Phenol (>99%) was also purchased from Sigma-Aldrich and used as the internal standard for phenylalanine quantification on high-performance liquid chromatography (HPLC). Deionized (DI) water (18.2 MΩ) was obtained from a Barnstead Nanopure system. Sodium hydroxide (NaOH, 98%) and hydrochloric acid (HCl, 50wt%) were purchased from Sigma-Aldrich and used for the pH experiments. Metals salts including sodium chloride (99%), aluminum chloride (99%), copper(II) chloride (99%), iron(II) chloride (anhydrous, 99.5%) magnesium chloride (≥98%), and copper sulfate (pentahydrate, 98%) were also obtained from Sigma-Aldrich, while iron(III) chloride (anhydrous, 98%) was obtained from Alfa Aesar.

Table B1.

Measured pH at benchtop (room temperature) and calculated in-situ pH (at the experimental condition of 275°C and 59.5 bar) in the phenylalanine solutions (Taken after Aspin et al., submitted).

Benchtop pH	**In-situ pH**	**Expected form of phenylalanine in-situ**
1.2	1.3	cationic
2.7	2.7	zwitterionic
3.5	3.5	zwitterionic
4.5	4.5	zwitterionic
5.6	5.4	zwitterionic
9.2	6.4	anionic
11.3	8.5	anionic

Table B2.

Calculated rate constants and half-lives for phenylalanine hydrothermal degradation in this and the previous studies (Taken after Aspin et al., submitted).

Temperature (°C)	**Rate constant (k, h^{-1})**	**Half-life (hrs)**	**Source**
220	0.09	7.7	Changi et al. (2012)
230	0.17	3.9	Abdelmoez et al. (2010)
250	0.08	8.2	Vallentyne (1964)
250	0.50	1.4	Changi et al. (2012)
250	0.55	1.3	Abdelmoez et al. (2010)
250	0.57	1.2	Li and Brill (2003)
260	0.96	0.7	Abdelmoez et al. (2010)
280	4.15	0.2	Changi et al. (2012)
290	4.20	0.2	Abdelmoez et al. (2010)
225	0.13	5.3	this work
250	0.29	2.4	this work
275	0.42	1.6	this work

Table B3.

Conversion of 2-phenylethylamine (0.07 molal) and the production of styrene and 2-phenylethanol under different hydrothermal conditions (Taken after Aspin et al., submitted).

Temperature (ºC)	**Reaction time (hrs)**	**2-phenylethylamine conversion (%)**	**styrene (mmolal)**	**2-phenylethanol (mmolal)**
175	24	3.7±1.3	0.7±0.3	1.0±0.1
175	120	8.3±0.4	3.9±0.1	1.9±0.2
225	6	25.3±4.8	5.9±2.8	<0.1
275	2	21.7±0.2	13.5±0.3	<0.1
275	6	40.6±0.9	25.7±0.9	0.4±0.1

Table B4.

Calculated in-situ pH, ionic strength, and observed total degradation aromatic products (after 6 hrs) in phenylalanine (0.07 molal) hydrothermal experiments with dissolved metal salts (0.05 – 1.0 molal) at 275ºC and 59.5 bar (P_{sat}) (Taken after Aspin et al., submitted).

Metal Salt	**In-situ pH**	**Ionic strength (mmolal)**	**Total aromatic products (mmolal)**
None (DI)	5.4	0	36.4±2.5
$AlCl_3$ (0.05 molal)	1.5	237	16.4±0.3
$FeCl_3$ (0.05 molal)	1.6	164	35.5±1.4
$CuCl_2$ (0.05 molal)	2.5	69	20.4±2.9
$FeCl_2$ (0.05 molal)	3.8	87	42.6±1.4
$MgCl_2$ (0.05 molal)	4.3	106	27.9±0.4
$CuSO_4$ (0.05 molal)	4.7	111	14.7±0.1
NaCl (0.1 molal)	5.4	86	39.0±0.6
NaCl (0.2 molal)	5.4	160	28.9±0.8
NaCl (0.4 molal)	5.4	299	21.7±0.4
NaCl (0.7 molal)	5.4	484	26.1±0.3
NaCl (1.0 molal)	5.4	653	28.2±2.7

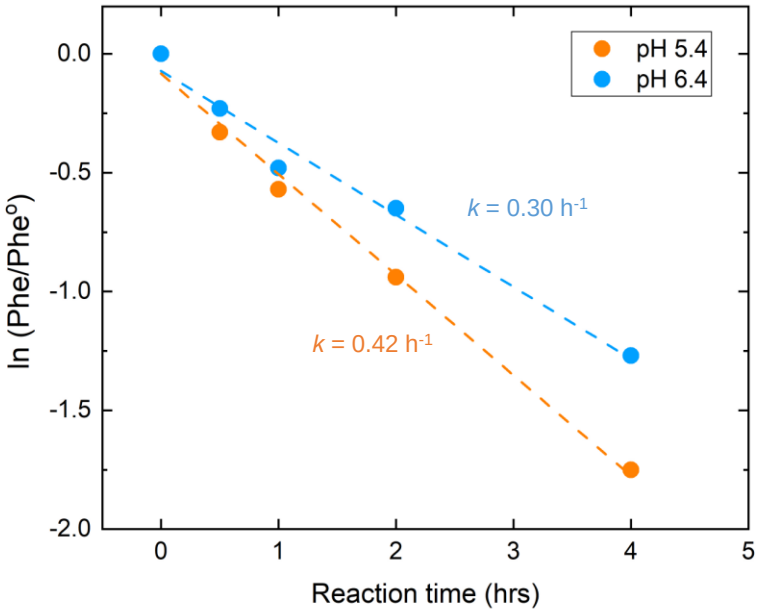

Figure B1. Degradation kinetics and calculated rate constants of phenylalanine at in-situ pH of 5.4 and 6.4 at 275°C and 59.5 bar (P_{sat}). Data are best fitted with a pseudo first-order kinetics with respect to the phenylalanine concentration (Taken after Aspin et al., submitted).

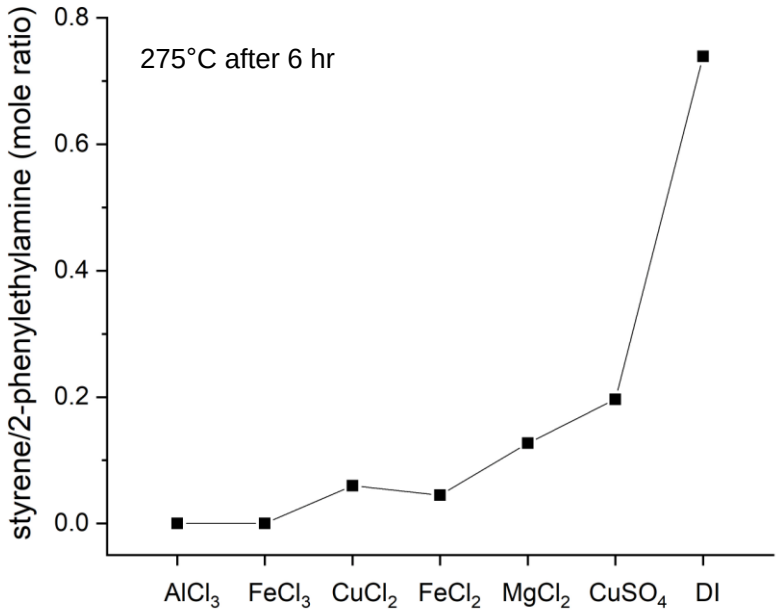

Figure B2. Relative concentration ratios between styrene and 2-phenylethylamine as an indicator for the relative distribution of deamination and decarboxylation pathways for phenylalanine in the presence of metal salts at 275ºC and P_{sat} after 6 hrs (Taken after Aspin et al., submitted).

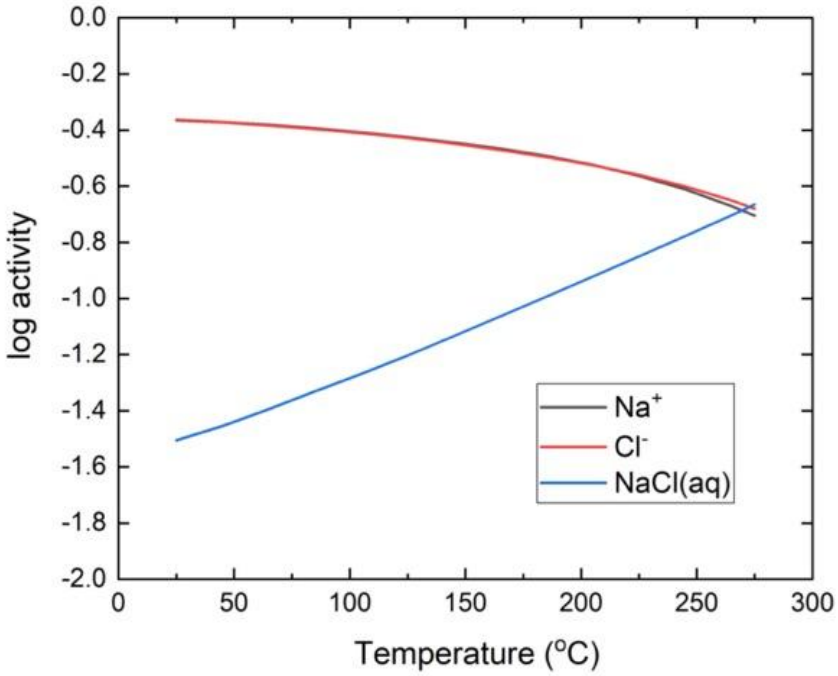

Figure B3. Calculated activities of Na^+, Cl^-, and $NaCl_{(aq)}$ in a 0.1 molal NaCl solution as a function of temperature (Taken after Aspin et al., submitted).

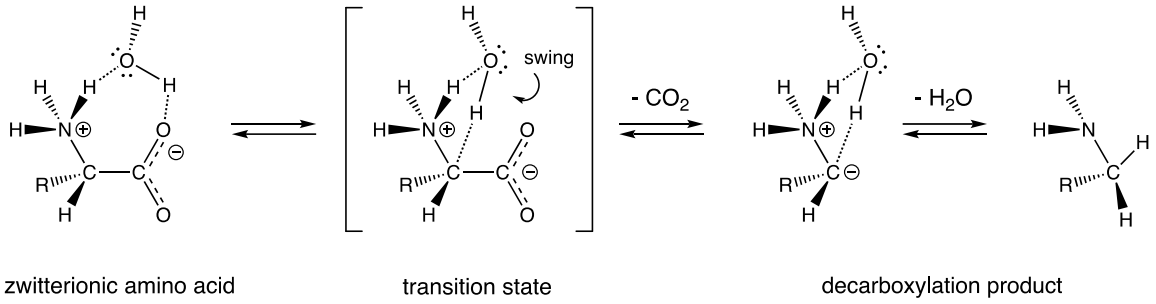

Figure B4. Proposed stabilization of zwitterionic amino acid via hydrogen bonding and transition state for the decarboxylation mechanism (modified from Li & Brill, 2003).

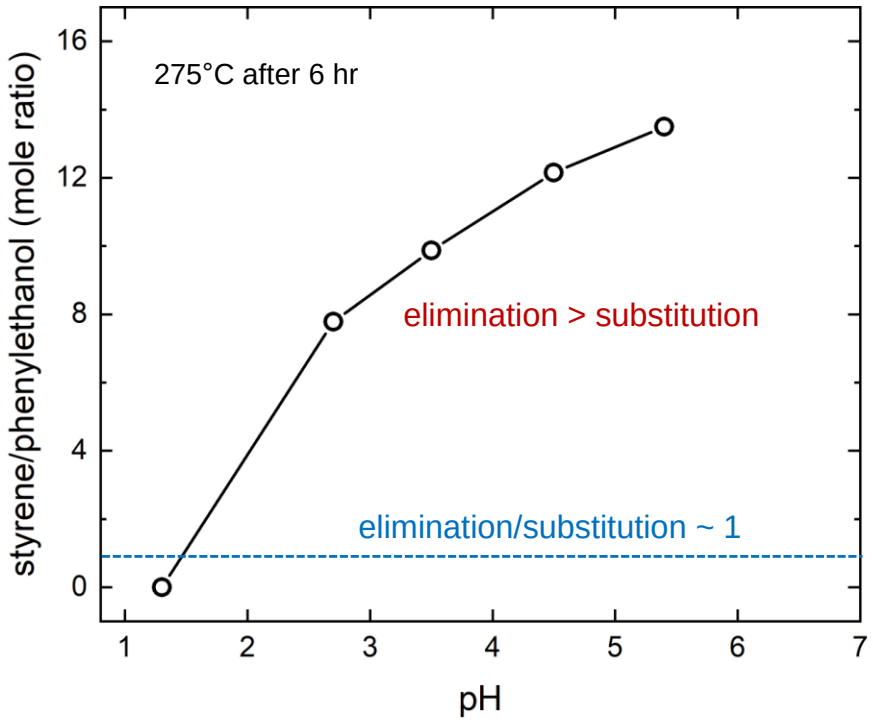

Figure B5. Relative ratios between elimination deamination and substitution deamination as a function of pH, plotted using the concentration ratio between styrene and phenylethanol (Taken after Aspin et al., submitted).

APPENDIX C

SUPPORTING INFORMATION FOR EFFECT OF THE LIQUID-VACUUM TRANSITION ON THE RELATIVE ABUNDANCES OF AMINO AND FATTY ACIDS SOUGHT AS BIOSIGNATURES ON ICY OCEAN WORLDS

Text C1. Velocity and freezing rate of the fluid and grains

The speed of the fluid and grains in the sub-P_t sections of the injection line, v_{fluid}, was likely on the order of 10 m s^{-1}. Below, we provide estimates and constraints on this velocity using different methods. First, the flow velocity was greater than $\sim (g \times l)^{0.5} \approx 1$ m s^{-1} because the material sprayed the center of the collection cup at a distance $l \approx 5$–15 cm from the end of the port at the chamber edge, rather than falling to the bottom of the chamber due to Earth's gravitational acceleration g.

Second, we think that the grain velocity was not much greater than 1 m s^{-1}, because grains did not bounce off of the cup or visibly pit its soft aluminum surface. In vacuum, 10–100 µm particles bounce only for impact speeds > 0.1–1 m s^{-1} (Arakawa & Krijt, 2021; Fritscher & Teiser, 2021; Musiolik et al., 2016; Nietiadi et al., 2020). Higher velocities are possible for smaller (Miller et al., 2022) and/or partially frozen, stickier particles, which may have been the case in our experiments.

Third, we did not observe water (liquid or ice) in grains during injection, except a few instances of > mm-sized, partially frozen material that volatilized within ~1 second. Frozen grains may have been too small to be visible (< 0.1 mm), the freezing time scale discussed in Section 4.2.1 of the main text indicates a corresponding transport time of $\leq$ 0.005 s. Since transport takes place through the ≈ 20–30 cm distance between the valves and collection cup (see Figure 15a of the main text), a corresponding lower bound on v_{fluid} is 40 m s^{-1}.

Finally, we witnessed impacting sub-mm grains on the cup temporarily tilting its foil support by $d_{tilt} \sim 1$ cm (Supplementary video), and reproduced this tilt by placing a test mass $m_{test} = 8$ grams on a horizontal foil sheet. By equating $m_{test}\, g \approx m_{grain}\, v_{fluid}^2/d_{tilt}$,

with v_{fluid}^2/d_{tilt} the approximate grain deceleration to zero velocity, we find $v_{fluid} \approx (d_{tilt}\ m_{test}\ g\ /\ m_{grain})^{0.5}$ = 14 m s^{-1} for a 1 mm-radius ice grain. These ~10 m s^{-1} velocities are similar to those modeled for most of the length of subsurface conduits with pressure below Pt on Enceladus (Nakajima & Ingersoll, 2016).

Text C2. Figure 18 caption continued

Notes: In (a), example biological aa/Gly are the average of data from (Nishikawa & Ooi, 1982) for 356 proteins with molecular mass > 5000 Da from prokaryotes and eukaryotes, and from (Lobry & Gautier, 1994) for E. coli; both datasets have very similar values. Uncertainties are the square root of the sum of the two squared uncertainties, divided by √2. Abiotic aa/Gly are the average of (total hydrolyzed amino acid)/(total hydrolyzed Gly) in up to eleven measurements: Ryugu samples A0106 (one measurement from (Naraoka et al., 2023); one from (Parker et al., 2023) and C0107 (Parker et al., 2023); CM chondrites Winchcombe (Chan et al., 2024) and Asuka 12236 (Glavin et al., 2020); and CR chondrites GRO 95577, EET 92042, and QUE99177 (Glavin et al., 2010), MIL 090001 and MIL 090657 (Aponte et al., 2020), and GRA 95229 (Martins et al., 2007). Abundances for which the L-enantiomer was more abundant than the D-enantiomer above 1 sigma were ignored to screen out potential terrestrial contamination. Uncertainties are standard errors among the samples for which aa/Gly was reported and had no such L-excess; uncertainties reported for individual measurements were not propagated.

Table C1.

Fraction of the mass of compound recovered in various sections of the injection path. Uncertainties are 1 standard deviation across three 200 mL solution replicates (amino acid injection) or the standard deviation, unweighted by volume, across two 280-mL and 470-mL replicates of the fatty acid solution. [a]Only one replicate; for the other, the phenylacetic acid signal was below the GC limit of detection (Taken from Neveu et al., 2024a).

Compounds	**Mass of recovered dry residue (% of total injected mass, ± 1 standard deviation)**			
	Valves	**Flange**	**Port**	**Chamber**
Gly	12.3±8.1	24.2±4.8	63.2±10.9	9.1±1.1
Ala	12.2±8.2	26.5±6.5	63.6±16.8	8.4±3.6
Glu	9.8±6.1	22.1±5.5	49.2±10.3	8.6±1.4
Asp	7.7±4.5	16.0±3.8	36.2±8.3	6.1±1.3
Leu	13.1±7.9	22.1±5.4	50.9±12.4	7.3±3.9
Thr	13.4±9.2	29.7±6.5	71.3±17.6	7.3±0.5
AIB	8.7±5.8	15.7±3.1	36.2±6.3	6.2±1.1
γAB	10.0±6.7	20.8±4.2	47.3±10.5	7.8±1.8
His	8.1±2.5	21.5±6.4	47.8±8.6	10.1±1.4
Phe	19.4±1.2	23.7±6.9	52.1±8.0	12.4±2.5
Tyr	11.0±4.3	15.6±5.1	29.8±8.0	6.0±1.7
Trp	7.4±5.6	16.2±5.2	32.6±7.4	4.0±0.9
Phenylacetic acid	0.86[a]	10.2±0.4	62.1±3.2	6.6±1.1
Palmitic acid	0.95[a]	2.86±0.04	5.20±0.01	0.92±0.01

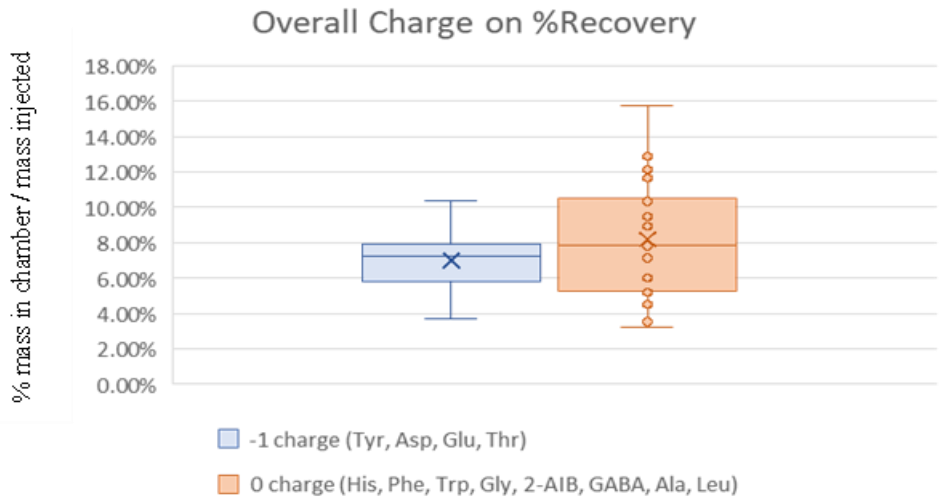

Figure C1. Effect of overall charge of amino acids on the mass fraction of amino acids recovered in the chamber (% of injected mass). The predominant form of Tyr, Asp, Glu, and Thr had an overall charge of -1, while the others were electrically neutral (Taken from Neveu et al., 2024a).

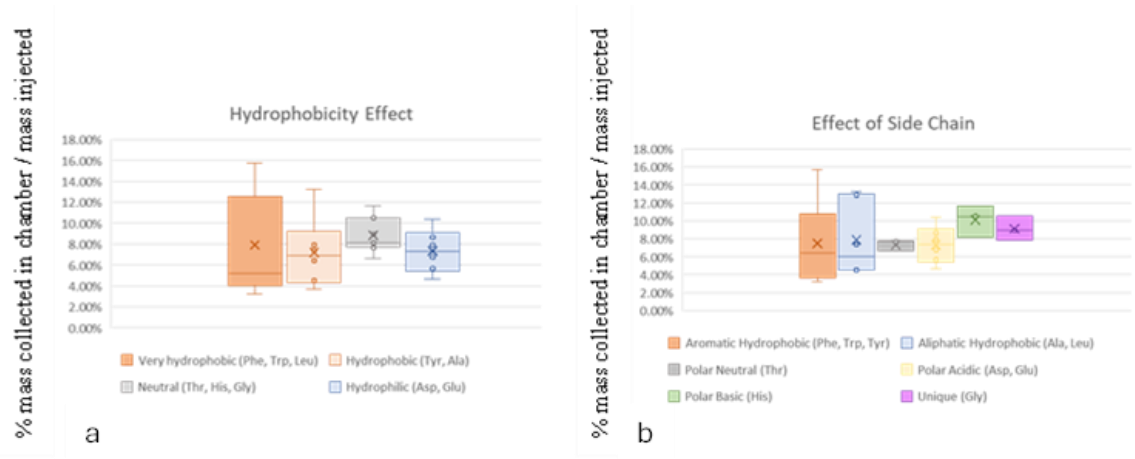

Figure C2. Effect of hydrophobicity (a) and side chain functionality (b) of amino acids on the mass fraction in the collection chamber (as % of injected mass) after simulated plume injection. Four of the amino acids are aromatic, including Phe, Tyr, Trp, and His, which contain either six- or five-membered rings. Phe and Tyr are quite similar in their structures, with a short carbon chain attached to a benzene ring (Phe) or to the para-position of a benzenol (Tyr). Trp is the largest aromatic acid, which contains an indole group as the side chain. Because these aromatic side chains are relatively bulky and nonpolar, Phe, Tyr, and Trp are classified under the aromatic hydrophobic category for comparison with other amino acids (Figure C2). His, on the other hand, although aromatic with an imidazole group in the side chain, is considered a polar-basic amino acid because the imidazole group is readily protonated in solutions. For non-aromatic structures, Ala and Leu are categorized as aliphatic-hydrophobic because their side chains contain only aliphatic hydrocarbons and are hydrophobic in nature. Asp and Glu both have a carboxyl group in their side chain, which is expected to deprotonate at the pH of injected solutions, making them polar-acidic. The side chain of Thr consists of a short hydrocarbon with an alcohol group attached, which is relatively polar but neutral at the experimental conditions; so Thr is considered polar neutral. As a reference, Gly is given its own unique category due to its simplest structure (Taken from Neveu et al., 2024a).

REFERENCES

Abdelmoez, W., Nakahasi, T., & Yoshida, H. (2007). Amino acid transformation and decomposition in saturated subcritical water conditions. *Industrial & Engineering Chemistry Research*, *46*(16), 5286–5294. https://doi.org/10.1021/ie070151b

Abdelmoez, W., Yoshida, H., & Nakahasi, T. (2010). Pathways of amino acid transformation and decomposition in saturated subcritical water conditions. *International Journal of Chemical Reactor Engineering*, *8*(1). https://doi.org/10.2202/1542-6580.1903

Ahmed, M., Namboodiri, V., Singh, A. K., & Mondal, J. A. (2014). On the intermolecular vibrational coupling, hydrogen bonding, and librational freedom of water in the hydration shell of mono- and bivalent anions. *The Journal of Chemical Physics*, *141*(16), 164708. https://doi.org/10.1063/1.4899070

Akerlof, G. C., & Oshry, H. I. (1950). The dielectric constant of water at high temperatures and in equilibrium with its vapor. *Journal of the American Chemical Society*, *72*(7), 2844–2847. https://doi.org/10.1021/ja01163a006

Akiya, N., & Savage, P. E. (2002). Roles of water for chemical reactions in high-temperature water. *Chemical Reviews*, *102*(8), 2725–2750. https://doi.org/10.1021/cr000668w

Alherbawi, M., Parthasarathy, P., Al-Ansari, T., Mackey, H., & McKay, G. (2021). Potential of drop-in biofuel production from camel manure by hydrothermal liquefaction and biocrude upgrading: A Qatar case study. *Energy*, *232*.

Allen, D. E., & Seyfried, W. E. (2003). Compositional controls on vent fluids from ultramafic-hosted hydrothermal systems at mid-ocean ridges: An experimental study at 400°C, 500 bars. *Geochimica et Cosmochimica Acta*, *67*(8), 1531–1542. https://doi.org/10.1016/S0016-7037(02)01173-0

Alper, K., Tekin, K., Karagoz, S., & Ragauskas, A. (2020). Sustainable energy and fuels from biomass: A review focusing on hydrothermal biomass processing. *Sustainable Energy and Fuels*, *4*(9).

Al-Salem, S. M., Antelava, A., Constantinou, A., Manos, G., & Dutta, A. (2017). A review on thermal and catalytic pyrolysis of plastic solid waste (PSW). *Journal of Environmental Management*, *197*, 177–198. https://doi.org/10.1016/j.jenvman.2017.03.084

Amaya-Garcia, F., Caldera, M., Koren, A., Kubicek, S., Menche, J., & Unterlass, M. (2021). Green hydrothermal synthesis of fluorescent 2,3-diarylquinoxalines and large-scale computational comparison to existing alternatives. *ChemSusChem, 14*(8).

Amend, J. P., McCollom, T. M., Hentscher, M., & Bach, W. (2011). Catabolic and anabolic energy for chemolithoautotrophs in deep-sea hydrothermal systems hosted in different rock types. *Geochimica et Cosmochimica Acta, 75*(19), 5736–5748. https://doi.org/10.1016/j.gca.2011.07.041

Amend, J. P., & Shock, E. L. (1998). Energetics of Amino Acid Synthesis in Hydrothermal Ecosystems. *Science, 281*(5383), 1659–1662. https://doi.org/10.1126/science.281.5383.1659

Aponte, J. C., Elsila, J. E., Hein, J. E., Dworkin, J. P., Glavin, D. P., McLain, H. L., Parker, E. T., Cao, T., Berger, E. L., & Burton, A. S. (2020). Analysis of amino acids, hydroxy acids, and amines in CR chondrites. *Meteoritics & Planetary Science*, *55*(11), 2422–2439. https://doi.org/10.1111/maps.13586

Arakawa, S., & Krijt, S. (2021). On the stickiness of CO_2 and H_2O ice particles. *The Astrophysical Journal*, *910*(2), 130. https://doi.org/10.3847/1538-4357/abe61d

Aranovich, L. Y., & Newton, R. C. (1996). H_2O activity in concentrated NaCl solutions at high pressures and temperatures measured by the brucite-periclase equilibrium. *Contributions to Mineralogy and Petrology*, *125*(2), 200–212. https://doi.org/10.1007/s004100050216

Aspin, A., Ellis, R., Stull, M., & Yang, Z. (2025). Survivability and pathways of amino acids in oceanic hydrothermal systems: A mechanistic study of phenylalanine. *under review*

Aspin, A., Smith, B., Burcar, E., Firestone, Z., & Yang, Z. (2023). Experimental and theoretical investigation of alkene transformations in oceanic hydrothermal fluids: A mechanistic study of styrene. *Geophysical Research Letters*, *50*(16), e2023GL103738. https://doi.org/10.1029/2023GL103738

Bada, J., & Miller, S. (1970). Kinetics and mechanism of the reversible nonenzymic deamination of aspartic acid. *Journal of the American Chemical Society*. *92*(9), 2774–2782.

Bai, B., Jin, H., Fan, C., Cao, C., Wei, W., & Cao, W. (2019). Experimental investigation on liquefaction of plastic waste to oil in supercritical water. *Waste Management*, *89*, 247–253. https://doi.org/10.1016/j.wasman.2019.04.017

Barge, L. M., Flores, E., Baum, M. M., VanderVelde, D. G., & Russell, M. J. (2019). Redox and pH gradients drive amino acid synthesis in iron oxyhydroxide mineral systems. *Proceedings of the National Academy of Sciences, 116*(11), 4828. https://doi.org/10.1073/pnas.1812098116

Barge, L. M., & White, L. M. (2017). Experimentally testing hydrothermal vent origin of life on Enceladus and other icy/ocean worlds. *Astrobiology, 17*(9), 820–833. https://doi.org/10.1089/ast.2016.1633

Baross, J. A., & Hoffman, S. E. (1985). Submarine hydrothermal vents and associated gradient environments as sites for the origin and evolution of life. *Origins of Life and Evolution of the Biosphere*, *15*(4), 327–345. https://doi.org/10.1007/BF01808177

Batra, M. S., Dwivedi, R., & Prasad, R. (2019). Recent developments in heterogeneous catalyzed epoxidation of styrene to styrene oxide. *ChemistrySelect*, *4*(40), 11636–11673. https://doi.org/10.1002/slct.201902396

Baumgartner, B., Svirkova, A., Bintinger, J., Hametner, C., Marchetti-Deschmann, M., & Unterlass, M. (2017). Green and highly efficient synthesis of perylene and naphthalene bisimides in nothing but water. In *Chemical Communications* (Issue 7).

Beller, M., Seayad, J., Tillack, A., & Jiao, H. (2004). Catalytic markovnikov and anti-markovnikov functionalization of alkenes and alkynes: Recent developments and trends. *Angewandte Chemie International Edition*, *43*(26), 3368–3398. https://doi.org/10.1002/anie.200300616

Bennett, S. A., Achterberg, E. P., Connelly, D. P., Statham, P. J., Fones, G. R., & German, C. R. (2008). The distribution and stabilisation of dissolved Fe in deep-sea hydrothermal plumes. *Earth and Planetary Science Letters*, *270*(3), 157–167. https://doi.org/10.1016/j.epsl.2008.01.048

Bergmann, M., Mützel, S., Primpke, S., Tekman, M. B., Trachsel, J., & Gerdts, G. (2019). White and wonderful? Microplastics prevail in snow from the Alps to the Arctic. *Science Advances*, *5*(8), eaax1157. https://doi.org/10.1126/sciadv.aax1157

Bläsing, M., & Amelung, W. (2018). Plastics in soil: Analytical methods and possible sources. *Science of The Total Environment*, *612*, 422–435. https://doi.org/10.1016/j.scitotenv.2017.08.086

Bockisch, C., Lorance, E. D., Hartnett, H. E., Shock, E. L., & Gould, I. R. (2018). Kinetics and mechanisms of dehydration of secondary alcohols under hydrothermal conditions. *ACS Earth and Space Chemistry*, *2*(8), 821–832. https://doi.org/10.1021/acsearthspacechem.8b00030

Bockisch, C., Lorance, E. D., Shaver, G., Williams, L. B., Hartnett, H. E., Shock, E. L., & Gould, I. R. (2019). Selective hydrothermal reductions using geomimicry. *Green Chemistry, 21*(15), 4159–4168. https://doi.org/10.1039/C9GC00636B

Borrelle, S. B., Ringma, J., Law, K. L., Monnahan, C. C., Lebreton, L., McGivern, A., Murphy, E., Jambeck, J., Leonard, G. H., Hilleary, M. A., Eriksen, M., Possingham, H. P., De Frond, H., Gerber, L. R., Polidoro, B., Tahir, A., Bernard, M., Mallos, N., Barnes, M., & Rochman, C. M. (2020). Predicted growth in plastic waste exceeds efforts to mitigate plastic pollution. *Science*, *369*(6510), 1515–1518. https://doi.org/10.1126/science.aba3656

Bouquet, A., Glein, C. R., & Waite, J. H. (2019). How adsorption affects the gas–ice partitioning of organics erupted from Enceladus. *The Astrophysical Journal*, *873*(1), 28. https://doi.org/10.3847/1538-4357/ab0100

Brahney, J., Hallerud, M., Heim, E., Hahnenberger, M., & Sukumaran, S. (2020). Plastic rain in protected areas of the United States. *Science*, *368*(6496), 1257–1260. https://doi.org/10.1126/science.aaz5819

Brugger, J., Liu, W., Etschmann, B., Mei, Y., Sherman, D. M., & Testemale, D. (2016). A review of the coordination chemistry of hydrothermal systems, or do coordination changes make ore deposits? *Chemical Geology*, *447*, 219–253. https://doi.org/10.1016/j.chemgeo.2016.10.021

Bühler, W., Dinjus, E., Ederer, H. J., Kruse, A., & Mas, C. (2002). Ionic reactions and pyrolysis of glycerol as competing reaction pathways in near- and supercritical water. *The Journal of Supercritical Fluids*, *22*(1), 37–53. https://doi.org/10.1016/S0896-8446(01)00105-X

Bühring, S. I., Elvert, M., & Witte, U. (2005). The microbial community structure of different permeable sandy sediments characterized by the investigation of bacterial fatty acids and fluorescence in situ hybridization. *Environmental Microbiology*, *7*(2), 281–293. https://doi.org/10.1111/j.1462-2920.2004.00710.x

Bull, H. B., & Breese, K. (1974). Surface tension of amino acid solutions: A hydrophobicity scale of the amino acid residues. *Archives of Biochemistry and Biophysics, 161*(2), 665–670. https://doi.org/10.1016/0003-9861(74)90352-X

Cable, M. L., Porco, C., Glein, C. R., German, C. R., MacKenzie, S. M., Neveu, M., Hoehler, T. M., Hofmann, A. E., Hendrix, A. R., Eigenbrode, J., Postberg, F., Spilker, L. J., McEwen, A., Khawaja, N., Waite, J. H., Wurz, P., Helbert, J., Anbar, A., Vera, J.-P. de, & Núñez, J. (2021). The science case for a return to Enceladus. *The Planetary Science Journal*, *2*(4), 132. https://doi.org/10.3847/PSJ/abfb7a

Cable, M. L., Spilker, L. J., Postberg, F., Waite, J. H., Kempf, S., Clark, K., Reh, K., Sherwood, B., & Lunine, J. I. (2017). *Enceladus Life Finder (ELF): A proposed mission to assess the habitability of a plume-bearing world*. *2042*, 4124. Habitable Worlds 2017: A System Science Workshop.

Capone, D. G., Popa, R., Flood, B., & Nealson, K. H. (2006). Follow the nitrogen. *Science*, *312*(5774), 708–709. https://doi.org/10.1126/science.1111863

Castillo-Rogez, J., Neveu, M., McSween, H. Y., Fu, R. R., Toplis, M. J., & Prettyman, T. (2018). Insights into Ceres's evolution from surface composition. *Meteoritics & Planetary Science*, *53*(9), 1820–1843. https://doi.org/10.1111/maps.13181

Chan, Q. H. S., Watson, J. S., Sephton, M. A., O'Brien, Á. C., & Hallis, L. J. (2024). The amino acid and polycyclic aromatic hydrocarbon compositions of the promptly recovered CM2 Winchcombe carbonaceous chondrite. *Meteoritics & Planetary Science*, *59*(5), 1101–1130. https://doi.org/10.1111/maps.13936

Chandru, K., Imai, E., Kaneko, T., Obayashi, Y., & Kobayashi, K. (2013). Survivability and abiotic reactions of selected amino acids in different hydrothermal system simulators. *Origins of Life and Evolution of Biospheres*, *43*(2), 99–108. https://doi.org/10.1007/s11084-013-9330-9

Changi, S., Zhu, M., & Savage, P. E. (2012). Hydrothermal reaction kinetics and pathways of phenylalanine alone and in binary mixtures. *ChemSusChem*, *5*(9), 1743–1757. https://doi.org/10.1002/cssc.201200146

Charlou, J. L., Donval, J. P., Fouquet, Y., Jean-Baptiste, P., & Holm, N. (2002). Geochemistry of high H_2 and CH_4 vent fluids issuing from ultramafic rocks at the Rainbow hydrothermal field (36°14′N, MAR). *Chemical Geology*, *191*(4), 345–359. https://doi.org/10.1016/S0009-2541(02)00134-1

Chau, R., Mitchell, A. C., Minich, R. W., & Nellis, W. J. (2001). Electrical conductivity of water compressed dynamically to pressures of 70–180 GPa (0.7–1.8 Mbar). *The Journal of Chemical Physics*, *114*(3), 1361–1365. https://doi.org/10.1063/1.1332079

Cho, Y. S., Oh, I.-H., Kim, J. H., Kim, J. I., Lee, K.-B., & Nah, I. W. (2025). Production of abiotic or biogenic hydrocarbons on rock particles in the presence of H_2O and carbon compounds. *Scientific Reports*, *15*(1), 2085. https://doi.org/10.1038/s41598-025-86121-9

Cochran, R. E., Jayarathne, T., Stone, E. A., & Grassian, V. H. (2016). Selectivity across the interface: A test of surface activity in the composition of organic-enriched aerosols from bubble bursting. *The Journal of Physical Chemistry Letters*, *7*(9), 1692–1696. https://doi.org/10.1021/acs.jpclett.6b00489

Cohen, N. R., Noble, A. E., Moran, D. M., McIlvin, M. R., Goepfert, T. J., Hawco, N. J., German, C. R., Horner, T. J., Lamborg, C. H., McCrow, J. P., Allen, A. E., & Saito, M. A. (2021). Hydrothermal trace metal release and microbial metabolism in the northeastern Lau Basin of the South Pacific Ocean. *Biogeosciences*, *18*(19), 5397–5422. https://doi.org/10.5194/bg-18-5397-2021

Concha-Herrera, V., Lerma-García, M. J., Herrero-Martínez, J. M., & Simó-Alfonso, E. F. (2010). Classification of vegetable oils according to their botanical origin using amino acid profiles established by High Performance Liquid Chromatography with UV–vis detection: A first approach. *Food Chemistry*, *120*(4), 1149–1154. https://doi.org/10.1016/j.foodchem.2009.11.046

Concha-Herrera, V., Vivó-Truyols, G., Torres-Lapasió, J. R., & García-Alvarez-Coque, M. C. (2005). Limits of multi-linear gradient optimisation in reversed-phase liquid chromatography. *Journal of Chromatography A*, *1063*(1), 79–88. https://doi.org/10.1016/j.chroma.2004.12.001

Cordier, M., Uehara, T., Baztan, J., Jorgensen, B., & Yan, H. (2021). Plastic pollution and economic growth: The influence of corruption and lack of education. *Ecological Economics*, *182*, 106930. https://doi.org/10.1016/j.ecolecon.2020.106930

Corliss, J. B., Dymond, J., Gordon, L. I., Edmond, J. M., von Herzen, R. P., Ballard, R. D., Green, K., Williams, D., Bainbridge, A., Crane, K., & van Andel, T. H. (1979). Submarine thermal springs on the Galápagos Rift. *Science*, *203*(4385), 1073–1083. https://doi.org/10.1126/science.203.4385.1073

Cox, J. S., & Seward, T. M. (2007). The hydrothermal reaction kinetics of aspartic acid. *Geochimica et Cosmochimica Acta*, *71*(4), 797–820. https://doi.org/10.1016/j.gca.2006.06.1558

Daly, R. T., Marchand, A. N. R., Pontefract, A., Stockstill-Cahill, K. R., Martin, A. C., Sunshine, J. M., Mayorga, L. C., & Rizos, J. L. (2023, October 17). *The effects of impacts on the reflectance spectra of aliphatic organics: Implications for Ceres*. GSA Connects 2023 Meeting in Pittsburgh, Pennsylvania. https://gsa.confex.com/gsa/2023AM/meetingapp.cgi/Paper/392730

Dasgupta, R., & Hirschmann, M. M. (2010). The deep carbon cycle and melting in Earth's interior. *Earth and Planetary Science Letters*, *298*(1), 1–13. https://doi.org/10.1016/j.epsl.2010.06.039

De Sanctis, M. C., Raponi, A., Ammannito, E., Ciarniello, M., Toplis, M. J., McSween, H. Y., Castillo-Rogez, J. C., Ehlmann, B. L., Carrozzo, F. G., Marchi, S., Tosi, F., Zambon, F., Capaccioni, F., Capria, M. T., Fonte, S., Formisano, M., Frigeri, A., Giardino, M., Longobardo, A., … Russell, C. T. (2016). Bright carbonate deposits as evidence of aqueous alteration on (1) Ceres. *Nature*, *536*(7614), 54–57. https://doi.org/10.1038/nature18290

Dick, G. J. (2019). The microbiomes of deep-sea hydrothermal vents: Distributed globally, shaped locally. *Nature*, *17*, 271–283.

Dorn, E. D., McDonald, G. D., Storrie-Lombardi, M. C., & Nealson, K. H. (2003). Principal component analysis and neural networks for detection of amino acid biosignatures. *Icarus*, *166*(2), 403–409. https://doi.org/10.1016/j.icarus.2003.08.011

Dotson, R. (2020). *Planetary Astrobiology*. University of Arizona Press. https://www.jstor.org/stable/j.ctv105bb62

Douville, E., Charlou, J. L., Oelkers, E. H., Bienvenu, P., Jove Colon, C. F., Donval, J. P., Fouquet, Y., Prieur, D., & Appriou, P. (2002). The rainbow vent fluids (36°14′N, MAR): The influence of ultramafic rocks and phase separation on trace metal content in Mid-Atlantic Ridge hydrothermal fluids. *Chemical Geology*, *184*(1), 37–48. https://doi.org/10.1016/S0009-2541(01)00351-5

Dudd, L., Venardou, E., Garcia-Verdugo, E., Licence, P., Blake, A., Wilson, C., & Poliakoff, M. (2003). Synthesis of benzimidazoles in high-temperature water. *Green Chemistry*, *5*.

Eigenbrode, J., Gold, R. E., McKay, C. P., Hurford, T., & Davila, A. (2018). *Searching for life in an ocean world: The Enceladus Life Signatures and Habitability (ELSAH) mission concept*. *42*, F3.6-3-18. 42nd COSPAR Scientific Assembly.

Estrada, C. F., Mamajanov, I., Hao, J., Sverjensky, D. A., Cody, G. D., & Hazen, R. M. (2017). Aspartate transformation at 200°C with brucite [$Mg(OH)_2$], NH_3, and H_2: Implications for prebiotic molecules in hydrothermal systems. *Chemical Geology*, *457*, 162–172. https://doi.org/10.1016/j.chemgeo.2017.03.025

Fagents, S. A. (2003). Considerations for effusive cryovolcanism on Europa: The post-Galileo perspective. *Journal of Geophysical Research: Planets*, *108*(E12). https://doi.org/10.1029/2003JE002128

Fan, Y., Hornung, U., Dahmen, N., & Kruse, A. (2018). Hydrothermal liquefaction of protein-containing biomass: Study of model compounds for Maillard reactions. *Biomass Conversion and Biorefinery*, *8*.

Fecteau, K. M., Gould, I. R., Glein, C. R., Williams, L. B., Hartnett, H. E., & Shock, E. L. (2019). Production of carboxylic acids from aldehydes under hydrothermal conditions: A kinetics study of benzaldehyde. *ACS Earth and Space Chemistry, 3*(2), 170–191. https://doi.org/10.1021/acsearthspacechem.8b00130

Fifer, L. M., Catling, D. C., & Toner, J. D. (2022). Chemical fractionation modeling of plumes indicates a gas-rich, moderately alkaline Enceladus ocean. *The Planetary Science Journal, 3*(8), 191. https://doi.org/10.3847/PSJ/ac7a9f

Foustoukos, D. I. (2016). On the solvation properties of supercritical electrolyte solutions. *Chemical Geology*, *447*, 191–198. https://doi.org/10.1016/j.chemgeo.2016.10.039

Fox-Powell, M. G., & Cousins, C. R. (2021). Partitioning of crystalline and amorphous phases during freezing of simulated Enceladus ocean fluids. *Journal of Geophysical Research: Planets*, *126*(1), e2020JE006628. https://doi.org/10.1029/2020JE006628

Fritscher, M., & Teiser, J. (2021). CO2-ice Collisions: A new experimental approach. *The Astrophysical Journal*, *923*(2), 134. https://doi.org/10.3847/1538-4357/ac2df4

Fryer, P., Pearce, J. A., Stokking, L. B., & et al. (Eds.). (1992). *Short-chain organic acids in interstitial waters from Mariana and Bonin forearc serpentines: Leg 125*. *125*. https://doi.org/10.2973/odp.proc.sr.125.1992

Fu, X., Jamison, M., Jubb, A. M., Liao, Y., Aspin, A., Hayes, K., Glein, C. R., & Yang, Z. (2020a). Effect of copper salts on hydrothermal oxidative decarboxylation: A study of phenylacetic acid. *Chemical Communications, 56*, 2791–2794.

Fu, X., Liao, Y., Aspin, A., & Yang, Z. (2020b). Effect of copper salts on amide hydrothermal formation and reactivity. *ACS Earth and Space Chemistry, 4*(9), 1596–1603. https://doi.org/10.1021/acsearthspacechem.0c00150

Fu, X., Liao, Y., Glein, C. R., Jamison, M., Hayes, K., Zaporski, J., & Yang, Z. (2020c). Direct synthesis of amides from amines and carboxylic acids under hydrothermal conditions. *ACS Earth and Space Chemistry*, *4*(5), 722–729.

Fuchida, S., Mizuno, Y., Masuda, H., Toki, T., & Makita, H. (2014). Concentrations and distributions of amino acids in black and white smoker fluids at temperatures over 200°C. *Organic Geochemistry*, *66*, 98–106. https://doi.org/10.1016/j.orggeochem.2013.11.008

Gall, S. C., & Thompson, R. C. (2015). The impact of debris on marine life. *Marine Pollution Bulletin*, *92*(1), 170–179. https://doi.org/10.1016/j.marpolbul.2014.12.041

Ganesan, A., Dreyer, J., Wang, F., Akola, J., & Larrucea, J. (2013). Density functional study of Cu^{2+}-phenylalanine complex under micro-solvation environment. *Journal of Molecular Graphics and Modelling*, *45*, 180–191. https://doi.org/10.1016/j.jmgm.2013.08.015

Gentilcore, C., Jin, K., Barzallo, G., Vozka, P., & Wang, N.-H. L. (2024). Low-pressure hydrothermal processing for conversion of polystyrene into oils. *Journal of Environmental Chemical Engineering*, *12*(5), 113836. https://doi.org/10.1016/j.jece.2024.113836

Geyer, R., Jambeck, J. R., & Law, K. L. (2017). Production, use, and fate of all plastics ever made. *Science Advances*, *3*(7), e1700782. https://doi.org/10.1126/sciadv.1700782

Glavin, D. P., Callahan, M. P., Dworkin, J. P., & Elsila, J. E. (2010). The effects of parent body processes on amino acids in carbonaceous chondrites. *Meteoritics & Planetary Science*, *45*(12), 1948–1972. https://doi.org/10.1111/j.1945-5100.2010.01132.x

Glavin, D. P., McLain, H. L., Dworkin, J. P., Parker, E. T., Elsila, J. E., Aponte, J. C., Simkus, D. N., Pozarycki, C. I., Graham, H. V., Nittler, L. R., & Alexander, C. M. O. (2020). Abundant extraterrestrial amino acids in the primitive CM carbonaceous chondrite Asuka 12236. *Meteoritics & Planetary Science*, *55*(9), 1979–2006. https://doi.org/10.1111/maps.13560

Glein, C. R., Gould, I. R., Lorance, E. D., Hartnett, H. E., & Shock, E. L. (2020). Mechanisms of decarboxylation of phenylacetic acids and their sodium salts in water at high temperature and pressure. *Geochimica et Cosmochimica Acta*, *269*, 597–621. https://doi.org/10.1016/j.gca.2019.11.003

Glein, C. R., & Waite, J. H. (2020). The carbonate geochemistry of Enceladus' ocean. *Geophysical Research Letters*, *47*(3), e2019GL085885. https://doi.org/10.1029/2019GL085885

Goguen, J. D., Buratti, B. J., Brown, R. H., Clark, R. N., Nicholson, P. D., Hedman, M. M., Howell, R. R., Sotin, C., Cruikshank, D. P., Baines, K. H., Lawrence, K. J., Spencer, J. R., & Blackburn, D. G. (2013). The temperature and width of an active fissure on Enceladus measured with *Cassini* VIMS during the 14 April 2012 South Pole flyover. *Icarus*, *226*(1), 1128–1137. https://doi.org/10.1016/j.icarus.2013.07.012

Guzman, M., Lorenz, R., Hurley, D., Farrell, W., Spencer, J., Hansen, C., Hurford, T., Ibea, J., Carlson, P., & McKay, C. P. (2019). Collecting amino acids in the Enceladus plume. *International Journal of Astrobiology*, *18*(1), 47–59. https://doi.org/10.1017/S1473550417000544

Haase, K. M., Koschinsky, A., Petersen, S., Devey, C. W., German, C., Lackschewitz, K. S., Melchert, B., Seifert, R., Borowski, C., Giere, O., & Paulick, H. (2009). Diking, young volcanism and diffuse hydrothermal activity on the southern Mid-Atlantic Ridge: The Lilliput field at 9°33′S. *Marine Geology*, *266*(1), 52–64. https://doi.org/10.1016/j.margeo.2009.07.012

Haberstroh, P. R., & Karl, D. M. (1989). Dissolved free amino acids in hydrothermal vent habitats of the Guaymas Basin. *Geochimica et Cosmochimica Acta*, *53*(11), 2937–2945. https://doi.org/10.1016/0016-7037(89)90170-1

Hamerly, T., Tripet, B., Wurch, L., Hettich, R. L., Podar, M., Bothner, B., & Copié, V. (2015). Characterization of fatty acids in Crenarchaeota by GC-MS and NMR. *Archaea*, *2015*(1), 472726. https://doi.org/10.1155/2015/472726

Hand, K. P., Chyba, C. F., Priscu, J. C., Carlson, R. W., Nealson, K. H., & Dotson, R. (2009). Astrobiology and the potential for life on Europa. R. T. Pappalardo, W. B. McKinnon, & K. K. Khurana (Eds.), *Europa* (pp. 589–630). University of Arizona Press; JSTOR. https://doi.org/10.2307/j.ctt1xp3wdw.32

Hand, K. P., Murray, A., & Gavin, J. B. (2016). *Europa Lander Study 2016 Report*. https://europa.nasa.gov/resources/58/europa-lander-study-2016-report

Hand, K. P., Phillips, C. B., Murray, A., Garvin, J. B., Maize, E. H., Gibbs, R. G., Reeves, G., Martin, A. M. S., Tan-Wang, G. H., Krajewski, J., Hurst, K., Crum, R., Kennedy, B. A., McElrath, T. P., Gallon, J. C., Sabahi, D., Thurman, S. W., Goldstein, B., Estabrook, P., … Wasiolek, M. (2022). Science goals and mission architecture of the Europa Lander mission concept. *The Planetary Science Journal*, *3*(1), 22. https://doi.org/10.3847/PSJ/ac4493

Hedges, J. I. (1992). Global biogeochemical cycles: Progress and problems. *Marine Chemistry*, *39*(1), 67–93. https://doi.org/10.1016/0304-4203(92)90096-S

Heger, K., Uematsu, M., & Franck, E. U. (1980). The static dielectric constant of water at high pressures and temperatures to 500 MPa and 550°C. *Berichte Der Bunsengesellschaft Für Physikalische Chemie*, *84*(8), 758–762. https://doi.org/10.1002/bbpc.19800840814

Helgeson, H. C., Richard, L., McKenzie, W. F., Norton, D. L., & Schmitt, A. (2009). A chemical and thermodynamic model of oil generation in hydrocarbon source rocks. *Geochimica et Cosmochimica Acta*, *73*(3), 594–695. https://doi.org/10.1016/j.gca.2008.03.004

Helmer Pedersen, T., & Conti, F. (2017). Improving the circular economy via hydrothermal processing of high-density waste plastics. *Waste Management*, *68*, 24–31. https://doi.org/10.1016/j.wasman.2017.06.002

Hemingway, D. J., & Mittal, T. (2019). Enceladus's ice shell structure as a window on internal heat production. *Icarus*, *332*, 111–131. https://doi.org/10.1016/j.icarus.2019.03.011

Hendrix, A., Hurford, T., Barge, L. M., Bland, M., Bowman, J., Brinckerhodd, W., Buratti, B., Cable, M. L., Castillo-Rogez, J., Collins, G. C., Diniega, S., German, C. R., Hayes, A., & Hoehler, T. M. (2019). *The NASA Roadmap to Ocean Worlds | Astrobiology*. *19*. https://www.liebertpub.com/doi/10.1089/ast.2018.1955

Herboth, R., Gopakumar, G., Caleman, C., & Wohlert, M. (2021). Charge state dependence of amino acid propensity at water surface: Mechanisms elucidated by molecular dynamics simulations. *The Journal of Physical Chemistry A*, *125*(22), 4705–4714. https://doi.org/10.1021/acs.jpca.0c10963

Hoehler, T. M., Amend, J. P., & Shock, E. L. (2007). A "follow the energy" approach for astrobiology. *Astrobiology*, *7*(6), 819–823. https://doi.org/10.1089/ast.2007.0207

Holm, N. G., & Charlou, J. L. (2001). Initial indications of abiotic formation of hydrocarbons in the Rainbow ultramafic hydrothermal system, Mid-Atlantic Ridge. *Earth and Planetary Science Letters*, *191*(1), 1–8. https://doi.org/10.1016/S0012-821X(01)00397-1

Holzapfel, W. B. (1969). Effect of pressure and temperature on the conductivity and ionic dissociation of water up to 100 kbar and 1000°C. *The Journal of Chemical Physics*, *50*(10), 4424–4428. https://doi.org/10.1063/1.1670914

Hongthong, S., Raikova, S., Leese, H., & Chuck, C. (2020). Co-processing of common plastics with pistachio hulls via hydrothermal liquefaction. *Waste Management*, *102*.

Horsfield, B., Schenk, H. J., Zink, K., Ondrak, R., Dieckmann, V., Kallmeyer, J., Mangelsdorf, K., Di Primio, R., Wilkes, H., Parkes, R. J., Fry, J., & Cragg, B. (2006). Living microbial ecosystems within the active zone of catagenesis: Implications for feeding the deep biosphere. *Earth and Planetary Science Letters*, *246*(1–2), 55–69.

Hsu, H.-W., Postberg, F., Sekine, Y., Shibuya, T., Kempf, S., Horányi, M., Juhász, A., Altobelli, N., Suzuki, K., Masaki, Y., Kuwatani, T., Tachibana, S., Sirono, S., Moragas-Klostermeyer, G., & Srama, R. (2015). Ongoing hydrothermal activities within Enceladus. *Nature*, *519*(7542), Article 7542. https://doi.org/10.1038/nature14262

Hu, Q., Zhao, H., Wu, X., & Liang, Y. (2022). A temperature-dependent hydrating structure around SO_4^{2-} investigated from Raman spectroscopy. *Journal of Raman Spectroscopy*, *53*(10), 1694–1703. https://doi.org/10.1002/jrs.6348

Hunter, S. E., & Savage, P. E. (2004). Recent advances in acid- and base-catalyzed organic synthesis in high-temperature liquid water. *Chemical Engineering Science, 59*(22), 4903–4909. https://doi.org/10.1016/j.ces.2004.09.009

Ingersoll, A. P., & Nakajima, M. (2016). Controlled boiling on Enceladus. 2. Model of the liquid-filled cracks. *Icarus, 272*, 319–326. https://doi.org/10.1016/j.icarus.2015.12.040

Jian, X., Zhuang, X., Li, B., Xu, X., Wei, Z., Song, Y., & Jiang, E. (2018). Comparison of characterization and adsorption of biochars produced from hydrothermal carbonization and pyrolysis. *Environmental Technology and Innovation, 10*.

Johnson, J. W., Oelkers, E. H., & Helgeson, H. C. (1992). SUPCRT92: A software package for calculating the standard molal thermodynamic properties of minerals, gases, aqueous species, and reactions from 1 to 5000 bar and 0 to 1000°C. *Computers & Geosciences, 18*(7), 899–947. https://doi.org/10.1016/0098-3004(92)90029-Q

Johnson-Finn, K. N., Williams, L. B., Gould, I. R., Hartnett, H. E., & Shock, E. L. (2021). Hydrothermal one-electron oxidation of carboxylic acids in the presence of iron oxide minerals. *ACS Earth and Space Chemistry, 5*(10), 2715–2728.

Jones, D. M., Head, I. M., Gray, N. D., Adams, J. J., Rowan, A. K., Aitken, C. M., Bennett, B., Huang, H., Brown, A., Bowler, B. F. J., Oldenburg, T., Erdmann, M., & Larter, S. R. (2008). Crude-oil biodegradation via methanogenesis in subsurface petroleum reservoirs. *Nature, 451*, 176–180.

Kanno, H., Yonehama, K., Somraj, A., & Yoshimura, Y. (2006). Structure-making ions become structure breakers in glassy aqueous electrolyte solutions. *Chemical Physics Letters, 427*(1), 82–86. https://doi.org/10.1016/j.cplett.2006.06.055

Kaplan, H. H., Milliken, R. E., & Alexander, C. M. O. (2018). New constraints on the abundance and composition of organic matter on Ceres. *Geophysical Research Letters, 45*(11), 5274–5282. https://doi.org/10.1029/2018GL077913

Kasmuri, N., Tarmizi, N. A. A., & Mojiri, A. (2022). Occurrence, impact, toxicity, and degradation methods of microplastics in environment—A review. *Environmental Science and Pollution Research, 29*(21), 30820–30836. https://doi.org/10.1007/s11356-021-18268-7

Kelemen, P. B., & Manning, C. E. (2015). Reevaluating carbon fluxes in subduction zones, what goes down, mostly comes up. *Proceedings of the National Academy of Sciences, 112*(30), E3997–E4006. https://doi.org/10.1073/pnas.1507889112

Khawaja, N., Postberg, F., Hillier, J., Klenner, F., Kempf, S., Nölle, L., Reviol, R., Zou, Z., & Srama, R. (2019). Low-mass nitrogen-, oxygen-bearing, and aromatic compounds in Enceladean ice grains. *Monthly Notices of the Royal Astronomical Society*, *489*(4), 5231–5243. https://doi.org/10.1093/mnras/stz2280

Koelmans, A. A., Kooi, M., Law, K. L., & van Sebille, E. (2017). All is not lost: Deriving a top-down mass budget of plastic at sea. *Environmental Research Letters*, *12*(11), 114028. https://doi.org/10.1088/1748-9326/aa9500

Körner, P. (2021). Hydrothermal degradation of amino acids. *ChemSusChem*, *14*(22), 4947–4957. https://doi.org/10.1002/cssc.202101487

Kühn, S., & van Franeker, J. A. (2020). Quantitative overview of marine debris ingested by marine megafauna. *Marine Pollution Bulletin*, *151*, 110858. https://doi.org/10.1016/j.marpolbul.2019.110858

Kumar, P., & Kumar, R. (2021). 6 - Synthesis process of functionalized ZnO nanostructure for additive manufacturing: A state-of-the-art review. S. Singh & C. M. Hussain (Eds.), *Additive Manufacturing with Functionalized Nanomaterials* (pp. 135–153). Elsevier. https://doi.org/10.1016/B978-0-12-823152-4.00002-8

Kwak, H., Shin, H.-Y., Bae, S.-Y., & Kumazawa, H. (2006). Characteristics and kinetics of degradation of polystyrene in supercritical water. *Journal of Applied Polymer Science*, *101*(1), 695–700. https://doi.org/10.1002/app.23896

Lang, S. Q., & Brazelton, W. J. (2020). Habitability of the marine serpentinite subsurface: A case study of the Lost City hydrothermal field. *Philosophical Transactions of the Royal Society A: Mathematical, Physical and Engineering Sciences*, *378*(2165), 20180429. https://doi.org/10.1098/rsta.2018.0429

Large, R. R. (1977). Chemical evolution and zonation of massive sulfide deposits in volcanic terrains. *Economic Geology*, *72*(4), 549–572. https://doi.org/10.2113/gsecongeo.72.4.549

LaRowe, D. E., & Regnier, P. (2008). Thermodynamic potential for the abiotic synthesis of adenine, cytosine, guanine, thymine, uracil, ribose, and deoxyribose in hydrothermal systems. *Origin of Life and Evolution of Biospheres*, *38*.

Larter, S., Wilhelms, A., Head, I., Koopmans, M., Aplin, A., Di Primio, R., Zwach, C., Erdmann, M., & Telnaes, N. (2003). The controls on the composition of biodegraded oils in the deep subsurface—Part 1: Biodegradation rates in petroleum reservoirs. *Organic Geochemistry*, *34*(4), 601–613. https://doi.org/10.1016/S0146-6380(02)00240-1

Lau, W. W. Y., Shiran, Y., Bailey, R. M., Cook, E., Stuchtey, M. R., Koskella, J., Velis, C. A., Godfrey, L., Boucher, J., Murphy, M. B., Thompson, R. C., Jankowska, E., Castillo Castillo, A., Pilditch, T. D., Dixon, B., Koerselman, L., Kosior, E., Favoino, E., Gutberlet, J., … Palardy, J. E. (2020). Evaluating scenarios toward zero plastic pollution. *Science*, *369*(6510), 1455–1461. https://doi.org/10.1126/science.aba9475

Lebreton, L., & Andrady, A. (2019). Future scenarios of global plastic waste generation and disposal. *Palgrave Communications*, *5*(1), 1–11. https://doi.org/10.1057/s41599-018-0212-7

Lee, A., & Liew, M. S. (2021). Tertiary recycling of plastics waste: An analysis of feedstock, chemical and biological degradation methods. *Journal of Material Cycles and Waste Management*, *23*(1), 32–43. https://doi.org/10.1007/s10163-020-01106-2

Lee, N., Foustoukos, D. I., Sverjensky, D. A., Cody, G. D., & Hazen, R. M. (2014a). The effects of temperature, pH and redox state on the stability of glutamic acid in hydrothermal fluids. *Geochimica et Cosmochimica Acta*, *135*, 66–86. https://doi.org/10.1016/j.gca.2014.02.043

Lee, N., Foustoukos, D. I., Sverjensky, D. A., Hazen, R. M., & Cody, G. D. (2014b). Hydrogen enhances the stability of glutamic acid in hydrothermal environments. *Chemical Geology*, *386*, 184–189. https://doi.org/10.1016/j.chemgeo.2014.08.012

Lemke, K. H., Rosenbauer, R. J., & Bird, D. K. (2009). Peptide synthesis in early Earth hydrothermal systems. *Astrobiology*, *9*(2), 141–146. https://doi.org/10.1089/ast.2008.0166

Leslie, H. A., van Velzen, M. J. M., Brandsma, S. H., Vethaak, A. D., Garcia-Vallejo, J. J., & Lamoree, M. H. (2022). Discovery and quantification of plastic particle pollution in human blood. *Environment International*, *163*, 107199. https://doi.org/10.1016/j.envint.2022.107199

Li, J., & Brill, T. B. (2003). Decarboxylation mechanism of amino acids by density functional theory. *The Journal of Physical Chemistry A*, *107*(31), 5993–5997. https://doi.org/10.1021/jp022477y

Li, J., Wang, X., Klein, M. T., & Brill, T. B. (2002). Spectroscopy of hydrothermal reactions, 19: pH and salt dependence of decarboxylation of α-alanine at 280–330°C in an FT-IR spectroscopy flow reactor. *International Journal of Chemical Kinetics*, *34*(4), 271–277. https://doi.org/10.1002/kin.10045

Liao, Y., Aspin, A., Fu, X., & Yang, Z. (2021). Hydrothermal transformations of alcohols with Copper(II) and Iron(III) salts. *ACS Earth and Space Chemistry*, *5*(8), 2021–2031. https://doi.org/10.1021/acsearthspacechem.1c00113

Liao, Y., Aspin, A., & Yang, Z. (2022). Anaerobic oxidation of aldehydes to carboxylic acids under hydrothermal conditions. *RSC Advances, 12*(3), 1738–1741. https://doi.org/10.1039/D1RA08444E

Lide, D. R. (1991). *CRC handbook of chemistry and physics: A ready-reference book of chemical and phyical data* (72nd ed. (1991-92 ed.)). CRC Press.

Liu, Q., Wu, Y., Yan, P., Zhang, Y., & Xu, R. (2011). Polyisobutylene with high exo-olefin content via β-H elimination in the cationic polymerization of isobutylene with $H_2O/FeCl_3$/Dialkyl ether initiating system. *Macromolecules, 44*(7), 1866–1875. https://doi.org/10.1021/ma1027017

Liu, W., Jiang, H., & Yu, H. (2015). Thermochemical conversion of lignin for functional materials: A review and future direction. *Green Chemistry*, *17*(11), 4888-4907

Liu, X., Wu, M., Li, C., Yu, P., Feng, S., Li, Y., & Zhang, Q. (2022). Interaction structure and affinity of zwitterionic amino acids with important metal cations (Cd^{2+}, Cu^{2+}, Fe^{3+}, Hg^{2+}, Mn^{2+}, Ni^{2+} and Zn^{2+}) in aqueous solution: A theoretical study. *Molecules*, *27*(8). https://www.mdpi.com/1420-3049/27/8/2407

Liu, Z., Tian, G., Zhu, S., He, C., Yue, H., & Feng, S. (2013). Ready Hydrothermal Reactions from Carbon Dioxide to Methane. *ACS Sustainable Chemistry and Engineering*, *1*(3), 313–315).

Lobry, J. R., & Gautier, C. (1994). Hydrophobicity, expressivity and aromaticity are the major trends of amino-acid usage in 999 Escherichia coli chromosome-encoded genes. *Nucleic Acids Research, 22*(15), 3174–3180. https://doi.org/10.1093/nar/22.15.3174

Loison, A., Dubant, S., Adam, P., & Albrecht, P. (2010). Elucidation of an iterative process of carbon–carbon bond formation of prebiotic significance. *Astrobiology, 10*(10), 973–988. https://doi.org/10.1089/ast.2009.0441

Longnecker, K., Sievert, S. M., Sylva, S. P., Seewald, J. S., & Kujawinski, E. B. (2018). Dissolved organic carbon compounds in deep-sea hydrothermal vent fluids from the East Pacific Rise at 9°50′N. *Organic Geochemistry*, *125*, 41–49. https://doi.org/10.1016/j.orggeochem.2018.08.004

Lonsdale, P. (1977). Clustering of suspension-feeding macrobenthos near abyssal hydrothermal vents at oceanic spreading centers. *Deep Sea Research, 24*(9), 857–863. https://doi.org/10.1016/0146-6291(77)90478-7

Lough, A. J. M., Connelly, D. P., Homoky, W. B., Hawkes, J. A., Chavagnac, V., Castillo, A., Kazemian, M., Nakamura, K., Araki, T., Kaulich, B., & Mills, R. A. (2019). Diffuse Hydrothermal Venting: A hidden source of Iron to the oceans. *Frontiers in Marine Science*, *6*. https://doi.org/10.3389/fmars.2019.00329

Lowell, R. P., & DuBose, M. (2005). Hydrothermal systems on Europa. *Geophysical Research Letters*, *32*(5). https://doi.org/10.1029/2005GL022375

Lu, X., Ma, X., Chen, X., Yao, Z., & Zhang, C. (2020). Co-hydrothermal carbonization of polyvinyl chloride and corncob for clean solid fuel production. *Bioresource Technology*, *301*.

Ma, C., & Zhao, Y. (2018). $FeCl_3$ -catalyzed dimerization/elimination of 1,1-diarylalkenes: Efficient synthesis of functionalized 4 H -chromenes. *Organic & Biomolecular Chemistry*, *16*(5), 703–706. https://doi.org/10.1039/C7OB02941A

MacIvor, J. S., & Moore, A. E. (2013). Bees collect polyurethane and polyethylene plastics as novel nest materials. *Ecosphere*, *4*(12), art155. https://doi.org/10.1890/ES13-00308.1

MacKenzie, S. M., Neveu, M., Davila, A. F., Lunine, J. I., Cable, M. L., Phillips-Lander, C. M., Eigenbrode, J. L., Waite, J. H., Craft, K. L., Hofgartner, J. D., McKay, C. P., Glein, C. R., Burton, D., Kounaves, S. P., Mathies, R. A., Vance, S. D., Malaska, M. J., Gold, R., German, C. R., … Heldmann, J. (2022). Science objectives for flagship-class mission concepts for the search for evidence of life at Enceladus. *Astrobiology*, *22*(6), 685–712. https://doi.org/10.1089/ast.2020.2425

MacKenzie, S. M., Neveu, M., Davila, A. F., Lunine, J. I., Craft, K. L., Cable, M. L., Phillips-Lander, C. M., Hofgartner, J. D., Eigenbrode, J. L., Waite, J. H., Glein, C. R., Gold, R., Greenauer, P. J., Kirby, K., Bradburne, C., Kounaves, S. P., Malaska, M. J., Postberg, F., Patterson, G. W., … Spilker, L. J. (2021). The Enceladus Orbilander mission concept: Balancing return and resources in the search for life. *The Planetary Science Journal*, *2*(2), 77. https://doi.org/10.3847/PSJ/abe4da

Madigan, M., Martinko, J., Stahl, D., & Clark, D. P. (2011). *Brock Biology of Microorganisms*. Pearson Higher Ed.

Madsen, R., & Glasius, M. (2019). How do hydrothermal liquefaction conditions and feedstock type influence product distribution and elemental composition? *Industrial and Engineering Chemistry Research*, *58*(37).

Malhotra, M., & Garg, A. (2020). Hydrothermal carbonization of centrifuged sewage sludge: Determination of resource recovery from liquid fraction and thermal behavior of hydrochar. *Waste Management*, *117*.

Marlin, T. C., Weber, J. M., Sheppard, R. Y., Perl, S., Diener, D., Baum, M. M., & Barge, L. M. (2025). Chemical gardens as analogs for prebiotic chemistry on ocean worlds. *Chem*, *11*(1). https://doi.org/10.1016/j.chempr.2024.08.012

Marsh, A., Miles, R. E. H., Rovelli, G., Cowling, A. G., Nandy, L., Dutcher, C. S., & Reid, J. P. (2017). Influence of organic compound functionality on aerosol hygroscopicity: Dicarboxylic acids, alkyl-substituents, sugars and amino acids. *Atmospheric Chemistry and Physics*, *17*(9), 5583–5599. https://doi.org/10.5194/acp-17-5583-2017

Martin, W., Baross, J., Kelley, D., & Russell, M. J. (2008). Hydrothermal vents and the origin of life. *Nature Reviews Microbiology*, *6*(11), 805–814. https://doi.org/10.1038/nrmicro1991

Martins, Z., Alexander, C. M. O., Orzechowska, G. E., Fogel, M. L., & Ehrenfreund, P. (2007). Indigenous amino acids in primitive CR meteorites. *Meteoritics & Planetary Science*, *42*(12), 2125–2136. https://doi.org/10.1111/j.1945-5100.2007.tb01013.x

Mayo, F. R. (1968). The dimerization of styrene. *Journal of the American Chemical Society*, *90*(5), 1289–1295. https://doi.org/10.1021/ja01007a032

McCollom, T. M. (2013). Laboratory simulations of abiotic hydrocarbon formation in Earth's deep subsurface. *Reviews in Mineralogy and Geochemistry*, *75*(1), 467–494. https://doi.org/10.2138/rmg.2013.75.15

McCollom, T. M., Ritter, G., & Simoneit, B. R. T. (1999). Lipid synthesis under hydrothermal conditions by Fischer-Tropsch-type reactions. *Origins of Life and Evolution of the Biosphere*, *29*(2), 153–166. https://doi.org/10.1023/A:1006592502746

McCollom, T. M., & Seewald, J. S. (2001). A reassessment of the potential for reduction of dissolved CO_2 to hydrocarbons during serpentinization of olivine. *Geochimica et Cosmochimica Acta*, *65*(21), 3769–3778. https://doi.org/10.1016/S0016-7037(01)00655-X

McCollom, T. M., & Seewald, J. S. (2003). Experimental constraints on the hydrothermal reactivity of organic acids and acid anions: I. Formic acid and formate. *Geochimica et Cosmochimica Acta*, *67*(19), 3625–3644. https://doi.org/10.1016/S0016-7037(03)00136-4

McCollom, T. M., & Seewald, J. S. (2006). Carbon isotope composition of organic compounds produced by abiotic synthesis under hydrothermal conditions. *Earth and Planetary Science Letters*, *243*(1), 74–84. https://doi.org/10.1016/j.epsl.2006.01.027

McCollom, T. M., & Seewald, J. S. (2007). Abiotic synthesis of organic compounds in deep-sea hydrothermal environments. *Chemical Reviews*, *107*(2), 382–401.

McCollom, T. M., & Shock, E. L. (1997). Geochemical constraints on chemolithoautotrophic metabolism by microorganisms in seafloor hydrothermal systems. *Geochimica et Cosmochimica Acta*, *61*(20), 4375–4391. https://doi.org/10.1016/S0016-7037(97)00241-X

McDermott, J. M., Seewald, J. S., German, C. R., & Sylva, S. P. (2015). Pathways for abiotic organic synthesis at submarine hydrothermal fields. *Proceedings of the National Academy of Sciences*, *112*(25), 7668–7672. https://doi.org/10.1073/pnas.1506295112

McKay, C. P., Anbar, A. D., Porco, C., & Tsou, P. (2014). Follow the plume: The habitability of Enceladus. *Astrobiology*, *14*(4), 352–355. https://doi.org/10.1089/ast.2014.1158

McKinnon, W. B. (2015). Effect of Enceladus's rapid synchronous spin on interpretation of Cassini gravity. *Geophysical Research Letters*, *42*(7), 2137–2143. https://doi.org/10.1002/2015GL063384

Melwani Daswani, M., Vance, S. D., Mayne, M. J., & Glein, C. R. (2021). A metamorphic origin for Europa's ocean. *Geophysical Research Letters*, *48*(18), e2021GL094143. https://doi.org/10.1029/2021GL094143

Ménez, B., Pisapia, C., Andreani, M., Jamme, F., Vanbellingen, Q. P., Brunelle, A., Richard, L., Dumas, P., & Refregiers, M. (2018). Abiotic synthesis of amino acids in the recesses of the oceanic lithosphere. *Nature*, *564*, 59–63.

Miller, M. E. C., Burke, S. E., & Continetti, R. E. (2022). Production and impact characterization of Enceladus ice grain analogues. *ACS Earth and Space Chemistry*, *6*(7), 1813–1822. https://doi.org/10.1021/acsearthspacechem.2c00087

Mizan, T. I., Savage, P. E., & Ziff, R. M. (1994). Molecular dynamics of supercritical water using a flexible SPC model. *The Journal of Physical Chemistry*, *98*(49), 13067–13076. https://doi.org/10.1021/j100100a042

Mohan, M., Timung, R., Deshavath, N. N., Banerjee, T., Goud, V. V., & Dasu, V. V. (2015). Optimization and hydrolysis of cellulose under subcritical water treatment for the production of total reducing sugars. *RSC Advances*, *5*(125), 103265–103275. https://doi.org/10.1039/C5RA20319H

Musiolik, G., Teiser, J., Jankowski, T., & Wurm, G. (2016). Ice grain collisions in comparison: CO_2, H_2O, and their mixtures. *The Astrophysical Journal*, *827*(1), 63. https://doi.org/10.3847/0004-637X/827/1/63

Musivand, S., Bracciale, M. P., Damizia, M., De Filippis, P., & de Caprariis, B. (2023). Viable recycling of polystyrene via hydrothermal liquefaction and pyrolysis. *Energies*, *16*(13), Article 13. https://doi.org/10.3390/en16134917

Mwanza, B. G. (2021). Introduction to recycling. J. Parameswaranpillai, S. Mavinkere Rangappa, A. Gulihonnehalli Rajkumar, & S. Siengchin (Eds.), *Recent Developments in Plastic Recycling* (pp. 1–13). Springer. https://doi.org/10.1007/978-981-16-3627-1_1

Nadoll, P., Angerer, T., Mauk, J. L., French, D., & Walshe, J. (2014). The chemistry of hydrothermal magnetite: A review. *Ore Geology Reviews*, *61*, 1–32. https://doi.org/10.1016/j.oregeorev.2013.12.013

Nakajima, M., & Ingersoll, A. P. (2016). Controlled boiling on Enceladus. 1. Model of the vapor-driven jets. *Icarus*, *272*, 309–318. https://doi.org/10.1016/j.icarus.2016.02.027

Napper, I. E., Davies, B. F. R., Clifford, H., Elvin, S., Koldewey, H. J., Mayewski, P. A., Miner, K. R., Potocki, M., Elmore, A. C., Gajurel, A. P., & Thompson, R. C. (2020). Reaching new heights in plastic pollution—Preliminary findings of microplastics on Mount Everest. *One Earth*, *3*(5), 621–630. https://doi.org/10.1016/j.oneear.2020.10.020

Naraoka, H., Takano, Y., Dworkin, J. P., Oba, Y., Hamase, K., Furusho, A., Ogawa, N. O., Hashiguchi, M., Fukushima, K., Aoki, D., Schmitt-Kopplin, P., Aponte, J. C., Parker, E. T., Glavin, D. P., McLain, H. L., Elsila, J. E., Graham, H. V., Eiler, J. M., Orthous-Daunay, F.-R., … Tsuda, Y. (2023). Soluble organic molecules in samples of the carbonaceous asteroid (162173) Ryugu. *Science*, *379*(6634), eabn9033. https://doi.org/10.1126/science.abn9033

Neveu, M., Aspin, A., Naseem, M., & Yang, Z. (2024a). Effect of the liquid-vacuum transition on the relative abundances of amino and fatty acids sought as biosignatures on icy ocean worlds. *Earth and Planetary Science Letters*, *630*, 118622. https://doi.org/10.1016/j.epsl.2024.118622

Neveu, M., Desch, S. J., Shock, E. L., & Glein, C. R. (2015). Prerequisites for explosive cryovolcanism on dwarf planet-class Kuiper belt objects. *Icarus*, *246*, 48–64. https://doi.org/10.1016/j.icarus.2014.03.043

Neveu, M., Hays, L. E., Voytek, M. A., New, M. H., & Schulte, M. D. (2018). The ladder of life detection. *Astrobiology*, *18*(11), 1375–1402. https://doi.org/10.1089/ast.2017.1773

Neveu, M., Quinn, R., Barge, L. M., Craft, K. L., German, C. R., Getty, S., Glein, C., Parra, M., Burton, A. S., Cary, F., Corpolongo, A., Fifer, L., Gangidine, A., Gentry, D., Georgiou, C. D., Haddadin, Z., Herbold, C., Inaba, A., Jordan, S. F., … Yang, Z. (2024b). Future of the search for life: Workshop report. *Astrobiology*, *24*(1), 114–129. https://doi.org/10.1089/ast.2022.0158

Nietiadi, M. L., Rosandi, Y., & Urbassek, H. M. (2020). Collisions between ice-covered silica grains: An atomistic study. *Icarus*, *352*, 113996. https://doi.org/10.1016/j.icarus.2020.113996

Nishikawa, K., & Ooi, T. (1982). Correlation of the amino acid composition of a protein to its structural and biological characters. *The Journal of Biochemistry*, *91*(5), 1821–1824. https://doi.org/10.1093/oxfordjournals.jbchem.a133877

NIST. (2023). *Acetic acid* [SRD 69]. National Institute of Standards and Technology. https://webbook.nist.gov/cgi/cbook.cgi?ID=64-19-7

O'Connor, C. T., & Kojima, M. (1990). Alkene oligomerization. *Catalysis Today*, *6*(3), 329–349. https://doi.org/10.1016/0920-5861(90)85008-C

Okada, K., Imashuku, Y., & Yao, M. (1997). Microwave spectroscopy of supercritical water. *The Journal of Chemical Physics*, *107*(22), 9302–9311. https://doi.org/10.1063/1.475226

Parker, E. T., McLain, H. L., Glavin, D. P., Dworkin, J. P., Elsila, J. E., Aponte, J. C., Naraoka, H., Takano, Y., Tachibana, S., Yabuta, H., Yurimoto, H., Sakamoto, K., Yada, T., Nishimura, M., Nakato, A., Miyazaki, A., Yogata, K., Abe, M., Okada, T., … Nakamura, T. (2023). Extraterrestrial amino acids and amines identified in asteroid Ryugu samples returned by the Hayabusa2 mission. *Geochimica et Cosmochimica Acta*, *347*, 42–57. https://doi.org/10.1016/j.gca.2023.02.017

Patthoff, D. A., & Kattenhorn, S. A. (2011). A fracture history on Enceladus provides evidence for a global ocean. *Geophysical Research Letters*, *38*(18). https://doi.org/10.1029/2011GL048387

Pedreira-Segade, U., Hao, J., Montagnac, G., Cardon, H., & Daniel, I. (2019). Spontaneous polymerization of glycine under hydrothermal conditions. *ACS Earth and Space Chemistry*, *3*(8), 1669–1677. https://doi.org/10.1021/acsearthspacechem.9b00043

Peter, J. S., Nordheim, T. A., & Hand, K. P. (2023, December 15). *Detection of HCN and diverse redox chemistry in the plume of Enceladus*. AGU23. https://agu.confex.com/agu/fm23/meetingapp.cgi/Paper/1352721

Porco, C. C., Helfenstein, P., Thomas, P. C., Ingersoll, A. P., Wisdom, J., West, R., Neukum, G., Denk, T., Wagner, R., Roatsch, T., Kieffer, S., Turtle, E., McEwen, A., Johnson, T. V., Rathbun, J., Veverka, J., Wilson, D., Perry, J., Spitale, J., … Squyres, S. (2006). Cassini observes the active south pole of Enceladus. *Science*, *311*(5766), 1393–1401. https://doi.org/10.1126/science.1123013

Porco, C., DiNino, D., & Nimmo, F. (2014). How the geysers, tidal stresses, and thermal emission across the south polar terrain of Enceladus are related. *The Astronomical Journal*, *148*(3), 45. https://doi.org/10.1088/0004-6256/148/3/45

Postberg, F., Clark, R. N., Hansen, C. J., Coates, A. J., Ore, C. M. D., Scipioni, F., Hedman, M. M., Waite, J. H., & Dotson, R. (2018a). Plume and surface composition of Enceladus. R. N. Clark, J. H. Waite, P. M. Schenk, C. J. A. Howett, & A. J. Verbiscer (Eds.), *Enceladus and the Icy Moons of Saturn* (pp. 129–162). University of Arizona Press; JSTOR. http://www.jstor.org/stable/j.ctv65sw2b.16

Postberg, F., Khawaja, N., Abel, B., Choblet, G., Glein, C. R., Gudipati, M. S., Henderson, B. L., Hsu, H.-W., Kempf, S., Klenner, F., Moragas-Klostermeyer, G., Magee, B., Nölle, L., Perry, M., Reviol, R., Schmidt, J., Srama, R., Stolz, F., Tobie, G., … Waite, J. H. (2018b). Macromolecular organic compounds from the depths of Enceladus. *Nature*, *558*(7711), 564–568. https://doi.org/10.1038/s41586-018-0246-4

Postberg, F., Schmidt, J., Hillier, J., Kempf, S., & Srama, R. (2011). A salt-water reservoir as the source of a compositionally stratified plume on Enceladus. *Nature*, *474*(7353), 620–622. https://doi.org/10.1038/nature10175

Postberg, F., Sekine, Y., Klenner, F., Glein, C. R., Zou, Z., Abel, B., Furuya, K., Hillier, J. K., Khawaja, N., Kempf, S., Noelle, L., Saito, T., Schmidt, J., Shibuya, T., Srama, R., & Tan, S. (2023). Detection of phosphates originating from Enceladus's ocean. *Nature*, *618*(7965), Article 7965. https://doi.org/10.1038/s41586-023-05987-9

Proskurowski, G., Lilley, M. D., Seewald, J. S., Früh-Green, G. L., Olson, E. J., Lupton, J. E., Sylva, S. P., & Kelley, D. S. (2008). Abiogenic hydrocarbon production at Lost City Hydrothermal Field. *Science*, *319*(5863), 604–607. https://doi.org/10.1126/science.1151194

Pruppacher, H. R., & Klett, J. D. (2010). Homogeneous nucleation. H. R. Pruppacher & J. D. Klett (Eds.), *Microphysics of Clouds and Precipitation* (pp. 191–215). Springer Netherlands. https://doi.org/10.1007/978-0-306-48100-0_7

Qiu, Z., Fan, W., Han, X., Chen, X., & Yin, X. (2023). Distribution, speciation and mobility of metals in sediments of the Tianxiu hydrothermal field, Carlsberg Ridge, Northwest Indian Ocean. *Journal of Marine Systems*, *237*, 103826. https://doi.org/10.1016/j.jmarsys.2022.103826

Quick, L. C., Glaze, L. S., & Baloga, S. M. (2017). Cryovolcanic emplacement of domes on Europa. *Icarus*, *284*, 477–488. https://doi.org/10.1016/j.icarus.2016.06.029

Ragusa, A., Svelato, A., Santacroce, C., Catalano, P., Notarstefano, V., Carnevali, O., Papa, F., Rongioletti, M. C. A., Baiocco, F., Draghi, S., D'Amore, E., Rinaldo, D., Matta, M., & Giorgini, E. (2021). Plasticenta: First evidence of microplastics in human placenta. *Environment International*, *146*, 106274. https://doi.org/10.1016/j.envint.2020.106274

Reeves, E. P., Seewald, J. S., & Sylva, S. P. (2012). Hydrogen isotope exchange between n-alkanes and water under hydrothermal conditions. *Geochimica et Cosmochimica Acta*, *77*, 582–599. https://doi.org/10.1016/j.gca.2011.10.008

Remko, M., Fitz, D., Broer, R., & Rode, B. (2011). Effect of metal Ions (Ni^{2+}, Cu^{2+} and Zn^{2+}) and water coordination on the structure of L-phenylalanine, L-tyrosine, L-tryptophan and their zwitterionic forms. *Journal of Molecular Modeling*, *17*(12), 3117–3128.

Robinson, K. J., Bockisch, C., Gould, I. R., Liao, Y., Yang, Z., Glein, C. R., Shaver, G. D., Hartnett, H. E., Williams, L. B., & Shock, E. L. (2021a). Quantifying the extent of amide and peptide bond synthesis across conditions relevant to geologic and planetary environments. *Geochimica et Cosmochimica Acta*, *300*, 318–332. https://doi.org/10.1016/j.gca.2021.01.038

Robinson, K. J., Gould, I. R., Fecteau, K. M., Hartnett, H. E., Williams, L. B., & Shock, E. L. (2019). Deamination reaction mechanisms of protonated amines under hydrothermal conditions. *Geochimica et Cosmochimica Acta*, *244*, 113–128. https://doi.org/10.1016/j.gca.2018.09.020

Robinson, K. J., Gould, I. R., Hartnett, H. E., Williams, L. B., & Shock, E. L. (2021b). Hydrothermal experiments with protonated benzylamines provide predictions of temperature-dependent deamination rates for geochemical modeling. *ACS Earth and Space Chemistry*, *5*(8), 1997–2012. https://doi.org/10.1021/acsearthspacechem.1c00104

Rochman, C. M., Browne, M. A., Underwood, A. J., van Franeker, J. A., Thompson, R. C., & Amaral-Zettler, L. A. (2016). The ecological impacts of marine debris: Unraveling the demonstrated evidence from what is perceived. *Ecology*, *97*(2), 302–312. https://doi.org/10.1890/14-2070.1

Rodziewicz, P., & Doltsinis, N. L. (2007). Ab initio molecular dynamics free-energy study of microhydration effects on the neutral–zwitterion equilibrium of phenylalanine. *ChemPhysChem*, *8*(13), 1959–1968. https://doi.org/10.1002/cphc.200700252

Roth, L., Saur, J., Retherford, K. D., Strobel, D. F., Feldman, P. D., McGrath, M. A., & Nimmo, F. (2014). Transient water vapor at Europa's south pole. *Science*, *343*(6167), 171–174. https://doi.org/10.1126/science.1247051

Ruesch, O., Platz, T., Schenk, P., McFadden, L. A., Castillo-Rogez, J. C., Quick, L. C., Byrne, S., Preusker, F., O'Brien, D. P., Schmedemann, N., Williams, D. A., Li, J.-Y., Bland, M. T., Hiesinger, H., Kneissl, T., Neesemann, A., Schaefer, M., Pasckert, J. H., Schmidt, B. E., … Russell, C. T. (2016). Cryovolcanism on Ceres. *Science*, *353*(6303), aaf4286. https://doi.org/10.1126/science.aaf4286

Ruesch, O., Quick, L. C., Landis, M. E., Sori, M. M., Čadek, O., Brož, P., Otto, K. A., Bland, M. T., Byrne, S., Castillo-Rogez, J. C., Hiesinger, H., Jaumann, R., Krohn, K., McFadden, L. A., Nathues, A., Neesemann, A., Preusker, F., Roatsch, T., Schenk, P. M., … Russell, C. T. (2019). Bright carbonate surfaces on Ceres as remnants of salt-rich water fountains. *Icarus*, *320*, 39–48. https://doi.org/10.1016/j.icarus.2018.01.022

Russell, M. J., & Hall, A. J. (1997). The emergence of life from iron monosulphide bubbles at a submarine hydrothermal redox and pH front. *Journal of the Geological Society*, *154*(3), 377–402. https://doi.org/10.1144/gsjgs.154.3.0377

Sander, S. G., & Koschinsky, A. (2011). Metal flux from hydrothermal vents increased by organic complexation. *Nature Geoscience*, *4*, 145. https://doi.org/10.1038/ngeo1088

Sato, N., Quitain, A. T., Kang, K., Daimon, H., & Fujie, K. (2004). Reaction kinetics of amino acid decomposition in high-temperature and high-pressure water. *Industrial & Engineering Chemistry Research*, *43*(13), 3217–3222. https://doi.org/10.1021/ie020733n

Schäfer, C., Ellstrom, C. J., & Török, B. (2018). Heterogeneous catalytic aqueous phase oxidative cleavage of styrenes to benzaldehydes: An environmentally benign alternative to ozonolysis. *Topics in Catalysis*, *61*(7), 643–651. https://doi.org/10.1007/s11244-018-0961-y

Schmidt, J., Brilliantov, N., Spahn, F., & Kempf, S. (2008). Slow dust in Enceladus' plume from condensation and wall collisions in tiger stripe fractures. *Nature*, *451*(7179), 685–688. https://doi.org/10.1038/nature06491

Schmidt, K., Koschinsky, A., Garbe-Schönberg, D., de Carvalho, L. M., & Seifert, R. (2007). Geochemistry of hydrothermal fluids from the ultramafic-hosted Logatchev hydrothermal field, 15°N on the Mid-Atlantic Ridge: Temporal and spatial investigation. *Chemical Geology*, *242*(1), 1–21. https://doi.org/10.1016/j.chemgeo.2007.01.023

Scully, J. E. C., Schenk, P. M., Castillo-Rogez, J. C., Buczkowski, D. L., Williams, D. A., Pasckert, J. H., Duarte, K. D., Romero, V. N., Quick, L. C., Sori, M. M., Landis, M. E., Raymond, C. A., Neesemann, A., Schmidt, B. E., Sizemore, H. G., & Russell, C. T. (2020). The varied sources of faculae-forming brines in Ceres' Occator crater emplaced via hydrothermal brine effusion. *Nature Communications*, *11*(1), 3680. https://doi.org/10.1038/s41467-020-15973-8

Seewald, J. S. (1994). Evidence for metastable equilibrium between hydrocarbons under hydrothermal conditions. *Nature*, *370*(6487), 285–287.

Seewald, J. S. (2001). Aqueous geochemistry of low molecular weight hydrocarbons at elevated temperatures and pressures: Constraints from mineral buffered laboratory experiments. *Geochimica et Cosmochimica Acta*, *65*(10), 1641–1664. https://doi.org/10.1016/S0016-7037(01)00544-0

Seewald, J. S. (2003). Organic-inorganic interactions in petroleum-producing sedimentary basins. *Natur*, *426*(6964), 327–333.

Seshasayee, M., & Savage, P. (2020). Oil from plastic via hydrothermal liquefaction: Production and characterization. *Applied Energy*, *278*.

Seshasayee, M., & Savage, P. (2021a). Synergistic interactions during hydrothermal liquefaction of plastics and biomolecules. *Chemical Engineering Journal, 417*.

Seshasayee, M., Stofanak, R., & Savage, P. (2021b). Component additivity model for plastics-biomass mixtures during hydrothermal liquefaction in sub-, near-, and supercritical water. *Science, 24*(12).

Seyfried, W. E., Pester, N. J., Ding, K., & Rough, M. (2011). Vent fluid chemistry of the Rainbow hydrothermal system (36°N, MAR): Phase equilibria and in situ pH controls on subseafloor alteration processes. *Geochimica et Cosmochimica Acta*, *75*(6), 1574–1593. https://doi.org/10.1016/j.gca.2011.01.001

Shah, H. H., Amin, M., Iqbal, A., Nadeem, I., Kalin, M., Soomar, A. M., & Galal, A. M. (2023). A review on gasification and pyrolysis of waste plastics. *Frontiers in Chemistry*, *10*, 960894. https://doi.org/10.3389/fchem.2022.960894

Shan, G., Li, W., Bao, S., Li, Y., & Tan, W. (2023). Co-hydrothermal carbonization of agricultural waste and sewage sludge for product quality improvement: Fuel properties of hydrochar and fertilizer quality of aqueous phase. *Journal of Environmental Management, 326*.

Shapiro, R., & Schulze-Makuch, D. (2009). The search for alien life in our solar system: Strategies and priorities. *Astrobiology*, *9*(4), 335–343. https://doi.org/10.1089/ast.2008.0281

Shen, M., Hu, T., Huang, W., Song, B., Qin, M., Yi, H., Zeng, G., & Zhang, Y. (2021). Can incineration completely eliminate plastic wastes? An investigation of microplastics and heavy metals in the bottom ash and fly ash from an incineration plant. *Science of The Total Environment, 779*, 146528. https://doi.org/10.1016/j.scitotenv.2021.146528

Shen, M., Song, B., Zeng, G., Zhang, Y., Huang, W., Wen, X., & Tang, W. (2020). Are biodegradable plastics a promising solution to solve the global plastic pollution? *Environmental Pollution, 263*.

Shi, W., Liu, C., Ding, D., Lei, Z., Yang, Y., Feng, C., & Zhang, Z. (2013a). Immobilization of heavy metals in sewage sludge by using subcritical water technology. *Bioresource Technology, 137*.

Shi, W., Liu, C., Shu, Y., Feng, C., Lei, Z., & Zhang, Z. (2013b). Synergistic effect of rice husk addition on hydrothermal treatment of sewage sludge: Fate and environmental risk of heavy metals. *Bioresource Technology, 149*.

Shipp, J., Gould, I. R., Herckes, P., Shock, E. L., Williams, L. B., & Hartnett, H. E. (2013a). Organic functional group transformations in water at elevated temperature and pressure: Reversibility, reactivity, and mechanisms. *Geochimica et Cosmochimica Acta*, *104*(104), 194–209. https://doi.org/10.1016/j.gca.2012.11.014

Shipp, J., Gould, I., Shock, E., Williams, L., & Hartnett, H. (2013b). Sphalerite is a geochemical catalyst for carbon-hydrogen bond activation. *Proceedings of the National Academy of Sciences, 111*.

Shock, E., Bockisch, C., Estrada, C., Fecteau, K., Gould, I., Hartnett, H., Johnson, K., Robinson, K., Shipp, J., & Williams, L. (2020). Earth as organic chemist. B. Orcutt, I. Daniel, & R. Dasgupta (Eds.), *Deep Carbon: Past to Present*. Cambridge University Press.

Shock, E., & Canovas, P. (2010). The potential for abiotic organic synthesis and biosynthesis at seafloor hydrothermal systems. *Geofluids, 10,* 161–192.

Shock, E., Canovas, P., Yang, Z., Boyer, G., Johnson, K., Robsinson, K., Fecteau, K., Windman, T., & Cox, A. (2013). Thermodynamics of organic transformations in hydrothermal fluids. *Reviews in mineralogy and geochemistry, 76*(1).

Shock, E. L. (1992). Stability of peptides in high-temperature aqueous solutions. *Geochimica et Cosmochimica Acta*, *56*(9), 3481–3491. https://doi.org/10.1016/0016-7037(92)90392-V

Shock, E. L. (1993). Hydrothermal dehydration of aqueous organic compounds. *Geochimica et Cosmochimica Acta*, *57*(14), 3341–3349. https://doi.org/10.1016/0016-7037(93)90542-5

Shock, E. L., & Helgeson, H. C. (1988). Calculation of the thermodynamic and transport properties of aqueous species at high pressures and temperatures: Correlation algorithms for ionic species and equation of state predictions to 5 kb and 1000°C. *Geochimica et Cosmochimica Acta*, *52*(8), 2009–2036. https://doi.org/10.1016/0016-7037(88)90181-0

Shock, E. L., & Schulte, M. D. (1998). Organic synthesis during fluid mixing in hydrothermal systems. *Journal of Geophysical Research: Planets*, *103*(E12), 28513–28527. https://doi.org/10.1029/98JE02142

Snider, M. J., & Wolfenden, R. (2000). The rate of spontaneous decarboxylation of amino acids. *Journal of the American Chemical Society*, *122*(46), 11507–11508. https://doi.org/10.1021/ja002851c

Sonawane, G. H., Patil, S. P., & Sonawane, S. H. (2018). Chapter 1—Nanocomposites and its applications. S. Mohan Bhagyaraj, O. S. Oluwafemi, N. Kalarikkal, & S. Thomas (Eds.), *Applications of Nanomaterials* (pp. 1–22). Woodhead Publishing. https://doi.org/10.1016/B978-0-08-101971-9.00001-6

Spencer, J. R., Nimmo, F., Ingersoll, A. P., Hurford, T. A., Kite, E. S., Rhoden, A. R., Schmidt, J., Howett, C. J. A., & Dotson, R. (2018). Plume origins and plumbing: P. M. Schenk, R. N. Clark, C. J. A. Howett, A. J. Verbiscer, & J. H. Waite (Eds.), *Enceladus and the Icy Moons of Saturn* (pp. 163–174). University of Arizona Press; JSTOR. http://www.jstor.org/stable/j.ctv65sw2b.18

Spiess, F. N., Macdonald, K. C., Atwater, T., Ballard, R., Carranza, A., Cordoba, D., Cox, C., Garcia, V. M. D., Francheteau, J., Guerrero, J., Hawkins, J., Haymon, R., Hessler, R., Juteau, T., Kastner, M., Larson, R., Luyendyk, B., Macdougall, J. D., Miller, S., … Rangin, C. (1980). East Pacific Rise: Hot springs and geophysical experiments. *Science*, *207*(4438), 1421–1433. https://doi.org/10.1126/science.207.4438.1421

Steddum, R. E. (1971). *Characteristics of Water Sprays Under Vacuum Conditions* [Ph.D., Louisiana State University and Agricultural & Mechanical College]. https://www.proquest.com/docview/302626999/citation/A5D68F1F5634A0APQ/1

Steel, E. L., Davila, A., & McKay, C. P. (2017). Abiotic and biotic formation of amino acids in the Enceladus ocean. *Astrobiology*, *17*(9), 862–875. https://doi.org/10.1089/ast.2017.1673

Sui, Q., Zhao, W., Cao, X., Lu, S., Qiu, Z., Gu, X., & Yu, G. (2017). Pharmaceuticals and personal care products in the leachates from a typical landfill reservoir of municipal solid waste in Shanghai, China: Occurrence and removal by a full-scale membrane bioreactor. *Journal of Hazardous Materials, 323*, 99–108. https://doi.org/10.1016/j.jhazmat.2016.03.047

Sun, A., & Wang, W.-X. (2023). Human exposure to microplastics and its associated health risks. *Environment & Health*, *1*(3), 139–149. https://doi.org/10.1021/envhealth.3c00053

Tagliabue, A., Bowie, A. R., Boyd, P. W., Buck, K. N., Johnson, K. S., & Saito, M. A. (2017). The integral role of iron in ocean biogeochemistry. *Nature*, *543*(7643), 51–59. https://doi.org/10.1038/nature21058

Tekman, M. B., Wekerle, C., Lorenz, C., Primpke, S., Hasemann, C., Gerdts, G., & Bergmann, M. (2020). Tying up loose ends of microplastic pollution in the arctic: Distribution from the sea surface through the water column to deep-sea sediments at the HAUSGARTEN Observatory. *Environmental Science & Technology*, *54*(7), 4079–4090. https://doi.org/10.1021/acs.est.9b06981

Tester, J. W., Webley, P. A., & Holgate, H. R. (1993). Revised global kinetic measurements of methanol oxidation in supercritical water. *Industrial & Engineering Chemistry Research*, *32*(1), 236–239. https://doi.org/10.1021/ie00013a032

Thomas, E. C., Vu, T. H., Hodyss, R., Johnson, P. V., & Choukroun, M. (2019). Kinetic effect on the freezing of ammonium-sodium-carbonate-chloride brines and implications for the origin of Ceres' bright spots. *Icarus, 320*, 150–158. https://doi.org/10.1016/j.icarus.2017.12.038

Thomas, P. C., Tajeddine, R., Tiscareno, M. S., Burns, J. A., Joseph, J., Loredo, T. J., Helfenstein, P., & Porco, C. (2016). Enceladus's measured physical libration requires a global subsurface ocean. *Icarus, 264*, 37–47. https://doi.org/10.1016/j.icarus.2015.08.037

Thunman, H., Vilches, T., Seemann, M., Maric, J., Vela, I., Pissot, S., & Nguyen, H. (2019). Circular use of plastics-transformation of existing petrochemical clusters into thermochemical recycling plants with 100% plastics recovery. *Sustainable Materials and Technology, 22*.

Tosi, F., Mura, A., Cofano, A., Zambon, F., Glein, C. R., Ciarniello, M., Lunine, J. I., Piccioni, G., Plainaki, C., Sordini, R., Adriani, A., Bolton, S. J., Hansen, C. J., Nordheim, T. A., Moirano, A., Agostini, L., Altieri, F., Brooks, S. M., Cicchetti, A., … Turrini, D. (2024). Salts and organics on Ganymede's surface observed by the JIRAM spectrometer onboard Juno. *Nature Astronomy*, *8*(1), 82–93. https://doi.org/10.1038/s41550-023-02107-5

Trumbo, S. K., Becker, T. M., Brown, M. E., Denman, W. T. P., Molyneux, P., Hendrix, A., Retherford, K. D., Roth, L., & Alday, J. (2022). A new UV spectral feature on Europa: Confirmation of NaCl in leading-hemisphere chaos terrain. *The Planetary Science Journal*, *3*(2), 27. https://doi.org/10.3847/PSJ/ac4580

Truong, N., Monroe, A. A., Glein, C. R., Anbar, A. D., & Lunine, J. I. (2019). Decomposition of amino acids in water with application to in-situ measurements of Enceladus, Europa and other hydrothermally active icy ocean worlds. *Icarus*, *329*, 140–147. https://doi.org/10.1016/j.icarus.2019.04.009

Vallentyne, J. R. (1964). Biogeochemistry of organic matter—II Thermal reaction kinetics and transformation products of amino compounds. *Geochimica et Cosmochimica Acta*, *28*(2), 157–188. https://doi.org/10.1016/0016-7037(64)90147-4

Vance, S. D., Craft, K. L., Shock, E., Schmidt, B. E., Lunine, J., Hand, K. P., McKinnon, W. B., Spiers, E. M., Chivers, C., Lawrence, J. D., Wolfenbarger, N., Leonard, E. J., Robinson, K. J., Styczinski, M. J., Persaud, D. M., Steinbrügge, G., Zolotov, M. Y., Quick, L. C., Scully, J. E. C., … Elder, C. M. (2023). Investigating Europa's habitability with the Europa Clipper. *Space Science Reviews*, *219*(8), 81. https://doi.org/10.1007/s11214-023-01025-2

Venturi, S., Tassi, F., Gould, I. R., Shock, E. L., Hartnett, H. E., Lorance, E. D., Bockisch, C., Fecteau, K. M., Capecchiacci, F., & Vaselli, O. (2017). Mineral-assisted production of benzene under hydrothermal conditions: Insights from experimental studies on C6 cyclic hydrocarbons. *Journal of Volcanology and Geothermal Research, 346*, 21–27.

Villanueva, G. L., Hammel, H. B., Milam, S. N., Faggi, S., Kofman, V., Roth, L., Hand, K. P., Paganini, L., Stansberry, J., Spencer, J., Protopapa, S., Strazzulla, G., Cruz-Mermy, G., Glein, C. R., Cartwright, R., & Liuzzi, G. (2023a). Endogenous CO_2 ice mixture on the surface of Europa and no detection of plume activity. *Science*, *381*(6664), 1305–1308. https://doi.org/10.1126/science.adg4270

Villanueva, G. L., Hammel, H. B., Milam, S. N., Kofman, V., Faggi, S., Glein, C. R., Cartwright, R., Roth, L., Hand, K. P., Paganini, L., Spencer, J., Stansberry, J., Holler, B., Rowe-Gurney, N., Protopapa, S., Strazzulla, G., Liuzzi, G., Cruz-Mermy, G., El Moutamid, M., … Denny, K. (2023b). JWST molecular mapping and characterization of Enceladus' water plume feeding its torus. *Nature Astronomy, 7*(9), 1056–1062. https://doi.org/10.1038/s41550-023-02009-6

Vu, T. H., Choukroun, M., Hodyss, R., & Johnson, P. V. (2020). Probing Europa's subsurface ocean composition from surface salt minerals using in-situ techniques. *Icarus*, *349*, 113746. https://doi.org/10.1016/j.icarus.2020.113746

Vu, T. H., Hodyss, R., Johnson, P. V., & Cable, M. L. (2023). Spatial distribution of glycine and aspartic acid in rapidly frozen brines relevant to Enceladus. *The Planetary Science Journal*, *4*(8), 156. https://doi.org/10.3847/PSJ/aced90

Waite, J. H., Glein, C. R., Perryman, R. S., Teolis, B. D., Magee, B. A., Miller, G., Grimes, J., Perry, M. E., Miller, K. E., Bouquet, A., Lunine, J. I., Brockwell, T., & Bolton, S. J. (2017). Cassini finds molecular hydrogen in the Enceladus plume: Evidence for hydrothermal processes. *Science*, *356*(6334), 155–159. https://doi.org/10.1126/science.aai8703

Waluyo, I., Huang, C., Nordlund, D., Weiss, T. M., Pettersson, L. G. M., & Nilsson, A. (2011). Increased fraction of low-density structures in aqueous solutions of fluoride. *The Journal of Chemical Physics*, *134*(22), 224507. https://doi.org/10.1063/1.3597606

Wang, R., Lin, Z., Meng, S., Liu, S., Zhao, Z., Wang, C., & Yin, Q. (2022). Effect of lignocellulosic components on the hydrothermal carbonization reaction pathway and product properties of protein. *Energy*, *259*.

Wimmer, J. L. E., Xavier, J. C., Vieira, A. d N., Pereira, D. P. H., Leidner, J., Sousa, F. L., Kleinermanns, K., Preiner, M., & Martin, W. F. (2021). Energy at origins: Favorable thermodynamics of biosynthetic reactions in the Last Universal Common Ancestor (LUCA). *Frontiers in Microbiology*, *12*. https://doi.org/10.3389/fmicb.2021.793664

Wolery, T. J. (1992). *EQ3/6, a software package for geochemical modeling of aqueous systems: Package overview and installation guide (version 7.0)* [Report]. Lawrence Livermore National Lab.

Xiong, J., Chen, S., Wang, J., Wang, Y., Fang, X., & Huang, H. (2021). Speciation of main nutrients (N/P/K) in hydrochars produced from the hydrothermal carbonization of swine manure under different reaction temperatures. *Materials*, *14*(15).

Yadav, G. D. (2024). The net zero goal and sustainability: Significance of green hydrogen economy in valorization of CO_2, biomass and plastic waste into chemicals and materials. M. Goel & G. Sen (Eds.), *Climate Action and Hydrogen Economy: Technologies Shaping the Energy Transition* (pp. 61–90). Springer Nature. https://doi.org/10.1007/978-981-99-6237-2_4

Yang, Z., & Aspin, A. (2023). *Hydrothermal Chemistry*. American Chemical Society. https://doi.org/10.1021/acsinfocus.7e7023

Yang, Z., & Fu, X. (2018). An experimental protocol for studying mineral effects on organic hydrothermal transformations. *JoVE* (Issue 138, p. e58230).

Yang, Z., Gould, I. R., Williams, L. B., Hartnett, H. E., & Shock, E. L. (2012). The central role of ketones in reversible and irreversible hydrothermal organic functional group transformations. *Geochimica et Cosmochimica Acta, 98,* 48–65. http://dx.doi.org/10.1016/j.gca.2012.08.031

Yang, Z., Gould, I. R., Williams, L. B., Hartnett, H. E., & Shock, E. L. (2018). Effects of iron-containing minerals on hydrothermal reactions of ketones. *Geochimica et Cosmochimica Acta*, *223*, 107–126. https://doi.org/10.1016/j.gca.2017.11.020

Yang, Z., Hartnett, H., Shock, E., & Gould, I. (2015). Organic oxidations using geomimicry.*The Journal of Organic Chemistry, 80*(24), 12159–12165.

Yang, Z., Lorance, E. D., Bockisch, C., Williams, L. B., Hartnett, H. E., Shock, E. L., & Gould, I. R. (2014). Hydrothermal photochemistry as a mechanistic tool in organic geochemistry: The chemistry of dibenzyl ketone. *The Journal of Organic Chemistry*, *79*(17), 7861–7871. https://doi.org/10.1021/jo500899x

Yang, Z., Lü, F., Zhang, H., Wang, W., Shao, L., Ye, J., & He, P. (2021). Is incineration the terminator of plastics and microplastics? *Journal of Hazardous Materials*, *401*, 123429. https://doi.org/10.1016/j.jhazmat.2020.123429

Yao, Z., & Ma, X. (2018). Characteristics of co-hydrothermal carbonization on polyvinyl chloride wastes with bamboo. *Bioresource Technology*, *247*.

Zhao, S., Zhu, L., & Li, D. (2016). Microscopic anthropogenic litter in terrestrial birds from Shanghai, China: Not only plastics but also natural fibers. *Science of The Total Environment*, *550*, 1110–1115. https://doi.org/10.1016/j.scitotenv.2016.01.112

Zhao, X., Xia, Y., Zhan, L., Xie, B., Gao, B., & Wang, J. (2018a). Hydrothermal treatment of e-waste plastics for tertiary recycling: Product slate and decomposition mechanisms. *ACS Sustainable Chemistry and Engineering*, *7*(1).

Zhao, X., Zhan, L., Xie, B., & Gao, B. (2018b). Products derived from waste plastics (PC, HIPS, ABS, PP and PA6) via hydrothermal treatment: Characterization and potential applications. *Chemosphere*, *207*, 742–752. https://doi.org/10.1016/j.chemosphere.2018.05.156